UNIVERSIDADE TÉCNICA DE LISBOA

INSTITUTO SUPERIOR TÉCNICO

Data Acquisition and Performance Studies in Cosmic Ray Experiments

Pedro Jorge dos Santos de Assis
(Mestre)

**Dissertação para obtenção do Grau de Doutor
em Engenharia Física Tecnológica**

Orientador: Doutor Mário João Martins Pimenta
Co-Orientador: Doutor Pedro Miguel Félix Brogueira

Júri

Presidente: Reitor da Universidade Técnica de Lisboa
Vogais: Doutor Jorge Venceslau Comprido Dias de Deus
Doutor Mário João Martins Pimenta
Doutor João Carlos Lopes de Carvalho
Doutor Pedro Miguel Félix Brogueira
Doutor Osvaldo Catalano
Doutor Alan Andrew Watson

Janeiro 2009

Resumo

Esta tese insere-se no âmbito do estudo de detectores de Raios Cósmicos e seus sistemas de aquisição de dados.

Os sistemas de aquisição de dados baseados na técnica Single Photon Counting mereceram especial atenção. Os algoritmos de trigger da missão EUSO foram estudados e implementados na simulação geral. O desenvolvimento e teste de grande parte do firmware de GAW é da responsabilidade do LIP. Os trabalhos efectuados neste domínio estão aqui reportados.

O desenvolvimento de firmware neste quadro requereu a instalação do LIP-eCRLab, equipado com equipamento de teste e medida de grande desempenho. Neste laboratório existirá também uma vertente ensino, nomeadamente em electrónica digital avançada. Foram também desenvolvidos sitemas autónomos de aquisição de dados baseados na LIP-PAD e projectada a sua sucedânea - a LPV3.

No âmbito do Observatório Pierre Auger foi estudado o desempenho dos seus telescópios de fluorescência utilizando a simulação desenvolvida no LIP. Neste estudo estimaram-se os parâmetros ópticos do telescópio bem como a sua eficiência. O estudo da eficiência relativa ao longo da câmara abre a perspectiva para estudos aprofundados utilizando dados reais.

Palavras-chave: Raios Cósmicos, Aquisição de Dados, GAW, ULTRA, EUSO, Auger

Resumo

ii

Abstract

This thesis reflects the work developed in Data Acquisition systems for Cosmic Rays detectors and performance studies of such detectors.

Electronics firmware was mainly developed in the context of Single Photon Counting detectors. The EUSO mission triggering system algorithms and implementation in simulation, complying with the electronics constraints of the mission are reported. The EUSO detector concept is being applied in GAW, a gamma-ray experiment. The firmware of great part of GAW electronics is being developed at LIP and already some interface boards were produced and tests performed.

The requirements of such developments led to the creation of the e-CRLab, a digital electronics laboratory equipped with state of the art test and measurement equipment. Teaching activities in digital electronics and FPGAs are also planned for the e-CRLab. A new generation of LIP-PAD, successfully used in ULTRA and TRC, is being designed.

In the Pierre Auger Observatory the fluorescence telescopes performance was studied using a new simulation developed at LIP and integrated in the Auger simulation framework. This study led to the estimation of optical parameters of the telescope and its efficiency. Studies on relative efficiencies throughout the whole focal surface open a window to explore data.

Key-words: Cosmic Rays, Data Acquisition, GAW, ULTRA, EUSO, Auger

Abstract

Acknowledgments

Foi há cerca de trinta anos que o meu Pai e a minha Mãe uniram esforços e me trancaram num quarto escuro. Durante nove meses fui escravo das suas vontades. Mas, parece que naqueles tempos idos as coisas eram feitas assim. Hoje a situação é um pouco diferente mas sei que continuam a fazer tudo por mim! O meu muito obrigado e a expressão do meu carinho por eles ficam aqui expressos. Ao meu Avô que sempre lutou para que nada faltasse, o meu muito obrigado. Não posso deixar de lembrar aqui a minha Avó que infelizmente não me pôde acompanhar nestes últimos anos. Ao meu Mano que me treinou desde cedo nas artes da guerra e foi meu companheiro expresso aqui o meu carinho (apesar de não me deixar brincar com os carrinhos). Resumindo, obrigado à Francelina aos Jorges e à Candida. Quero também expressar o meu carinho pela família alargada, tios, tias, padrinhos (incluindo os do meu irmão), primos, Isaura ...

A todos os que se cruzaram comigo e que me acompanharam em aventuras e desventuras, à Tecas, à Patrícia, ao Jorge, à Susana, ao Luís, ao David, à Catarina, ao Rodrigo, ao Alves, ao Moura, à Sónia, ao Zé e ao Pedro o meu muito obrigado por todo o companheirismo.

The work in this thesis would not be possible without the contribution of several people to whom I would like to express here my gratitude

To Mário Pimenta and Pedro Brogueira for their supervision and beyond!

To my office colleagues, Patrícia and Bernardo, who had the most painfull jobs of all. Thank you for your "office solidarity".

To my colleagues of LIP working in Cosmic Rays, Fernando, Luísa, Pedro, Sofia, Catarina, Eva, Ruben, Bruno, Sara, thank you for all the support and friendship. To Pedro and Andreia thank you for all the help and discussions. Thank you to all who helped me burning some electronics, namely to Miguel Ferreira, José Carlos Silva, Gonçalo Pires and Luís Mendes.

To the group of Palermo with which we have a strong relationship for a long time, to the ULTRA collaboration, the EUSO collaboration, the GAW collaboration and

to the Pierre Auger collaboration for providing such good working environments.

I would also like to thank the support given by the LIP computing centre, with the difficulties managing conflicting interests and dealing with our many requests. I would also like to leave my thanks to the secretariat, Leonor, Lina, Claudia, Sandra and João, who so many times helped me and tolerated the lack of some 'minor' papers.

Writing this thesis proved to be an even harder task. Thanks to all that reviewed this document.

To Fundação para a Ciência e Tecnologia I need to thank the financial support under the PHD grant SFRH/BD/14226/2003. To LIP I wish to thank for the financial support and also for providing the necessary conditions to develop the work presented in this thesis.

Contents

CONTENTS

x

List of Figures

Chapter 1

Introduction

The history of cosmic ray physics is almost one century long. It started in 1912 when a flux of charged particles coming from above was detected using electroscopes. In the 1930s cloud chambers with magnetic fields were used to study cosmic rays. The observation of tracks similar to those of electrons but bending in the opposite direction led to the discovery of the positron - experimental particle physics was born. In its early years experimental particle physics developed through cosmic ray studies, with the discovery of several elementary particles. In the 1950s, with the first particle accelerators, a controlled, high-luminosity, beam of particles became available and the two fields of research took different paths. However, in the last twenty years, perhaps the most important result in particle physics came from a non-accelerator experiment - Super Kamiokande - with the discovery of neutrino oscillations. In fact, in the last decades, the communities of particle physics, cosmic rays and astrophysics have become increasingly aware of their similarities in terms of methods, tools, language and goals, and of the complementary nature of their probes to the frontiers of our knowledge of the Universe. This opened the field known as astroparticle physics, and has led to a new generation of cosmic ray experiments, which nowadays incorporate the complexity of interaction models, simulation tools, large collaborations and detectors typical of accelerator environments.

Historically, the great steps forward in cosmic ray physics were always linked to the evolution of detectors, progressively becoming more sensitive, precise and autonomous. This was the case in the discovery of Extensive Air Showers (EAS), made possible by fast timing coincidence units with a resolution better than five microseconds. The discovery of air showers was in fact crucial in terms of making sense of the observations: particles often came in bunches originating from a single particle hitting the top of the atmosphere, and what reached ground, actually

secondaries, depended on the original energy. We were no longer simply counting particles actually created in the atmosphere, but now had the concept of a primary particle coming from somewhere in the cosmos, and more and more rare as it became more energetic. The ground observations of EAS became the way of indirectly extracting information about these primary particles, in an attempt to understand their properties and origin.

Large aperture EAS detectors on the ground were for decades the only way to detect high energy cosmic rays hitting the top of the atmosphere. These detectors, composed by particle detectors disposed in arrays, became steadily larger and more sophisticated. The increase in the aperture compensated the power law reduction of the cosmic ray energy spectrum, allowing the study of ever higher energy cosmic rays. New techniques exploiting the light component of the showers appeared more recently: fluorescence telescopes, detecting the light produced by the de-excitation of the nitrogen molecules in the air excited by the shower particles, and Cherenkov telescopes, detecting the Cherenkov light produced by energetic shower particles travelling faster than the speed of light in air. In both cases, the detectors are actually UV telescopes, with optical systems consisting typically of large mirrors and segmented cameras.

In 1981 Fly's Eye became the first cosmic ray experiment employing the fluorescence technique. As the faint and isotropic fluorescence light is only intense enough for very energetic showers, and because it allows the observation of a large volume of atmosphere, this technique is particularly well suited for the low flux, high energy, end of the spectrum, where it has the advantage of providing a picture of the longitudinal development of the shower and a relatively more direct measurement of the energy with respect to ground detectors. While new sources of systematic errors arise in this method, the complementarity between the two techniques is in fact one of the keys to precise, well control and reliable results. It is also one of the great strengths of the Pierre Auger Observatory, a giant hybrid observatory combining the two techniques. The southern site of the Auger Observatory has recently been completed. The striking first results have already been made public, firmly establishing the existence of the GZK cutoff and the anisotropy of the highest energy cosmic rays, as well as raising very interesting puzzles concerning their nature and their interactions in the atmosphere.

Imaging Atmospheric Cherenkov Telescopes (IACT), on the other hand, detecting the rather collimated light cone along the shower axis, are well suited for an intermediate energy range, with larger fluxes, and in particular for the detection of the purely electromagnetic showers produced by TeV photons. Cherenkov telescopes

are today living a golden age, with the discovery of a large number of new point sources in only a few years and interesting results concerning the diffuse component. R&D in this domain is of the uttermost importance to allow for a future generation of detectors that is not only bigger but also better. One of the limitations of the present Cherenkov telescopes is the very small field of view, and the GAW - Gamma Air Watch - project addresses this issue by testing an innovative optical and light detection system.

While dealing with different primary particles and energies ranges, extreme energy cosmic ray detectors and Cherenkov telescopes have in common the goal of understanding the origin of very high energy particles in the Universe. Also, as light detectors, they share a number of detection techniques and characteristics. Finally, with the great success of the Auger observatory and the very interesting data expected in the years to come, and with the outstanding gamma results and the preparation of the next generation, both fields are today in a very exciting period.

The boom in astroparticle physics, and in particular the interest in extreme energy cosmic rays and gamma rays, grew in Portugal only in the late 1990s. The birth of this thesis is intimately related to this event. In 2000 LIP became involved in the EUSO space mission, an ESA mission to be installed in the International Space Station with the goal of detecting extreme energy air showers from above, with an extremely large field of view. This was the staring point for establishing a framework for high energy cosmic ray research in Portugal. A few years later, the participation in the EUSO trigger system design, as well as in supporting experiments for EUSO, was the starting point of this thesis. EUSO successfully completed, from both the technical and the scientific point of view, the Phase A study. The mission was nevertheless put on hold due to financial and programmatic issues related to the Columbia Space Shuttle accident. LIP joined the Pierre Auger Observatory in 2006. As a natural follow up of its experience in EUSO, the LIP group concentrated efforts in the fluorescence detectors. In this context detailed studies of the Auger fluorescence telescopes were performed, namely through precise Geant4-based simulation tools developed in Lisbon. LIP also became involved in GAW, an R&D project in which some of the solutions studied for EUSO, namely the Fresnel lens optical system, the highly-segmented focal surface and the use of the single photon counting technique are being studied for the next generation of Cherenkov telescopes, in order to build a highly sensitive, large field of view detector. LIP has considerable responsibilities in the development of firmware for the GAW trigger and data acquisition systems. This path from EUSO to Auger and GAW was, in addition, crossed by smaller R&D projects mainly for education and public outreach, but also support activities for

the main experiments. These activities relate basically to the development of data acquisition systems for cosmic ray detectors and were an important part of this work.

While the path in this thesis is not a straight one, its key subjects remain clear, and are twofold: the development and detection of air showers, in particular of their light component; and the development of detectors, in particular of trigger and data acquisition firmware. The key projects are, chronologically, EUSO, the Auger Observatory and GAW, together with supporting activities both to the main projects and to education and outreach activities developed at LIP. This thesis is organised as follows: a brief introduction to cosmic ray physics, with emphasis on air shower development and including simulation studies of EAS properties, is presented in chapter 2. An overview of the several relevant projects, EUSO, the Pierre Auger Observatory and GAW, is given in chapter 3. Chapters 4 and 5 relate to the LIP cosmic ray electronics laboratory. While chapter 4 describes the installation and the activities of the laboratory, chapter 5 describes in more detail the design of the data acquisition board LIP-PAD, used both in the ULTRA supporting experiment for EUSO and in the TRC educational project and, in general, well suited for small cosmic ray projects. Chapter 6 and chapter 7 concentrate on the work developed specifically for the main projects. The work developed on trigger design for systems using the single photon counting technique, in the context of EUSO and particularly GAW, is reported in chapter 6. The studies on the performance of the Auger fluorescence telescopes are presented in chapter 7. In chapter 8 some conclusions are drawn.

Chapter 2

A Brief Overview of Some Cosmic Ray Measurements
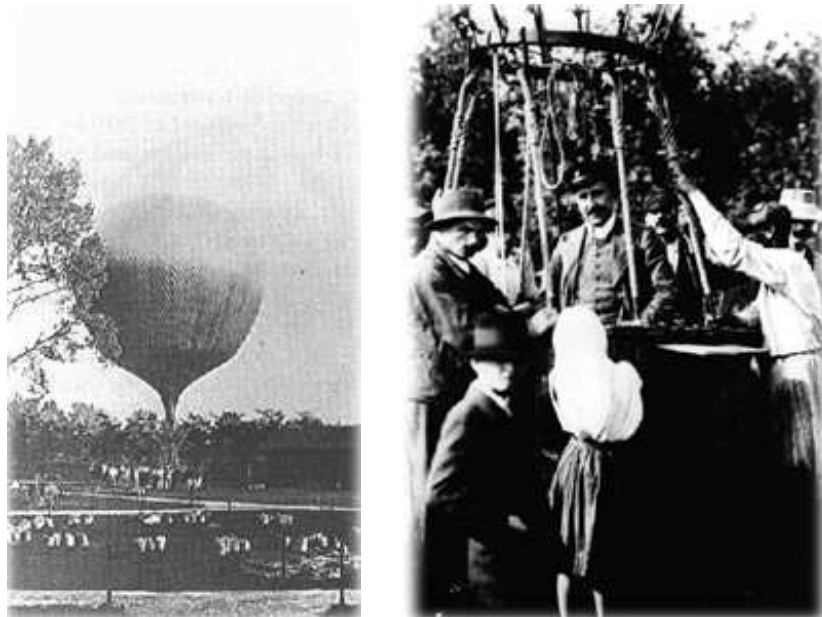
Figure 2.1: Balloon flights of Victor Hess.

"The results of my observations are best explained by the assumption that a radiation of very great penetrating power enters our atmosphere from above"

Victor Hess, Physikalische Zeitschrift, November 1912

The history of cosmic rays started with a very simple instrument - the electro-
scope. By the end of the 19th century it was known that electroscopes discharged
spontaneously due to the ionization of the air, and the rate of discharge of the in-
strument allowed to quantify this effect. The cause of air ionization was believed
to be the natural radioactivity of the Earth. It should therefore decrease with the
distance to ground. Several meaurements were conducted to determine the rate of
discharge with altitude, the most famous being the one performed by Thomas Wulf
in 1910, in which he took an electroscope to the top of the Eiffel tower. The results
showed that the rate of discharge did not decrease as fast as it was expected. In
1912 Victor Hess flew this kind of instrument in hot air balloons to measure the rate
of air ionization with altitude. Hess was able to fly and perform measurements up
to an altitude of 5 km. The results showed that the ionization rate decreased from
ground level to ~ 1 km and then increased with altitude. Such a decrease proved
that in fact a part of the air ionization effect was due to the natural radioactivity of
the Earth. The subsequent increase in the rate, and thus in the air ionization effect,
was attributed by Hess to some kind of radiation arriving to Earth from Space. The
quest to measure such radiation went further with the development of automatic
data acquisition systems for the electroscopes. The devices were then used in un-
manned balloon flights that could reach higher altitudes. Such flights would confirm
Hess results and, eventually, in 1926, Robert Millikan coined the term "Cosmic Rays"
to describe these phenomena.

More sophisticated instruments for the detection of radiation became available
and started to be used in the cosmic ray field. Such instruments, like the cloud
chamber and photographic emulsions, allowed particle tracks to be recorded and, by
the use of magnetic fields, to extract particle parameters like their mass and charge.
In this context particle physics was born, with the discovery of new particles: the
positron in 1932, the muon in 1937, the pion in 1947 followed by the discovery of
"strange" particles.

By the mid 1930s, counters in coincidence were being used in the study of cosmic
rays. At this point an excess in the coincidence rate suggested that particles arrived
in bunches. Later, with the the development of coincidence units with better timing
resolution (around 5 microseconds), Pierre Auger was able to conduct systematic
studies and establish the occurrence of air showers. The discovery of Extensive
Air Showers (EAS) was a breakthrough as it allowed a correlation between the
particles detected at ground and high energy cosmic particles reaching the top of
the atmosphere to be established, and to go higher in energy by building ever larger
sampling detectors. The path to the study of highly energetic cosmic rays was

opened. Still today, sampling detectors are widely used to detect cosmic rays with an energy up to $\sim 10^{20}$ eV with very large sampling arrays. The largest one, the Pierre Auger Observatory, has an area of $\sim 3000\,\mathrm{km}^2$.

An alternative technique to detect EAS - the fluorescence technique - was meanwhile developed. The first studies to detect fluorescence in the atmosphere were performed in the early 1960s in the Los Alamos National Laboratory for military purposes related with nuclear explosions. The idea to use the technique to detect cosmic rays was first proposed by the Cornell Cosmic Ray Observatory in the mid 1960s but was unsuccessful as it was not able to detect light from EAS. The first successful observation of fluorescence light from EAS would come in 1976 with the installation of prototype telescopes in Volcano Ranch by physicist from the Utah University. In 1981 Fly's Eye becomes the first cosmic ray experiment employing the fluorescence technique, which is a well-established technique nowadays. The Pierre Auger Observatory uses this technique together with the sampling technique. The hybrid detection capabilities are one of the strengths of the Observatory, allowing the cross-calibration of the two methods and reducing the systematic errors.

High energy γ-rays have energies in the GeV - TeV range and originate pure electromagnetic showers. Such showers develop high in the atmosphere, making the detection of the front of particles at ground impossible. Also, the fluorescence light emitted by such low energy showers falls below the sensitivity of fluorescence detectors. However, the shower development produces Cherenkov light that accumulates and propagates along the shower direction, producing a signal detectable at ground. In the late 1960s the programme to study the Cherenkov light emitted by EAS started with the Whipple observatory. The idea was to record this light by mean of telescopes. The background from charged cosmic rays was however enormous. The method became more efficient with the introduction of imaging techniques (Hillas, 1985), in which segmented focal surfaces and shower shape variables allowed to distinguish showers initiated by energetic gamma rays. In recent years, larger telescopes and telescope arrays were built, allowing the discovery of an impressive number of γ-ray sources in the sky. Most of the recent results have been provided by HESS, installed in Namibia, and the MAGIC telescope, in the Canary islands.

2.1 Cosmic rays flux

The energy spectrum of cosmic rays covers a very wide range both in energy and flux. In figure 2.2 the differential flux multiplied by E^2 as a function of the energy
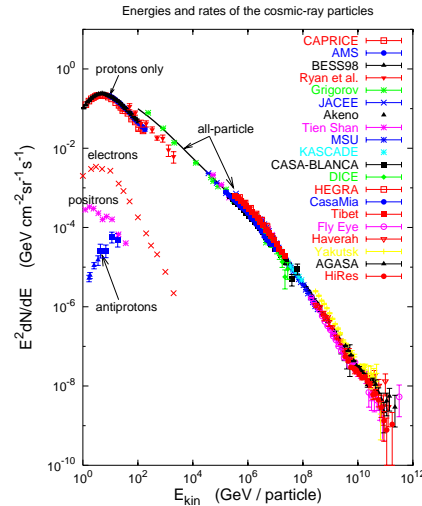
Figure 2.2: Energy spectrum of Cosmic Rays. The differential flux multiplied by E^2 is plotted against the energy [1].

is shown, in a compilation of data from several experiments by Gaisser [1]. This spectrum is quite steep, with the cosmic ray flux falling from one particle per square meter per second for energies of the order of 100 GeV to one particle per square kilometer per century for energies of the order of 10^{20} eV. It follows practically a power law of the form $E^{-\alpha}$, where α is usually referred as the spectral index and is of the order of 3. The spectrum has slight changes in the spectral index, steepening around 3×10^{15} eV and flattening at 3×10^{18} eV. These features in the spectrum are usually referred to as the "knee" and the "ankle", respectively and were first inferred by Khristiansen et al. (1956) and Linsley (1963), respectively. At the far end of the spectrum ($E > 10^{19}$ eV) the available statistic is low, and this has been for a while a controversial region. The far end of the spectrum and its features will be discussed in further detail below. The increase in the number of events in this region and the cross-calibration between different detection techniques is a major purpose of the Pierre Auger Observatory.

2.1.1   The GZK effect

The GZK effect has been predicted by Greisen [2] and, independently, by Zatsepin and Kuzmin [3]. The effect consists in the degradation of the energy of cosmic

rays above a certain energy threshold through their interaction with the Cosmic Microwave Background (CMB) photons. The CMB radiation presents a black body spectrum with an average temperature of 2.73 K and is present throughout the whole Universe with an isotropic distribution. High energy nuclei interact with this radiation and lose energy. The main process for high energy protons is the photopion production. Protons interact with the CMB photons and give a proton plus a pion. The cross section of the reaction rises as the reaction is mediated through the production of a Δ resonance. This effect has an energy threshold of $E \sim 5 \cdot 10^{19}$ eV, and imposes a limit on the mean free path of the protons. In case of heavy nuclei a similar scheme applies but the dominant process for energy loss is the photodisintegration with an energy threshold of the order of $E \sim 5 \cdot 10^{18}$ eV/nucleon. A GZK horizon can be defined as the maximum distance from which 90% of the particles with a given energy greater than the threshold energy can come.

Photons arriving to the Earth suffer an equivalent effect, but the dominant process is pair production in the interaction with CMB photons, making the sky opaque for photons with an energy greater than 10^{14} eV. However, the cross-section for this process will decrease with the increase of the photon energy and the universe will become transparent again for much higher energies.

Figure 2.3, from [4], shows the mean free path for both photons and protons as a function of the energy. As discussed, it can be seen that the mean free path of photons drops for energies of $\sim 10^{14}$ eV, starting to rise afterwards. For protons the mean free path drops at an energy of $\sim 10^{20}$ eV reaching a value of 10 Mpc for energies greater than $5 \cdot 10^{21}$ eV.

2.2 γ rays

The spectrum of diffuse extragalactic photon radiation [5] is presented in figure 2.4 . The energies in the plot range from 10^{-8} eV (radio) to 10^{20} eV. The flux is dominated by the CMB in the microwave region and falls quite rapidly afterwards. For energies above the GeV limits are shown for the γ-ray component. The cosmic ray flux is plotted with open circles for reference.

At such energies the γ-ray diffuse flux is very low and γ-rays are studied by looking at point sources, opening the field of γ-ray astronomy. The first source to be discovered was the Crab nebula. Crab is still the brightest steady emitter for Very High Energy (VHE) γ-rays and is used as a calibration candle. Its spectrum [6], shown in figure 2.5 , extends to several tens of TeV.
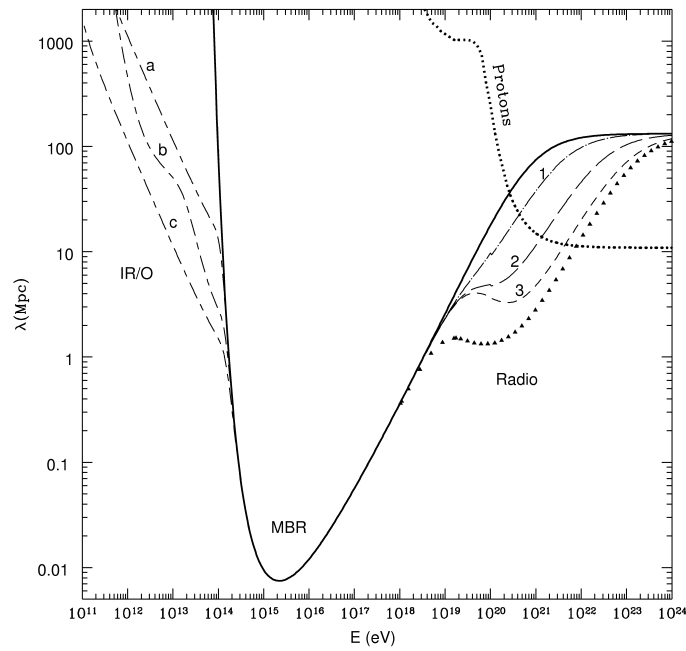
Figure 2.3: Mean free path, λ, of photons and protons as a function of the energy [4]. Photons below 10^{14} eV interact with the Infra-Red and Optical background. Curves a, b and c represent different models of such background radiation; Between $10^{14} - 10^{19}$ eV photons interact with the Microwave Background Radiation. For higher energies the photons interact with radio and the different curves in the plot represent λ under several radio background estimations.
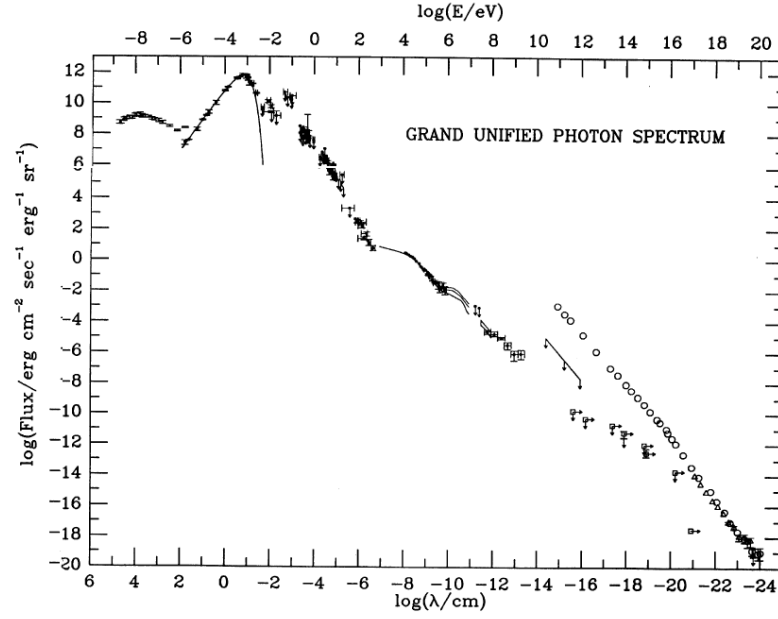
Figure 2.4: The spectrum of diffuse extragalactic photons[5]. For Above GeV energies limits are shown for the γ-ray component. The cosmic ray flux is plotted with open circles for reference.
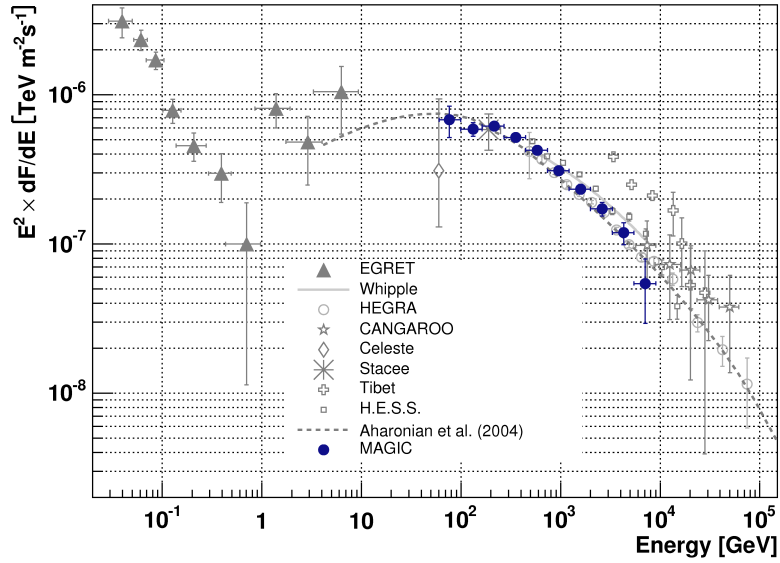
Figure 2.5: The crab γ ray spectrum.

2.3   Extensive Air Showers

It has been known for quite some time that most primary cosmic rays are protons
or heavier nuclei. When these high energy particles enter the Earth's atmosphere
they interact with the nuclei of atmospheric gases and new particles are created
from this interaction. These secondary particles will in turn interact and produce
a new generation of particles. In this way the primary particle gives birth to a
particle cascade. Such cascades develop in the atmosphere as a front of particles
propagating at nearly the speed of light and are commonly known as Extensive Air
Showers (EAS) [7, 8] .

As the primary particle enters the atmosphere and the first interaction occurs,
pions are produced (and also, in lower number, kaons and baryons). Neutral pions
readily decay into a photon pair. Each photon will then disintegrate through pair
production. The positrons and electrons created will in turn produce photons and
the process will go on until there is not enough energy for the production of new
particles. This chain reaction is known as an electromagnetic cascade. Charged pions
have a greater mean lifetime and can interact with nuclei before decaying. There
are also other particles created in the cascade that can originate nuclear interactions
with the nuclei of atmospheric gases. These nuclear interactions originate the hadron
component of the EAS. Charged pions can also decay into muons and neutrinos. The
muons created have such energy that in most cases they will neither interact with the
atmosphere nor decay while traversing it. They constitute the muonic component
of the shower that can be detected at sea level.

Although it is known that the primary cosmic rays are nuclei, their exact nature
is still a point of controversy. For low energy ($E \lesssim 100\,\mathrm{TeV}$) particles the detection
can be performed directly and the composition of cosmic rays is well known. For
higher energies ($E \gtrsim 100\,\mathrm{TeV}$) the detection relies in indirect methods where the
estimation of the primary properties requires the use of interaction models and
Monte Carlo (MC) simulations.

2.3.1   EAS simulation

The analytical treatment of the development of air showers is a complex task, viable
in practical terms only with many approximations and simplifications. Monte Carlo
simulations are in practice the standard method to calculate the properties of EAS.
These MC codes start with the primary particle and simulate the interactions of
subsequent particles along the shower development in the atmosphere. Two of the

main simulation codes are CORSIKA and AIRES. These codes simulate the interactions using different interaction models and follow the particles trajectories in 3D. Such computations for high energies are extremely time consuming, even with state of the art computers. One of the methods for reducing the computing time at high primary energies is the so called thinning method. In this method, below a certain energy only a small fraction of the particles are fully tracked, and they are given a weight to represent the remaining particles. Other simulation codes like CONEX and SENECA take a different approach. In these codes, the particles above an energy threshold are followed explicitly. The numerical description of sub-cascades, initiated by lower energetic particles, is performed using the the solution of cascade equations, reducing the required computation time. [9, 10]

2.3.2 Longitudinal profile

During EAS development particles are created and destroyed. Each particle interacts or decays, giving birth to other particles, each with a fraction of its energy. In this way the number of particles increases. However, low energy particles are easily absorbed in the medium. The number of particles in each step of the cascade will thus be a balance between the creation and annihilation of particles.

Greisen introduced in [11] a parametrization for the total number of electrons in a pure electromagnetic shower initiated by a photon. The shower longitudinal development can be written as a function of the atmospheric depth X as

$$N_e = \frac{0.31}{\sqrt{\beta_0}} \cdot e^{X/\lambda(1-3/2 \ln s)}$$

where $\beta_0 = E_0/\varepsilon_0$, E_0 is the primary energy, ε_0 the critical energy and λ is a characteristic length parameter ($\sim 60 - 70 \, \mathrm{g} \cdot \mathrm{cm}^{-2}$). The shower age s can be written as:

$$s = \frac{3X}{X + 2X_{\max}}$$

where $X_{\max}$ is the depth of the shower maximum - the atmospheric depth at which the shower contains the maximum number of particles. The shower age parameter is 0 for the first interaction point and is 1 at the shower maximum. At $s = 2$ the shower has already died, with N_e evaluating to less than 1.

Gaisser and Hillas presented in [12] (see also [8]) a parametrization of the average number of particles, N, for hadronic showers with a primary energy E_0. It can be

written as

$$N = S_0 \frac{E_0}{\epsilon} \cdot e^{t_m} \left(\frac{t}{t_m} \right)^{t_m} e^{-t}$$

where $S_0 = 0.045$, $\epsilon = 0.074 \, \text{GeV}$, $t = {}^X/\lambda$, λ is a characteristic length parameter ($\sim 60 - 70 \, \text{g} \cdot \text{cm}^{-2}$) and t_m is the depth of shower maximum in units of radiation length. t_m is expressed as

$$t_m = \frac{X_m}{\lambda} = \frac{X_0'}{\lambda} \ln \left(\frac{E_0}{A\epsilon} \right) - 1$$

where A is the atomic number of the nuclei that initiated the shower and $X_0' = 36 \, \text{g} \cdot \text{cm}^{-2}$. The number of particles at the shower maximum is thus proportional to the primary energy and given by:

$$N_m = S_0 \frac{E_0}{\epsilon}.$$

From the previous formulae it can also be seen that the depth of the shower maximum increases with the logarithm of the energy and, for the same energy, it decreases logarithmically with the nucleus mass A.

A slightly modified parametrization known as Gaisser-Hillas function is currently used to describe and fit the shower longitudinal profile:

$$N(X) = N_{\max} \cdot \left(\frac{X - X_0}{X_{\max} - X_0} \right)^{\frac{X_{\max} - X_0}{\lambda}} \cdot e^{\frac{X_{\max} - X}{\lambda}}$$

where $N_{\max}$ is the number of particles at the shower maximum ($X = X_{\max}$). The parameter X_0 is sometimes referred to as the first interaction point although the fit results for this parameter correlate poorly with the actual depth of the first interaction. Figure 2.6 shows the longitudinal profiles for simulated showers with a primary energy of 10^{19}eV. The profiles for iron-initiated (dashed) and proton-initiated (solid) showers are shown. It can be seen from the figure that while $N_{\max}$ is similar in the two cases, iron-initiated showers have, on average, a lower $X_{\max}$. This earlier development of iron showers is a natural consequence of the fact that the primary energy is carried by the 56 nucleons. Furthermore, it is evident that the fluctuations on $X_{\max}$ are considerable lower for iron-initiated showers. This is due to the fact that each nucleon will interact and produce a sub-shower, reducing the overall fluctuations in the shower. Nevertheless, shower to shower fluctuations are large and make it hard to distinguish, on an event by event basis, a proton shower from an iron shower.
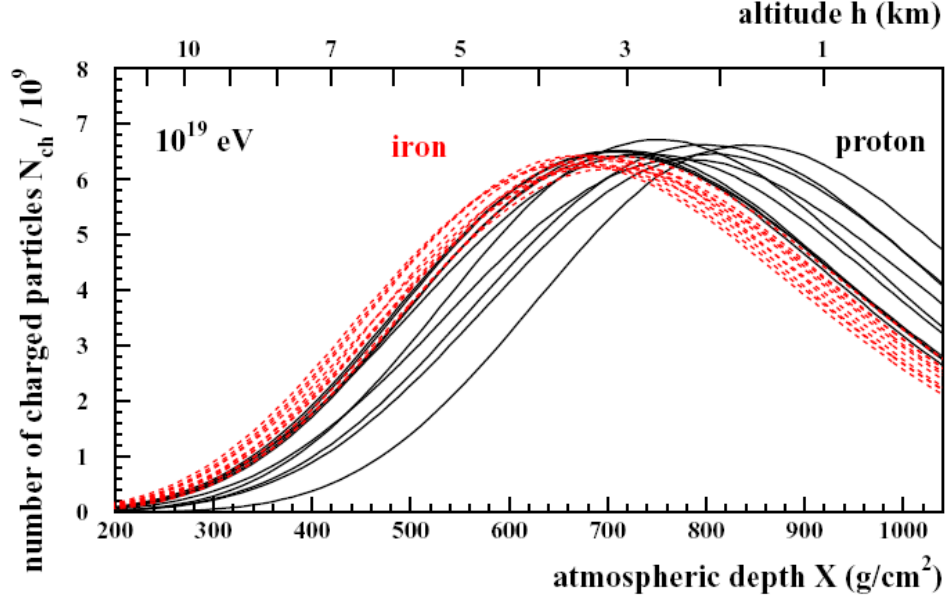
Figure 2.6: Longitudinal profiles for iron and proton initiated showers of energy $E = 10^{19}$ eV.

2.3.3 Lateral profile

In the previous section the longitudinal development of EAS was addressed. Let us now consider the lateral spread of the shower particles. Particles are spread due to multiple Coulomb interactions with the atmospheric nuclei. The cumulative effect of various small-angle scattering interactions builds up the shower transverse structure. The shower can be seen at each instant as a disk, with cylindrical symmetry, which particle density is greater at the center and falls with the disk radius.

The lateral or transverse particle density profile can be parametrised using the Nishimura-Kamata-Greisen function (NKG) [13, 14] that applies to electromagnetic showers:

$$\rho(r) = c(s) \frac{N_e}{r_0^2} \left(\frac{r}{r_0} \right)^{s-2} \left(1 + \frac{r}{r_0} \right)^{s-4.5}$$

with

$$c(s) = 0.366 \cdot s^2 (2.07 - s)^{1.25}$$

where s is the shower age parameter and N_e the total number of shower particles. The parameter r_0 is the Molière radius which is defined as $r_0 = \lambda E_s / E_c$ where λ is the radiation length, $E_s \sim 21$ MeV and E_c is the critical energy. In electromagnetic showers, in average, only 10% of the energy lies outside the cylinder with radius R_0.

The lateral distribution function for hadronic showers can be parametrised having as a base the NKG formula. Greisen [13] presents such a parametrization, where a

E	Nb. events	Thin	Wlim
10^5 GeV	100	0	10^4
10^6 GeV	10	10^{-6}	10
10^7 GeV	10	10^{-6}	10^2
10^8 GeV	10	10^{-6}	10^3

Table 2.1: Characteristics of the produced simulation samples. For each energy two samples were generated with different primaries (proton and iron) using the QGSJET hadronic interaction model.

correction factor appears:

$$\rho\left(r\right) = \frac{C_1\left(s\right)N_e}{2\pi r_1^2}\left(\frac{r}{r_1}\right)^{s-2}\left(1+\frac{r}{r_1}\right)^{s-4.5}\left(1+C_2\left(\frac{r}{r_1}\right)^{\delta}\right)$$

The dependence of the transverse distribution with the primary composition and energy was studied with MC simulations in the context of the possibility to use a fluorescence detector with high angular resolution. This study was carried on to investigate the possibility to use such a detector to measure the lateral profile and thus estimate the primary composition.

The transverse momentum distributions of the secondaries produced in an iron-air collision and in a proton-air collision are not substantially different. However, if the primary has the same energy, the average energy per nucleon is, in the case of an iron collision much smaller ($\sim 1/56$) than in the case of a proton collision. This fact should translate into smaller opening angles of the secondaries for proton initiated air showers and thus into narrower transverse distributions, mainly in the central region of the showers, where the hadronic component is stronger. Statistical fluctuations on the properties of the secondaries from the first reaction are small, as the multiplicity in high energy proton-air collisions is of the order of several tens of particles. However, the magnitude of this effect will depend on the boost and thus on the shower energy.

The CORSIKA [15] simulation package, which is the reference in the field, was used to produce samples of EAS initiated by protons and by iron nuclei with energies ranging from 10^{14} to 10^{17} eV. The QGSJET hadronic interaction model was chosen. For energies above 10^{15} eV the thinning option was used setting the thinning parameter $\varepsilon_{\text{th}} = 10^{-6}$ and applying a weight limit $W_{\text{lim}} = E_{\text{prim}} \cdot \varepsilon_{\text{th}}$, where E_{prim} is the primary energy in GeV. These choices ensure that the fluctuations introduced on the e^+e^- lateral distributions by the thinning are of the order of just a few % for distances to the shower axis below 1000 m. Table 2.1 summarises the characteristics

Observation level	Depth (g/cm²)
1	100
2	200
3	300
4	400
5	500
6	600
7	700
8	800
9	900
10	1000

Table 2.2: Depths of the chosen observation levels.

of the generated samples. The output of each generated event contains information on its longitudinal profile as well as on several transverse profiles at chosen observation levels placed along the shower axis. Table 2.2 summarises the depths of the chosen observation levels.

The lateral profiles near the shower maximum for a proton (solid) and an iron (dashed) event with energy $E = 10^{15}$ eV are shown in figure 2.7 . This plot confirms that the proton lateral distributions are, in the central region, sharper than the corresponding distributions for iron. In figure 2.8 and 2.9 the longitudinal profile of one proton and one iron event, respectively, with an energy $E = 10^{15}$ eV are shown as an example. In the same figures the contributions for the longitudinal profile from the particles with a transverse distance to the shower axis below and above $R_{\text{cut}} = 50$ m are also shown. It is striking that the ratio between these two contributions is well above 1 in the case of the proton-initiated EAS while it is of the order of 1 in the case of iron-initiated EAS. In order to quantify this effect the Rat variable is defined as

$$\text{Rat} = N_{\text{central}}/N_{\text{total}}$$

with

$$N_{\text{central}} = \int_{X_{\text{max}}-\delta}^{X_{\text{max}}+\delta} \int_{0}^{R_{\text{cut}}} \rho\left(r,t\right) drdt$$

$$N_{\text{total}} = \int_{X_{\text{max}}-\delta}^{X_{\text{max}}+\delta} \int_{0}^{\infty} \rho\left(r,t\right) drdt$$

where $\delta = 100$ g · cm^{-2} and $\rho\left(r,t\right)$ is the particle density at a given distance r
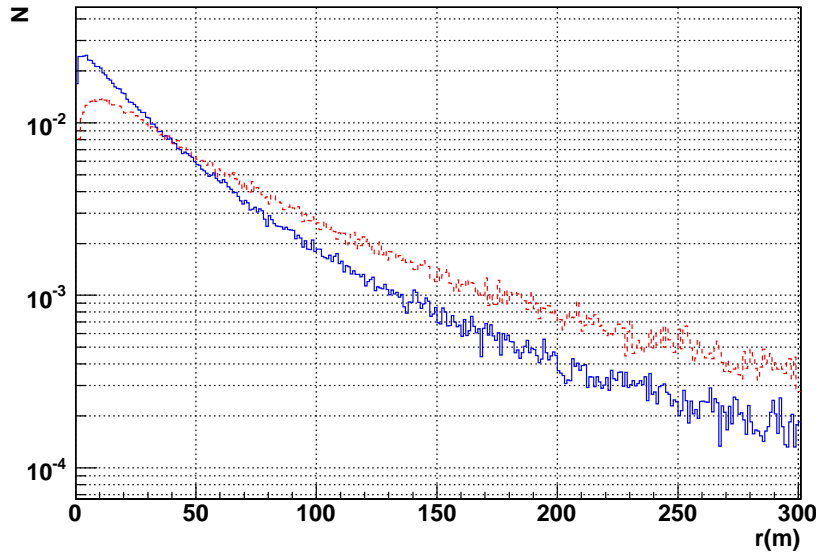
Figure 2.7: Comparison of lateral profiles for a proton (solid blue line) and an
iron (dashed red line) event with energy $E = 10^{15}$ eV near the shower maximum.
The lateral profiles were taken from the observation level nearest to the shower
maximum. In this case the chosen observation levels had a depth of $400\,\mathrm{g/cm^2}$ for
iron and $500\,\mathrm{g/cm^2}$ for proton.
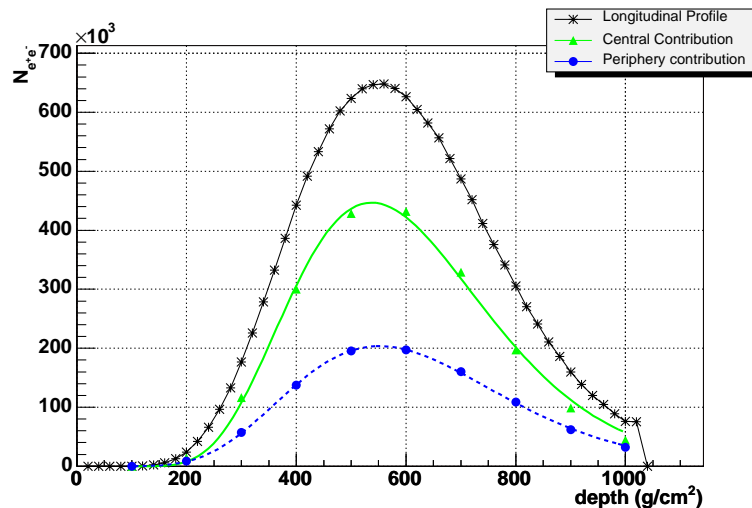
Figure 2.8: Longitudinal profile of a proton event with energy $E = 10^{15}$eV. The total
shower profile is shown, together with the separate contributions of the particles at
a distance above and below 50 m from the shower axis.
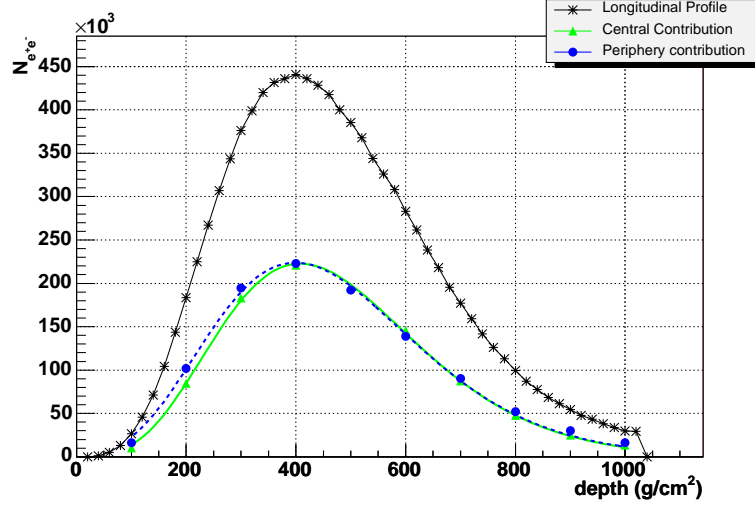
Figure 2.9: Longitudinal profile of an iron event with energy $E = 10^{15}$ eV. The total shower profile is shown, together with the separate contributions of the particles at a distance above and below 50 m from the shower axis.

from the shower axis for a given depth t. Figure 2.10 and figure 2.11 show the distributions of $\mathrm{Rat_{proton}}$ (solid) and $\mathrm{Rat_{iron}}$ (dashed) for energies of $E = 10^{14}$ eV and $E = 10^{17}$ eV, respectively. These Rat distributions were computed for two generated samples of proton and iron EAS, with $R_{\mathrm{cut}} = 50$ m. Figure 2.10 shows a clear separation between the Rat distributions for proton and iron initiated EAS. For higher energies the fluctuations in Rat tend to decrease, decreasing the width of the distribution, as can be seen in figure 2.11. It can also be seen that the difference between the proton and iron distributions tend to vanish with the increase of the energy.

In fact, it has been shown in [16] that at high energies ($\sim 10^{19}$ eV) an universal curve can be used for the description of the lateral profile. In this reference COR-SIKA simulations were used to study the fluorescence emission through the energy deposited in the atmosphere by the cascade. They conclude that the energy density depends only on the distance to the shower axis and on the shower age parameter. It is independent from the primary energy, composition and zenith angle. A parametrization of the form:

$$F\left(\frac{r}{r_M}\right) = 1 - \left(1 + a\left(s\right)\frac{r}{r_M}\right)^{-b(s)}$$

is presented, where a and b depend only on the age parameter s. The parameters
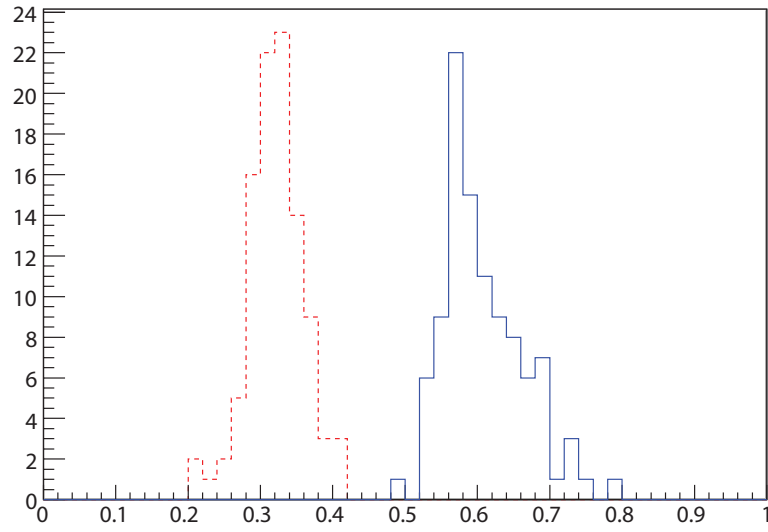
Figure 2.10: Distributions of the Rat variable, defined in the text, for proton (solid) and iron (dashed) EAS generated with an energy of $E = 10^{14}$ eV. For each shower the distribution of particles results from the average of the data between the two observation levels nearest to the shower maximum.
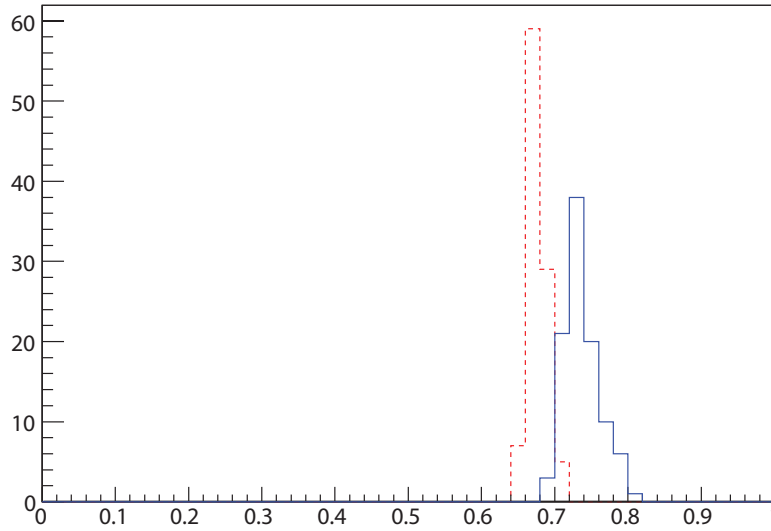
Figure 2.11: Rat distributions for proton (solid) and iron (dashed) EAS generated with an energy of $E = 10^{17}$ eV. For each shower the distribution of particles results from the average of the data between the two observation levels nearest to the shower maximum.

were fitted to the simulation results with polynomials:

$$a\left(s\right) = 5.151s^4 - 28.925s^3 + 60.056s^2 - 56.718s + 22.331.$$

This function is now commonly used in the Auger project to simulate and fit the lateral profile of showers in the fluorescence detector.

2.4 Detection techniques

Cosmic rays can be directly detected at the top of the atmosphere in experiments carried out in balloons or satellites. However the limited aperture of such experiments combined with the rapid decrease of the cosmic ray flux with the energy makes this technique only possible for energies below 10^{14} eV. At higher energies cosmic rays must be studied through the detection of EAS. For this purpose two basic types of detectors are currently used: the ground arrays, based on the sampling technique, and the fluorescence telescopes.

In γ-ray astronomy the fluxes are very much lower than the charged cosmic ray flux. This means that the energy at which ground-based experiments have to be replaced by space-based ones is also lower. For energies up to tens of GeV the detection is space-based, and the most recent and promising experiment is the Gamma-ray Large Area Space Telescope (GLAST[1]) [17] which was recently successfully launched. For higher energies the detection of γ-rays must rely on the detection of EAS. However at these energies the showers do not penetrate deeply in the atmosphere and the most effective instrument for their detection is the Imaging Atmospheric Cherenkov Telescope (IACT), which relies on the detection of the collimated Cherenkov light emitted mainly by the electrons and positrons of the shower in the atmosphere.

2.4.1 Ground arrays

The principle of ground arrays consists of sampling at ground the particle density of the EAS front in order to estimated the primary direction and energy. Ground arrays are composed by a grid of particle detectors. When the shower front crosses one of these detectors, a signal is recorded. This signal is proportional to the local density of particles in the shower front. Mainly two types of detectors are used: scintillators, like in AGASA, and water tanks, like in the Pierre Auger Observatory.

---

[1]NASA announced on 26/08/08 that GLAST has been renamed the Fermi Gamma-ray Space Telescope.

The most widely used scintillators are made of a plastic doped with a scintillating substance. Charged particles deposit energy by ionization and light is emitted by scintillation with an intensity proportional to the deposited energy. Blocks of scintillator are placed in a housing structure along with PMTs. This structure isolates the detector from the outside and directs the light produced to the light sensor (PMT or similar) where it is detected.

In water tanks Cherenkov light is emitted by relativistic particles crossing the detector. The emitted light, basically proportional to the the track length in the water, is reflected in the container walls and recorded using a PMT.

The shower front reaching the detectors is mainly composed by photons, muons and electrons and positrons. Muons penetrate deeply, depositing much less energy by ionization than electrons and positrons. On the other hand, muons cross the water tanks completely, while electrons and positrons are quickly absorbed. This makes water Cherenkov detectors more sensitive to the muonic component of the EAS and scintillators more sensitive to the electromagnetic component.

In both types of detectors the muon flux at the detection level is used to calibrate the detector. The single particle signal is extracted and later used to estimate the number of particles hitting the detector.

The shower front arrival time is recorded at each station with great precision. Assuming that the shower front propagates at the speed of light, the primary direction can be estimated from the time delays in different stations.

The shower size is inferred assuming a lateral shower profile and using it to fit the data from the different stations with signal. The core location is one of the fit parameters and is thus evaluated in the fit. The energy is usually estimated from the density at a fixed distance of the core, extrapolated from the fit. Using extensive Monte Carlo simulations the correlation of this parameter with the primary energy is assessed. The distance at which the density is taken depends on the detector properties, namely the geometry, and is chosen, through MC, as the point where the fluctuations are minimised. For instance AGASA used the density at 600 m from the core, while in the Pierre Auger Observatory, where the detectors are farther away, the signal at 1000 m, $S(1000)$, is used.

2.4.2 Fluorescence telescopes

In the fluorescence technique Earth's atmosphere is used as a calorimeter to study the primary cosmic rays properties. EAS develop in the atmosphere exciting the air molecules. When the molecules, mainly nitrogen, return to their ground state they

emit fluorescence light in the UV, which is detected by means of UV telescopes. Several optics design schemes can be used to build the telescope, but all rely on the use of a large mirror to collect the light and focus it on a PMT camera. Most telescopes are designed to cover a limited field of view and a greater area of the sky is observed by using more than one telescope.

As the atmosphere is used as a calorimeter, a detailed knowledge of its conditions is essential, as the light production and attenuation is related directly to atmospheric parameters. Several atmospheric sensing devices are installed on the Auger site. Weather stations and atmospheric balloons are used to measure directly the atmospheric temperature and pressure. The optical properties of the atmosphere are determined using LIDARs, that measure the scattering in the atmosphere of laser light. Although simple in principle, the solution of the LIDAR equation is not unique and several approximations and assumptions must be made to extract the atmospheric parameters. The detection by the fluorescence telescopes themselves of the light emitted by additional laser devices placed at known distances and scattered in the atmosphere is also used to infer the transmission properties of the atmosphere. Cloud cameras give information on the cloud coverage, extremely valuable for the shower analysis.

Fluorescence telescopes are calibrated using several light sources. Some of these sources are internal and calibrate only the optics and the PMTs of the telescopes. For the Pierre Auger Observatory, an end-to-end calibration device has been specifically developed, which is placed at the entrance of the diaphragm providing uniform and isotropic illumination in the relevant wavelength band. Pulsed laser beams emitted in the field of view of the telescopes are also used for calibration studies.

At each sampling time the EAS is a disk in space, at a certain distance, and illuminates basically a few side-by-side pixels in the camera of the telescope. The image for all samples taken forms a narrow band of pixels with signal, corresponding to the longitudinal development of the EAS. The reconstruction of the shower can be split into two steps: the geometrical reconstruction and the energy reconstruction. An illustration of the geometry used for the reconstruction of fluorescence events is shown in figure 2.12. The line in the centre of the illuminated pixel band and the detector position define the Shower Detector Plane (SDP), the plane in space which contains the shower axis and the detector. The timing information is used to define the shower core coordinates and the shower direction in the plane. The signal recorded by all the pixels can then be used to reconstruct the primary energy. A longitudinal shower profile shape is assumed (usually a Gaisser-Hillas function) and fitted to the light profile, corrected for the atmospheric effects. The integral
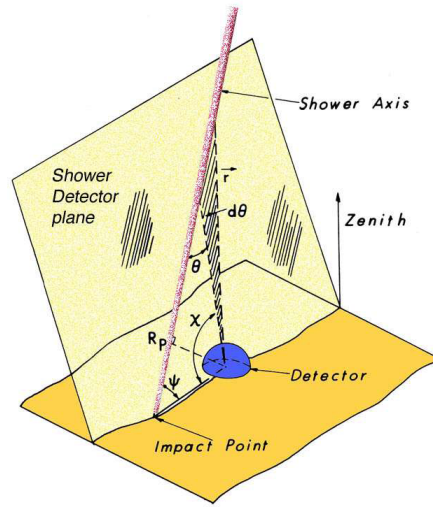
Figure 2.12: Illustration of the geometry used for the reconstruction of fluorescence events.

of the light curve gives an estimation of the energy. This estimation needs to be corrected for the "missing energy" which is the energy carried by particles that do not deposit it in the atmosphere, e.g. the energy carried by the neutrinos, and is usually estimated using Monte-Carlo simulations.

2.4.3 Imaging Atmospheric Cherenkov Telescopes

IACTs are currently the most widely used instruments in γ-astronomy. This technique relies on the detection of the Cherenkov radiation emitted by relativistic EAS particles on the atmosphere. Whereas the particle component does not reach the ground and the fluorescence light is, at the relevant energies, too faint to be detected, the Cherenkov radiation component builds up coherently with the shower front and reaches the ground, where it can be detected.

The detection of cosmic rays using this technique relies on large UV telescopes and arrays of telescopes that are usually characterised by large mirrors and a small field of view ($\sim 5°$).

The telescopes are usually pointed to a known or hypothetical γ-ray source or to specific sky positions as part of a sky survey. If the telescope is inside the Cherenkov pool of light the Cherenkov light is imaged as a filled ellipse in the PMT camera of the telescope. When several telescopes are inside the pool several images are recorded. By analysing the shape and intensity of the signal the parameters of the primary particle are extracted.
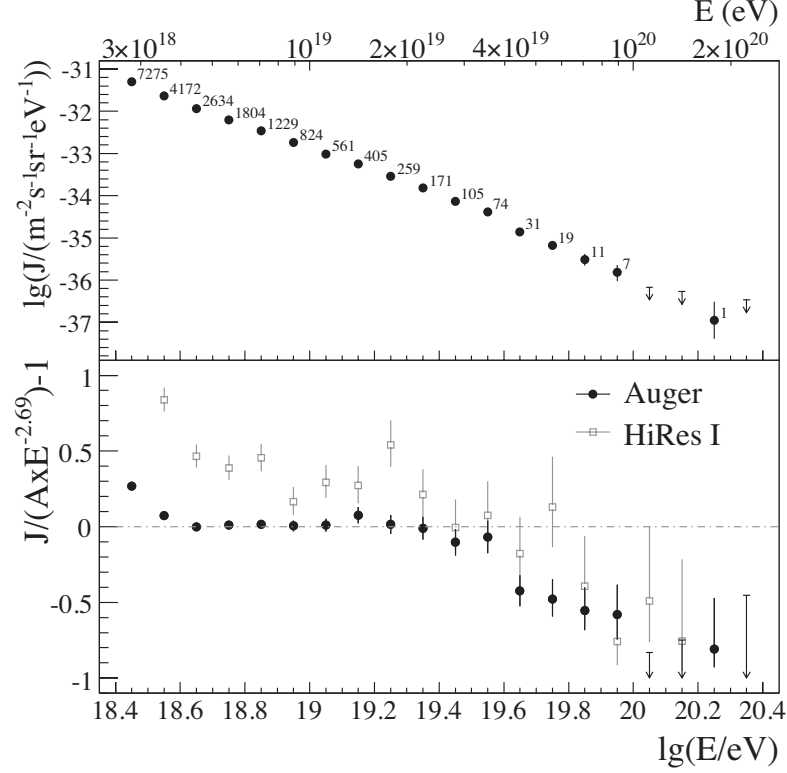
Figure 2.13: The Auger cosmic ray spectrum.

2.5 Recent results

2.5.1 Pierre Auger Observatory results

The first results from the Pierre Auger Observatory include the high energy cosmic ray spectrum, the elongation rate, defined as the variation of the depth of the shower maximum with the logarithm of the energy $(dX_{\max}/d\ln E)$, the photon flux and the cosmic rays arrival directions.

Energy spectrum

The cosmic ray energy spectrum measured by the Pierre Auger Observatory was recently published in [18] and is shown in figure 2.13. In the top panel the spectrum is shown, in logarithmic scale, as compiled from 20 000 events recorded by the surface detector. The bottom panel shows the spectrum as the residual from an assumed spectrum with a power law shape of the form $E^{-2.69}$, making its features more evident. These results show that above $4 \cdot 10^{19}$ eV there is a clear change in the spectral index, corresponding to a suppression of the flux. In the figure, data from HiRes I are also presented, also showing a flux suppression in this energy region.
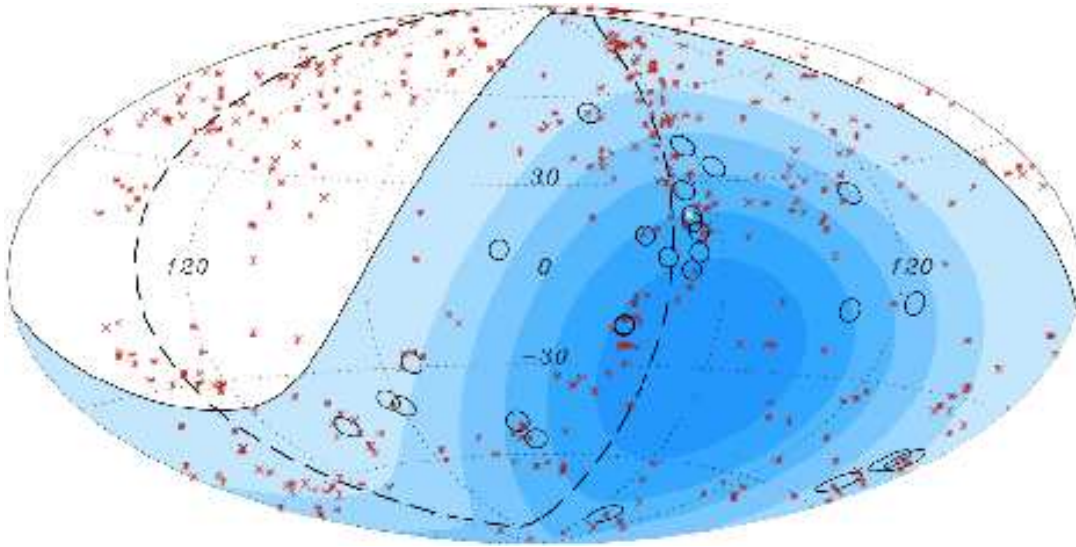
Figure 2.14: The arrival directions of the Auger highest energy events (circles) are
shown. The stars represent the positions of nearby AGNs.

These results are compatible with a GZK-like suppression. It is clear that Auger
results already represent a great improvement in the precision of the measurement
of the spectrum at the highest energies with respect to previous data. Better results
are to be expected in the near future, with the increase in the statistics and a better
control of the systematic uncertainties. Meanwhile, the understanding of the mass
spectrum at the highest energies remains crucial for a full characterisation of the
GZK effect.

Arrival directions

The origin of the highest energy cosmic rays remains an open question. In the
propagation from the sources to Earth cosmic rays are deflected by magnetic fields.
This deflection decreases as the primary energy increases, and increases with the
primary charge. The highest energy cosmic rays are expected to point to their
sources.

The Pierre Auger Observatory has recently [19] established the anisotropy of the
highest energy cosmic rays arrival directions. Figure 2.14 shows the direction in the
sky of the highest energy ($E > 57EeV$) events with circles of 3.1 degrees radius.
These parameters result from a scan in the data collected from 1 January 2004
to 26 May 2006 that minimized the probability that the events recorded resulted
from an isotropic distribution. A prescription was then established and used to
analyse the full data set collected in 3.5 years. The obtained value for the maximum

angular distance is compatible with the expectations for the deflections of protons in the magnetic fields. The relative aperture of the detector is indicated by the shading, with the darker zone corresponding to the higher exposure. The dashed line is super galactic plane. The red stars show the positions of nearby AGNs from the 12th Veron-Cetty and Veron catalog (d<75 Mpc, 472 AGNs) [20]. Analyses have been performed searching for correlations of the arrival direction of the most energetic events with different objects, and in particular with AGNs. The figure shows 27 events, 20 of which are correlated with an AGN within 3 degrees. There is evidence for a correlation with AGNs or with objects with a similar distribution. The accumulated statistics is however still relatively low.

Finally, the pointing accuracy indicated by this correlation seems to indicate that the primaries, at these energies, are mainly protons. Such fact might indeed confirm that the observed suppression of the energy spectrum is due to the GZK effect suffered by protons travelling to Earth.

Elongation rate

The shower development in the atmosphere is influenced by the primary composition. Proton primaries will produce longer showers while showers initiated by iron primaries will develop more rapidly for the same primary energy. A method to infer the cosmic ray composition is the study of the elongation rate, that is, the variation of the depth of the shower maximum with the energy $\left(dX_{\max}/d\log E\right)$.

In figure 2.15, taken from [21], the results from the Pierre Auger Observatory for the average depth of the shower maximum, $\langle X_{\max}\rangle$, as a function of the primary energy are shown. The plot also shows the predictions of different models for iron-initiated and proton-initiated showers. These results show that a single slope would not be sufficient to describe the data, and that the rate of increase of $X_{\max}$ with energy above $E \sim 2 \times 10^{18}$ eV tends to be lower. This seems to indicate a change to lighter primaries up to energies $E \sim 2 \times 10^{18}$ eV and a change to heavier primaries above this energy. More data will however be necessary to establish firmly the high energy behaviour.

This result seems thus in contradiction with the anisotropy results, that indicate proton primaries, and may indicate that the processes involved in the EAS development behave differently from expected. The hadronic interaction models used to simulate EAS are in fact extrapolated from accelerator data to energies several orders of magnitude above, and much is unknown. These results open very interesting particle physics possibilities.
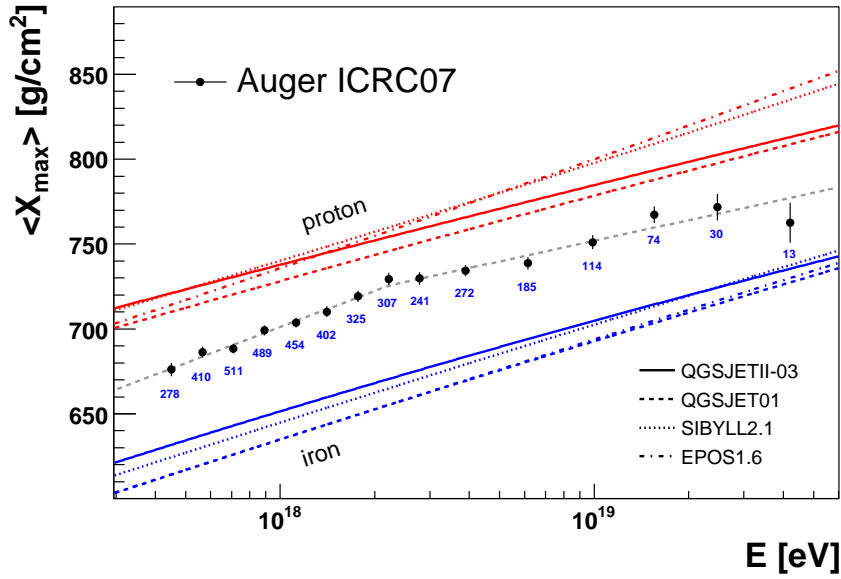
Figure 2.15: The depth of the shower maximum as a function of the energy as measured by Auger is shown and compared with the expectations from different models.

Photon flux

Photon-initiated showers reach the maximum development at much greater depths than proton or iron initiated showers. Using the shower maximum recorded by the Auger fluorescence detector, photon-initiated showers would be distinguishable. The particular characteristics of the development of these shower would also influence the signal recorded by the surface detector of Auger. The shower front curvature and thickness were also used to search for photon shower in the full sample of data.

The data from the Pierre Auger Observatory was searched for photon initiated EAS and no evidence for their observation was found. A limit could then be imposed on the flux of primary photons. These results, presented in [22], are shown in figure 2.16, where the limits on the fraction of photon initiated showers is plotted as a function of the energy along with the predictions of some models. The results from Auger are shown and compared with those from previous experiments. These limits can already exclude most of the top-down models for the creation of high energy photons.

The Pierre Auger Observatory is now fully operational and is expected to collect in one year approximately the same amount of data that was available at the time of the publication of these results. The Pierre Auger results have thus opened a new window for astronomy, astrophysics and particle physics, and very interesting
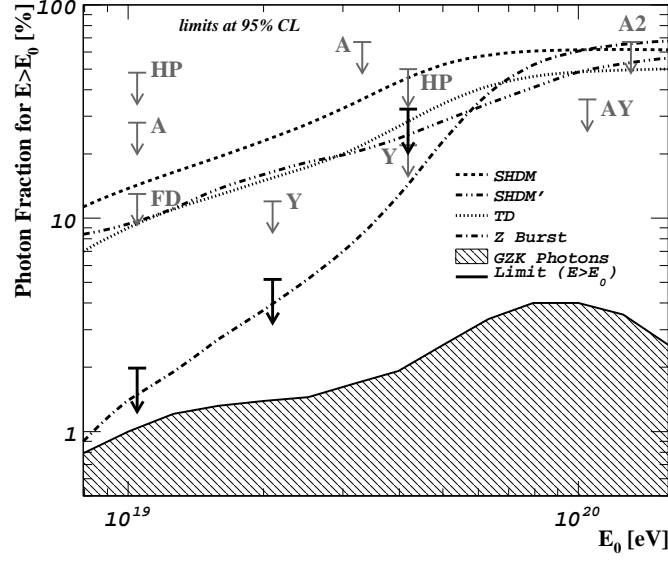
Figure 2.16: Limits on the fraction of photon-initiated showers. The Auger SD (black arrows) and FD limits are shown. For comparison, the predictions of several models and the results from previous experiments are also shown (HP: Haverah Park, A and A2: AGASA, Y: Yakutsk).

results are to be expected soon.

2.5.2 γ-ray astronomy

In recent years the high energy γ-ray field has evolved quite impressively. The advent of new satellite based telescopes like EGRET and AGILE and ground based IACT instruments like MAGIC and HESS allowed the discovery of a large number of sources. A recent and complete review on γ-ray astrophysics can be found in [23]. More than 76 VHE sources have been detected. Their positions are plotted in figure 2.17 . The sources can be identified with several different types of astronomical objects, like Supernova Remnants, Pulsar Wind nebulae and Active Galactic Nuclei. Part of the detected sources is still unidentified. In the figure it is evident that most of the sources lie in the galactic plane. The number of known galactic sources has increased by one order of magnitude in recent years. This comes mainly as a result of a galactic centre survey by the southern hemisphere experiment HESS (see figure 2.18) in the period 2004-2007. The sources accessible from the northern hemisphere were also observed by MAGIC.

The discovery and identification of more sources is to be expected in the near future. GLAST is in orbit since June 2008 and will soon end its commissioning
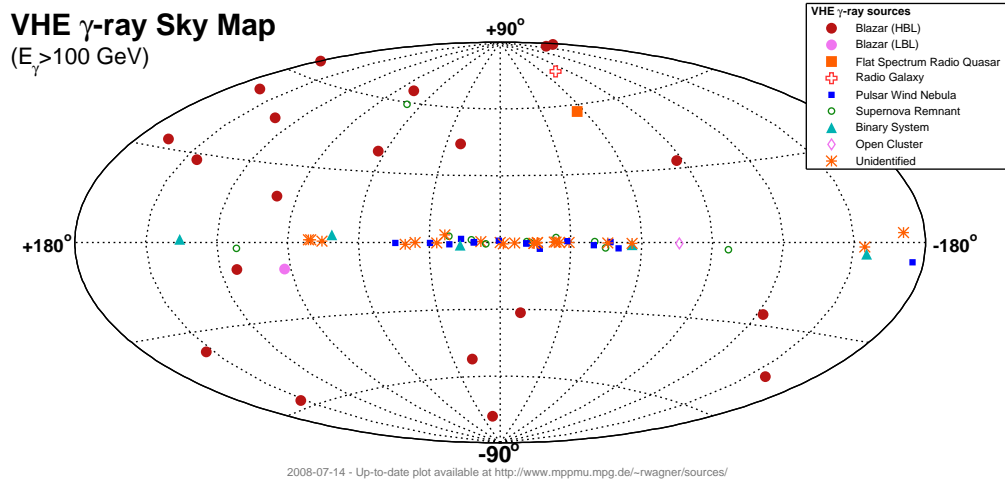
Figure 2.17: Distribution of the detected VHE γ-ray sources [24].
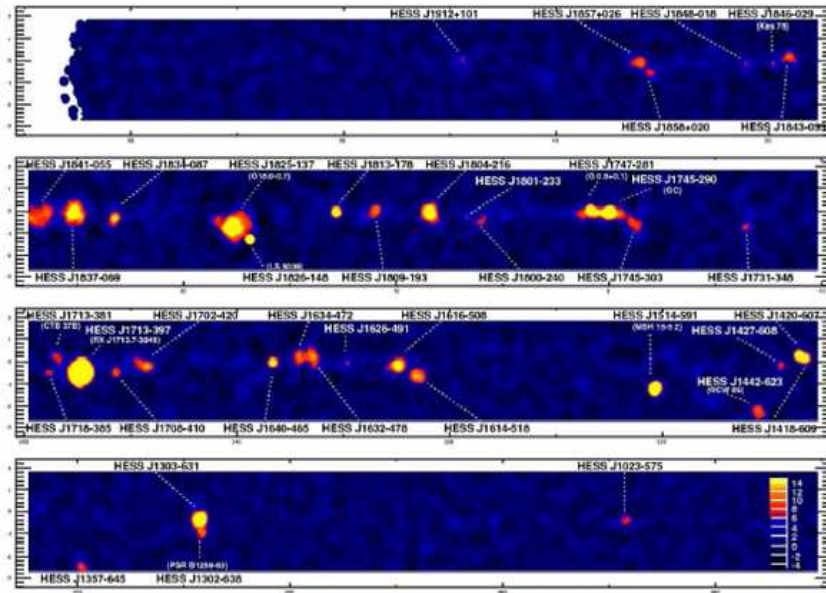
Figure 2.18: γ-ray sources in the galactic plane from the survey performed by
H.E.S.S. [25].

Phase, during which some data were already collected. Ground-based detectors should considerably increase the number of identified source as the present detectors are upgraded. MAGIC will move to its phase 2 with the addition of a new telescope, increasing its sensitivity and angular resolution. HESS phase 2 will count with a very large IACT (28 m) installed at the centre of the array and is expected to inaugurate after 2009, reducing the energy threshold and increasing the sensitivity of the experiment.

Chapter 3

Some Projects Designed to Study High-Energy Cosmic Rays

3.1 EUSO: Extreme Universe Space Observatory

The Extreme Universe Space Observatory (EUSO)[26] was a space mission devoted to the search of Ultra High Energy Cosmic Rays. EUSO was proposed to ESA as a free-flyer mission in January 2000. However, due to an opportunity window, EUSO's installation was redirected to the ISS, on the Columbus Exposed Payload Facility. By December 2000 the study on accommodation of EUSO was finished successfully and the project proceeded to Phase A. Phase A was successfully concluded by mid-2004 and EUSO was considered technically ready to proceed to Phase B. However, due to financial and programmatic issues related to the NASA Space Shuttle program, much affected by the Columbia accident in 2003, EUSO was put on hold. Nowadays two EUSO inspired projects are being considered: JEM-EUSO, a detector similar to EUSO, developed in the context of the Japanese participation in the ISS and Super-EUSO, which has been proposed to the Cosmic Vision program of ESA with a schedule beyond 2015.

The main purpose of EUSO was to collect very large statistics of UHECR at 10^{20} eV, reaching the 10^{21} eV decade, allowing systematic studies on primary cosmic rays composition and origin, while performing an inter-calibration with the Pierre Auger Observatory at energies of 5×10^{19} eV. Searches for highly energetic electron and tau neutrinos could also be performed with EUSO. A secondary objective of EUSO was to study the physical properties of the atmosphere, and related phenomena, including meteors and electrical discharges.

The principle of EUSO, illustrated in figure 3.1, was to observe from space the
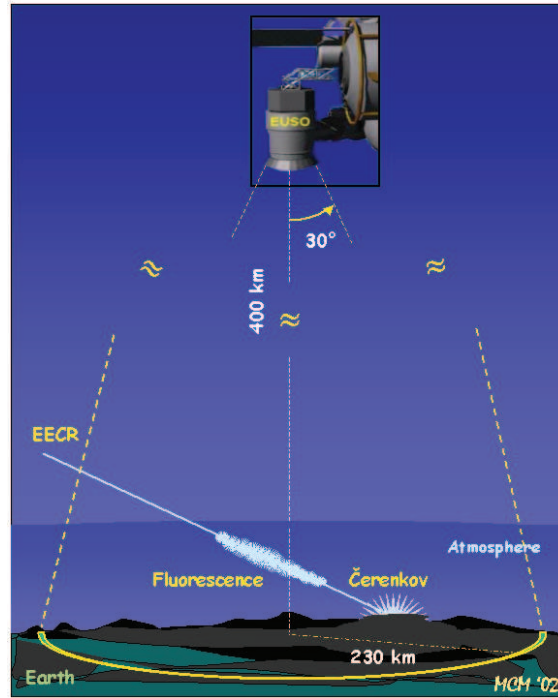
Figure 3.1: The EUSO concept

fluorescence and Cherenkov light produced by EASs in Earth's Atmosphere. The instrument consisted of an UV Telescope to be placed at~ 400 km height (the ISS altitude) , pointing to the nadir with a full field of view of 60°. With such a design, EUSO would have had an observation area of approximately $200\,000\,\text{km}^2$. The ISS, and thus EUSO, have a 51° inclined orbit with respect to the equator, allowing EUSO to observe both hemispheres detecting cosmic rays from all directions in the sky. However, fluorescence telescopes such as EUSO, operate exclusively on moonless nights, which reduces their duty cycle to $\sim 10\%$.

The estimation of the shower energy with EUSO relied on the calorimetric measurement of EAS in the atmosphere. This was accomplished by integrating the detected fluorescence light profile to estimate the energy of the shower. The direction of an EAS can be reconstructed from the fluorescence light distribution on the focal plane and by the timing at which the photons reach the detector. However, being a monocular experiment, there is an ambiguity in the estimation of the height of the EAS in the atmosphere. To solve this ambiguity EUSO relied not only on the detection of the fluorescence light produced by the EAS but also on the measurement of the Cherenkov component reflected from Earth´s surface. The collection of reflected Cherenkov light would also allow for an improved estimation of the location of the EAS core. Thus, the EUSO expected signal, represented in figure 3.2 would
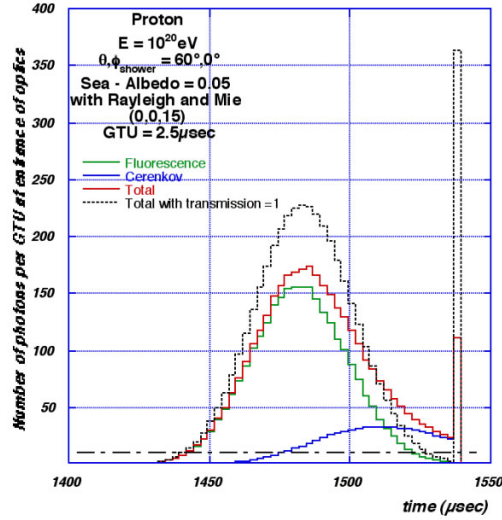
Figure 3.2: Expected signal seen by EUSO

have a fluorescence component followed by a peak of reflected Cherenkov light.

EUSO was designed to have a relative energy resolution of the order of 30%, an angular resolution better than 2° and a resolution of $35\,\mathrm{g\,cm^{-2}}$ in the depth of the shower maximum. Such goals, combined with the limited resources of a space mission installed in the ISS, led to the adoption of a highly pixelated focal surface($\sim 10^5$ pixels), with a high acquisition rate using the Single Photon Counting technique (see chapter 6.2).

The EUSO Detector

An exploded view of EUSO is shown in figure 3.3 . EUSO would be composed by an optical system directing the incoming light to a focal surface where it would be collected by photomultiplier tubes. Although the two fundamental systems in EUSO were the optical system and the data acquisition system, additional subsystems associated with a space experiment conducted aboard the ISS were also incorporated in the detector, such as the interface system to the ISS and the thermal conditioning system. EUSO would also be equipped with a LIDAR to perform measurements of important atmospheric parameters.

Although the definitive detector characteristics were to be defined in the project Phase B some of the important parameters of the design were already established in Phase A: the optical system was composed by two double faced Fresnel lenses. The collecting area of the instrument being defined by a first Fresnel lens with a diameter of 2.5 m, followed by a similar lens placed 2 m away, and 1.5 m before the
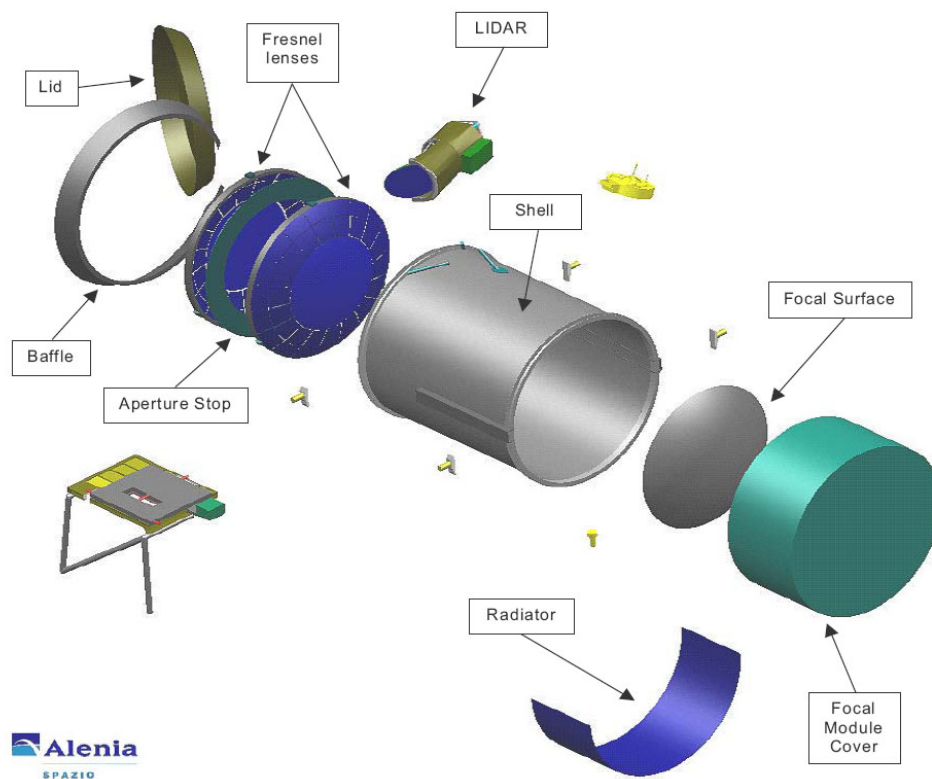
Figure 3.3: The EUSO detector

focal surface. The optical system had to comply with the full field of view of 60°
while producing a spot inferior to 5 mm, corresponding to 0.1°. A bandwidth filter
was deposited as a coating on the first lens to filter light outside the $300 - 400$ nm
wavelength region to remove background.

The focal surface would be instrumented with MAPMTs providing a high density
of channels and the DAQ of the system was based in the Single Photon Counting
technique to instrument such large number of channels ($\sim 10^4$). This technique
employs very simple front-end electronics allowing the reduction of financial, power
and mass budgets, in compliance with the requirements of a space experiment. In
EUSO the pixel signals would be input to a fast discriminator whose output would
feed a counter clock. This part of the system was designed to work with a peak-
to-peak resolution of 10 ns. In each Gate Time Unit (of the μs order) the value
from the counter would be read and the counter would be reset, corresponding to
the acquisition of a number of detected photons per pixel per GTU. The system
would saturate in the of case a bunch of photons arriving within the resolving time
of the system: in fact all photons arriving within 10 ns would be counted as a single
photon. This saturation could be overcome by the digitalisation, through an ADC,
of the last dynode signal of a whole PMT (containing 64 pixels).

3.2   The ULTRA experiment

The ULTRA experiment - Ultra violet Light Transmission and Reflection in the
Atmosphere - was a support experiment for the EUSO mission with the goal of
providing quantitative measurements of the UV light produced by EAS traversing
the atmosphere after reflection on the Earth surface. The ULTRA experiment is
described in [27] and its achievements are reported in [28].

The main concept of ULTRA, illustrated in figure 3.4, was the use an UV optical
detector, the UVScope, to collect the UV light generated by the EAS whose arrival
direction, core location and shower size are estimated using the data collected with a
conventional ground array of scintillators, the ETScope. The UVScope was typically
placed on a high location pointing downward so that its field of view centre coincided
with the ETScope central station, and the UV light reflected from the surface upon
shower front arrival reached the UVScope where it could be detected. Two wide
field of view Cherenkov detectors, "Belenos", were placed in the centre of the array
pointing to the zenith and the nadir in order to measure in coincidence the direct
and diffused Cherenkov light.
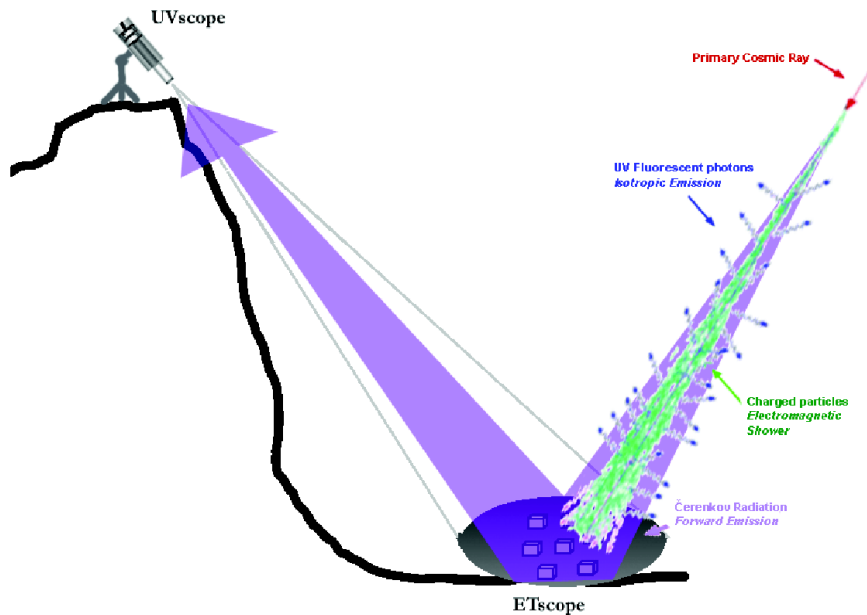
Figure 3.4: The ULTRA operation principle.
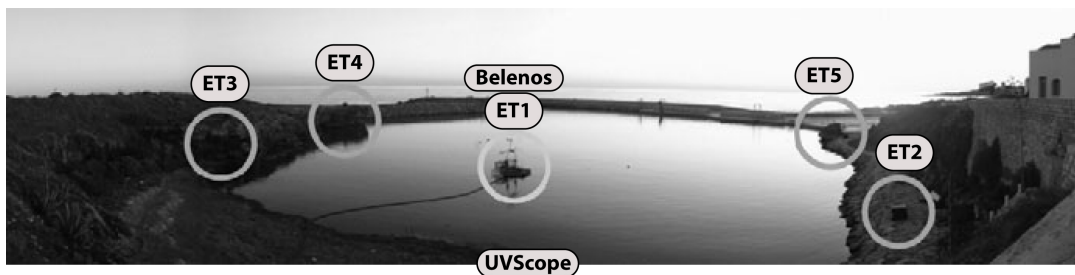
Figure 3.5: View of the ULTRA setup. The ETScope stations are indicated as ET1,
ET2, ET3, ET4 and ET5. The station ET1 and the Belenos detector are installed
in the center of the array in a raft. The UVScope is at a higher altitude pointing
downward. The photo was taken, approximately, from the UVScope position.

The first engineering runs for calibration and optimisation took place at Mont-
Cenis and Grenoble, France, and are reported in [29]. In May 2005 ULTRA was
installed in Capo Granitola, Sicily, Italy, in a protected small private harbour, pro-
viding the conditions to study the reflection of Cherenkov light from EAS on water.
The central station was placed on a raft, along with "Belenos", in the centre of the
harbour. The other stations were placed on shore near the coast line of the harbour.
Figure 3.5 is a photograph, taken from the UVScope location, where the ETScope
stations and Belenos are indicated by circles. The location, in the local coordinate
system, of the several detectors of ULTRA is indicated in figure 3.6

The DAQ used in the successful run in Sicily was based on an acquisition board
developed at LIP - the LIP-PAD board. This board, as well as its application in
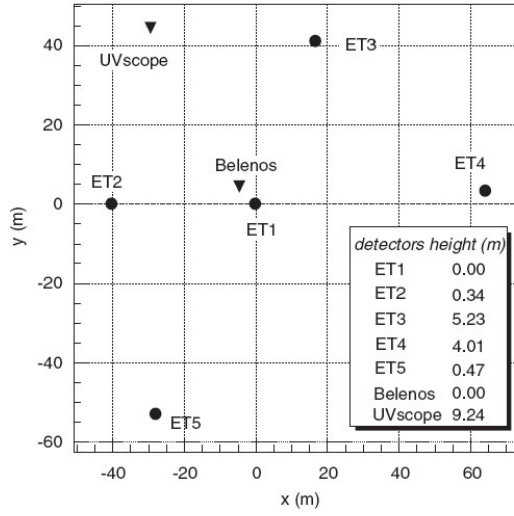
Figure 3.6: The location of the detectors in ULTRA
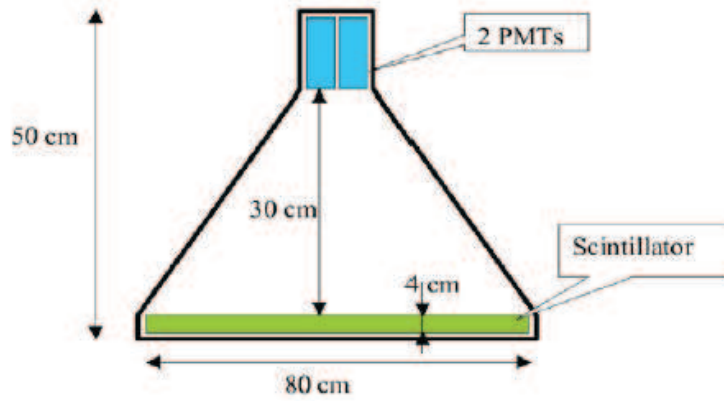
Figure 3.7: Schematic view of one ETScope station

ULTRA, is the subject of chapter 5. Full simulations of the ETScope and of the UVScope were developed at LIP using the Geant4 simulation toolkit [30, 31].

The ETScope detector

The ETScope was a ground array of scintillators used to detect the electromagnetic component of EAS. Each ETScope station estimated the corresponding particle density as well as the shower front impact time. Figure 3.7 represents a schematic view of one station which consisted of a plastic scintillator, NUCLEAR NE 102A with 80×80 cm^2, 4 cm thick, enclosed in an aluminium pyramidal shaped box internally coated with a white diffusing paint. For protection from environmental conditions, each of these boxes was placed inside a PVC container. At the top of the
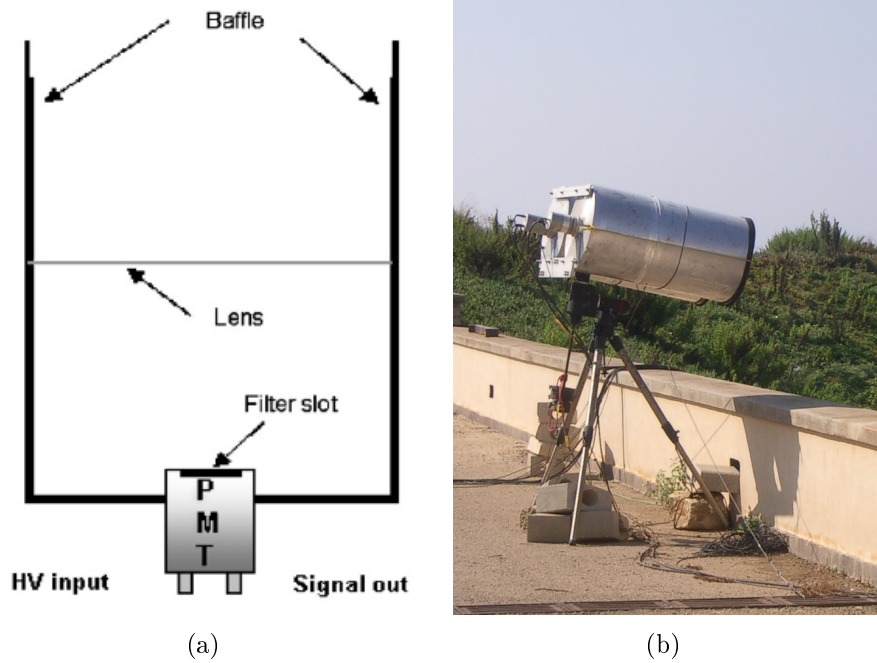
Figure 3.8: The UVScope detector. Left: scheme of each monocle. Right: The binocular detector at Capo Granitola.

pyramidal box there were two co-located Photomultipliers PHILIPS PHOTONICS XP3462B collecting the light generated in the scintillator by charged particles.

In the presented configuration each PMT received, at the same time, approximately half of the light signal and thus the coincidence between the two PMT signals eliminated uncorrelated noise. In shower acquisitions, a larger dynamic range is needed, and one of the PMTs was set to a lower gain. The High Gain PMT was sensitive to low particle densities in the detector. It had a better response in time and was used to perform the trigger logic and to evaluate the difference in timing between the several stations. The Low Gain PMT was mainly used to estimate the number of particles in a station when the high gain PMT saturated. To enable their cross-calibration, the gain of the PMTs was set in such a way that their dynamic ranges overlapped.

The UVScope detector

The UVScope detected the UV light generated by an EAS and diffusely reflected on ground. The UVScope was a binocular instrument with two monocles mounted side by side overlooking the ETScope array. Each monocle, represented in figure 3.8(a), consisted of a lens and a PMT enclosed inside a metallic cylinder. The lens used was a Fresnel lens made of UV transmitting acrylic with a diameter of 457 mm and an

effective focal length of 441.97 mm at $\lambda = 400$ nm. The photocathode of the PMT had a diameter of 68 mm and was placed at the centre of the focal plane defined by the lens. Considering the instrument geometry, its full field of view was estimated to be $\sim 9°$. Figure 3.8(b) is a photograph of the UVScope mounted on a telescope structure in Capo Granitola.

3.3 Gamma Air Watch - GAW

Gamma Air Watch [32, 33] – GAW – is a "path-finder" experiment to test the feasibility of a new generation of Imaging Atmospheric Cherenkov telescopes for the detection and measurement of the Cherenkov light produced by high-energy gamma rays traversing the Earth atmosphere. Traditional Imaging Atmospheric Cherenkov Telescopes (IACT) use large reflective optical systems associated with a PMT camera at the focal surface. These telescopes are designed to search for incoming γ-rays from a given source and have a small field of view (few degrees). Ground based detectors have high field of view and high duty cycle but low sensitivity. Such detectors need acquisitions of several months to detect the Crab Nebula.

GAW adds high flux sensitivity to a large field of view ($24° \times 24°$) capability. In traditional IACT designs the size of the camera necessary to have a large FOV would produce a very large obscuration on the mirror. To overcome this problem GAW uses an innovative approach based on a refractive optical system and a highly pixelated focal surface. In figure 3.9 a schematic view of the GAW telescopes is presented. The refractive optical system is composed by a custom-made 2.13 m diameter Fresnel lens with a focal length of 2.56 m. The lens is designed to have an uniform spatial resolution suitable to meet the Cherenkov imaging requirements up to 12° off-axis. The use of such a system makes it possible to overcome the obscuration problem as well as the optical aberration for large input angles.

The focal surface detector of each telescope consists of a grid of 40×40 Multi-Anode Photomultipliers Tubes (MAPMT). Each MAPMT has 64 anodes, arranged in an 8×8 matrix. The focal surface is operated in single photoelectron counting mode [34] instead of the charge integration method widely used in the IACT experiments. The total array of active channels, $102\,400$ for each telescope, will record the Cherenkov image as a binary image with high granularity, which is fundamental in order to minimise the probability of photoelectrons pile-up within intervals shorter than the sampling time of 10 ns. In such working mode, the effects of electronics noise and PMT gain differences are kept negligible, allowing the photo-
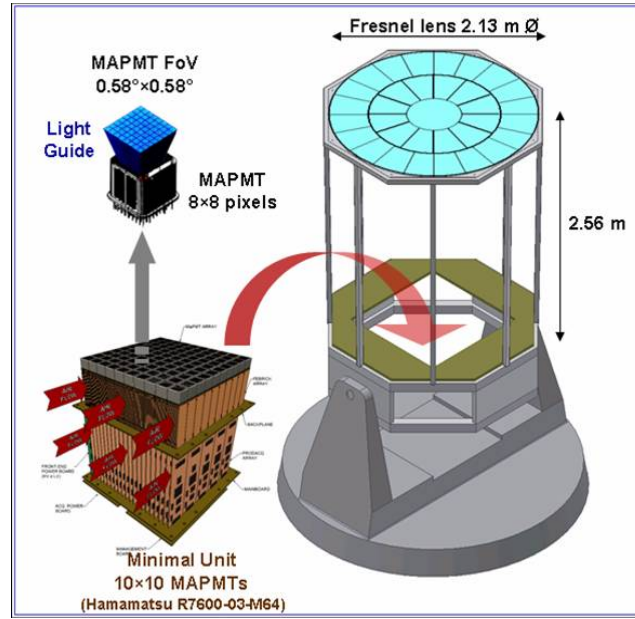
Figure 3.9: Schematic view of one GAW telescope.

electron trigger threshold to be lowered and, as a result, achieving a low telescope energy threshold in spite of the relatively small dimension of the GAW telescope light-collector.

The GAW electronics has been designed to fully match the specific requirements imposed by this new approach. GAW focal surface and acquisition system, including the triggering system are described in more detail in section 6.2.

3.4 The Pierre Auger Observatory

The Pierre Auger Observatory is an instrument designed to measure Ultra High Energy Cosmic Rays providing high statistics at the far end of the CR spectrum. The Pierre Auger Observatory is a hybrid detector composed by a surface array and by a set of fluorescence detectors. A southern and a northern site are foreseen to attain full sky coverage.

The southern site is installed near Malargüe, a small town in the province of Mendoza, Argentina. The site, covering $\sim 3\,000\,\mathrm{km}^2$, was completed in 2008 and it is the biggest cosmic ray detector ever built. The northern site is currently being designed and the corresponding proposal is being finalised. The site will be located in Colorado, USA, near the town of Lamar. It is currently foreseen that the detector will cover $\sim 20\,000\,\mathrm{km}^2$. The first local activity will be the installation of a small surface array for R&D in 2009/2010.
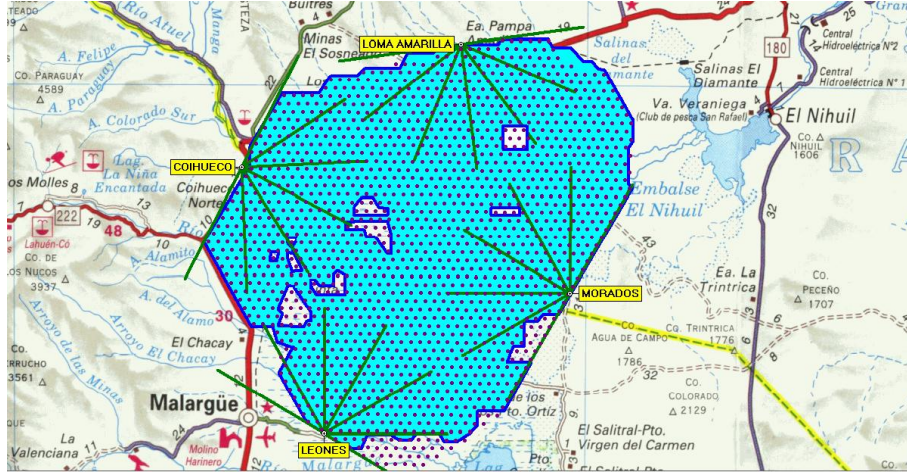
Figure 3.10: The Pierre Auger southern site status in June 11 2008
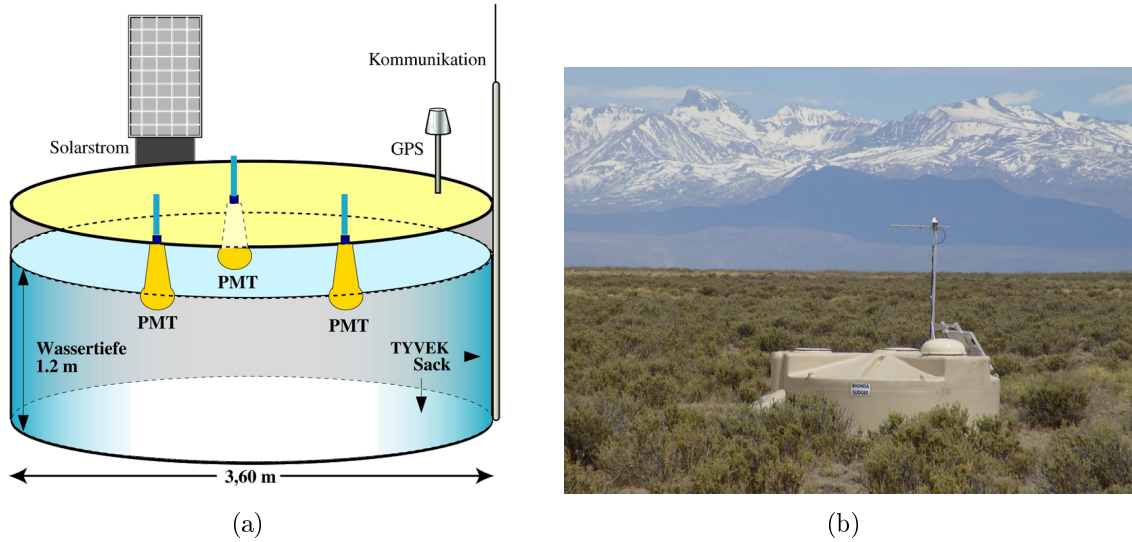
Figure 3.11: Scheme and photograph of an Auger water tank

The status of the Auger South detector in 11 June 2008 is shown in figure 3.10 where the water tank layout, each marked by a dot, can be seen, as well as the four fluorescence eyes and the town of Malargüe. The surface detector is composed by ~ 1600 water tanks. A scheme and a photograph of a surface detector water tank are presented in figure 3.11 . Each tank is a plastic container where an inner liner is installed and filled with purified water, in which Cherenkov light is generated by the relativistic shower particles. The liner is coated to diffusely reflect the light which will arrive at the three Photomultipliers placed on top and be processed by an FADC. Data are recorded and time-tagged with the help of a GPS. The data from each tank is transmitted to the nearest FD site and then to the Auger central campus installed in Malargüe. To minimise the bandwidth only information about

(a)   (b)
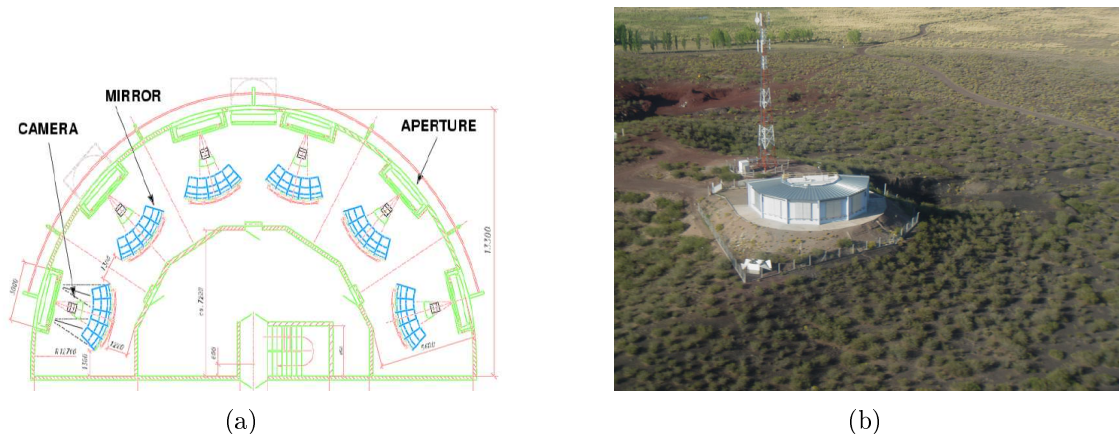
Figure 3.12: Scheme and photograph of an Auger fluorescence eye

the time of the trigger is transmitted in the first step. Using this information, a
central trigger decides if there is an interesting event and the involved stations are
then requested to transmit the whole information recorded for that event.

The fluorescence detector is composed of four fluorescence eyes overlooking the
SD array. Each fluorescence eye, shown in figure 3.12, is composed of six telescopes
having a zenithal field of view of $\sim 30°$ and an azimuthal field of view of $180°$. Each
telescope, figure 3.13, is composed by an entrance filter, a corrector lens, a spherical
mirror and a PMT camera. A detailed description of the fluorescence telescopes is
presented in chapter 7.

The atmospheric conditions influence shower development, fluorescence light pro-
duction and its propagation to the fluorescence telescopes. Therefore, Auger has a
thorough program for atmospheric monitoring, the main atmospheric parameters
being constantly monitored by weather stations. Regular launches of atmospheric
balloons are also performed to record the dependence of the relevant atmospheric
parameters with altitude. Several other apparatus are installed on site to moni-
tor the atmosphere using light: the three main devices are the cloud cameras, the
LIDARs and the Central Laser Facility.

The cloud cameras are infrared cameras installed on top of the fluorescence
buildings enabling the verification of the cloud coverage for the fluorescence events.
The clouds emit more infrared radiation than the cloudless sky, due to the relative
temperature difference, appearing white in the cameras. Each camera is mounted
on a steerable support and acquires images of small parts of the sky, which are
joined, at every 15 minutes, to form an image of the whole sky. The cloud images
are correlated to the field of view of each pixel in the fluorescence telescopes and a
database is filled with cloud coverage information for each particular pixel.
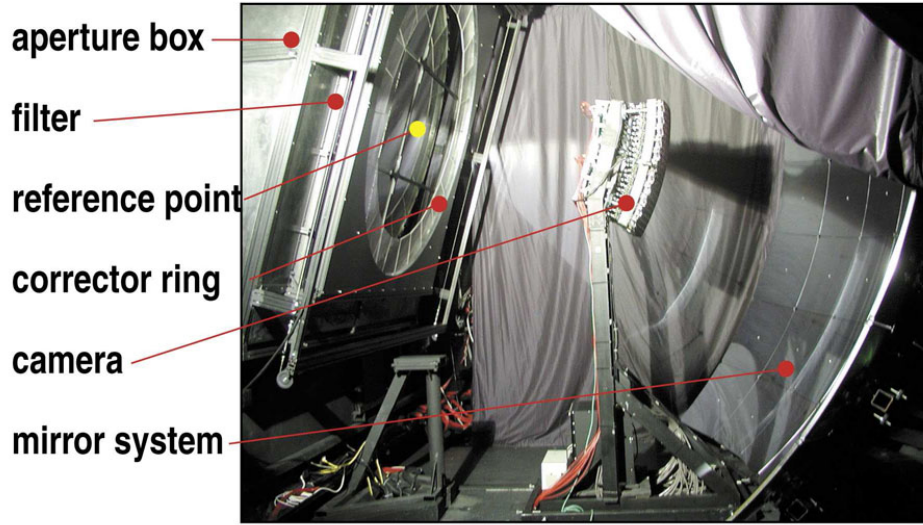
Figure 3.13: The Auger fluorescence telescopes

At the Auger southern site there are four LIDARs, one in each FD site, and a Raman LIDAR installed near "Los Leones" fluorescence detector. The LIDAR uses an UV laser to send short light pulses to the atmosphere which are then scattered. Part of this scattered light reaches the LIDAR station where it is collected using a parabolic mirror and focused into a PMT where it is recorded as a function of time. The LIDAR is mounted on a steerable structure to probe the whole sky. The data collected provide information on the Vertical Atmospheric Depth, aerosol scattering and absorption and can help in the characterisation of the cloud conditions of the sky. Namely, it can provide information on cloud coverage, height, depth and opacity of clouds. The Raman LIDAR is based on inelastic scattering of light and allows more detailed studies on the composition of the atmosphere to be performed. This technique requires a very intense light beam and is only used at twilight when the FD detectors are not operating.

The CLF, Central Laser Facility, is a laser emitter with an energy of $8\,\mathrm{mJ}$ placed in the middle of the array, equidistant from three fluorescence eyes ("Los Leones", Los Morados" and "Coihueco"). The laser propagates in the atmosphere suffering Rayleigh and Mie scattering. Some of the scattered light reaches the fluorescence telescopes. The laser energy is measured and it is set in such a way that the signal recorded in a telescope is similar to the signal emitted by an EAS with an energy $\sim 10^{20}$ eV. The CLF main application is the measurement of the attenuation of light in the atmosphere which depends on the atmospheric conditions. However,

since the CLF provides a controllable source of light, the so-called laser data can
also be used to perform studies of detector performance.

Two new detectors are currently being developed in the Auger southern site.
The Auger enhancements are AMIGA that stands for Auger Muons and Infill for
the Ground Array and HEAT - High Elevation Auger Telescopes. The AMIGA
detector consists of a grid of water tanks - the infill - with half the separation used
in the standard array and also of muon detectors be buried 3 m deep. Due to the
infill, AMIGA will enable the study of cosmic rays of lower energy ($\sim 10^{17}$ eV) and
will also allow to study in detail the muonic component of the showers using the
information from buried scintillators. The HEAT enhancement will extend the field
of view of the fluorescence detector in one eye ("Coihueco") up to $\sim 60°$.

Chapter 4

The LIP e-CRLab

The activities of LIP in the domain of cosmic ray research justified the creation of an electronics laboratory devoted to this field. A proposal to FCT (Fundação para a Ciência e Tecnologia) provided the necessary funds to equip the laboratory. I was deeply involved in this proposal and in the definition of the requirements of the equipment to be installed. The selection and negotiation of the equipment to be bought and the installation of the laboratory were mainly my responsibility.

The Laboratory is named e-CRLab that stands for "Electronics for Cosmic Rays LABoratory. In this section its installation and activities are presented.

4.1 Requirements

Cosmic rays reaching the Earth's atmosphere interact and produce Extensive Air Showers (EAS). EAS produce fluorescence and Cherenkov light that can be detected by UV-Telescopes. The shower front can be sampled at ground by using particle detectors. Most common particle detectors generate light through scintillation or Cherenkov effects which is then collected. Thus many modern cosmic rays experiments rely on the detection of light.

The most commonly used device to detect light produced by the EAS is the PMT. The PMT converts light into photo-electrons that are multiplied to produce an analog output signal. This output signal is usually amplified, filtered and then digitised. From this point onward all the electronics chain is digital. This electronic chain includes memory for the acquired signal and trigger algorithms to reject the noise and background. At some point the electronics must communicate with a computer where data is stored for off-line analysis.

Digital electronics plays thus an important role in data acquisition systems.

Recent technological developments allow the implementation of all-digital logic in a single electronic chip. The FPGA (Field Programmable Gate Array) contains a high number of programmable logic components and programmable interconnections between the logic components. Such devices allow the implementation of complex logic operations using a Hardware Description Language such as Verilog or VHDL. The firmware of such chips can be downloaded to the FPGA using a computer or it can reside in a memory that programmes the FPGA when a reset occurs. The FPGA can even be reprogrammed remotely at run time. Such versatility makes these devices ideal for the implementation of trigger, memory and other digital modules of Data AcQuisition (DAQ) systems.

A digital electronics laboratory is thus justified by the importance that digital logic has been acquiring in DAQ systems. Such laboratories must provide facilities to all development of firmware and to test it in hardware for the correct operation and timings of the devices. A digital electronics laboratory must also make it possible to develop the tools necessary for the testing of the correct operation of digital systems.

The e-CRLab was planned and designed so that the Cosmic Ray groups of LIP could acquire competence in the digital electronics domain. The laboratory was also thought to provide the necessary conditions for teaching and training activities.

Research

The e-CRLab gives support to the LIP group that develops its activities in cosmic rays experiments, namely in the Pierre Auger Observatory (PAO) and in the Gamma Air Watch (GAW) project. The activities in this domain are now centred in the development of firmware for the different components of the DAQ systems and the test, in hardware, of the firmware developed. However, in specific cases, it is also necessary to develop PCB boards for, e.g., the interface of testing equipment with the DAQ boards.

The DAQ systems being developed use fast digital devices with operating frequencies of the order of hundreds of MHz. Technological advances are pushing the operational frequencies of devices even higher. It should be foreseen that, in the near future, DAQ systems will be designed to work at GHz frequencies . Thus the laboratory must be able to cope with the frequencies used nowadays but should, where and when possible, be designed for GHz operating frequencies.

High-density PCB boards developed for high frequencies require complex production equipment. It also requires competence on the most advanced techniques of PCB production which fall outside the scope of the laboratory. However the design

of such boards must be within the competence of the laboratory. Thus a requirement was the availability of a CAD software able to deal with the design of high frequency PCB boards and with the simulation of the circuits. The fabrication of complex boards will be outsourced but, when viable, the assembly will be performed in the laboratory. Thus, it is imperative to have equipment for manually assembling and repairing such boards. The complexity of these boards make it obligatory that the equipment is adequate for assembling components with a high density of pins and small pitch.

In complex digital systems the firmware needs to be optimised and tested through simulation. These features must be present in the development software. The development software was required to be able to deal with high-density FPGA devices and allow for incremental compilation so that design blocks can be created and optimised independently while preserving the blocks already implemented. In complex designs it is also convenient to be able to use off-the-shelf IP cores. Moreover the software should have a timing analyser for the assurance of the different timings through the device. It is also desirable to be able to have an embedded logic analyser and support for integration with external logic analysers.

The test and measurement activities performed in the e-CRLab require equipment both for functional tests and for performance evaluation that is able to work in the hundreds of MHz (preferably in the GHz range). The main items considered were: a logic analyser to deal with many digital channels; a highly performant oscilloscope to characterise the analog signals acquired by ADCs; a signal generator for testing the functionality of the systems; a spectrum analyser for the study of the components of signals and their behaviour on the various part of the electronics systems.

Digital development kits were also required as a test-bench for the development of firmware. Being used to interface some of the DAQ boards, these kits should be highly performant. Preferably these kits should be able to deal with operating frequencies in the range defined previously

Education

The laboratory was planned to give support both to cosmic ray outreach projects and to specific laboratory courses for students of the second cycle of higher education, as defined in the Bologna process. Presently the Cosmic Ray Telescope (TRC) project, an outreach project, and the cosmic ray laboratory, a course of IST, are supported by the e-CRLab. In the second semester of 2008/2009 and in the context

of the Master degree in Physics Engineering from IST, a course in digital electronics named "Projecto e Controlo em Electrónica Digital" will be held at the e-CRLab.

Activities for first cycle students were also foreseen within the research integration of university-level students program supported by FCT. Such activities give the students the opportunity to perform small projects, embedded in a research environment and having an early contact with electronics and FPGA devices. The electronics projects are usually developed in three phases: design; prototyping and testing. Some activities are centred in the development of firmware modules.

The design process of such projects implies no special requirements since optimisation and simulation is not required at this level.

The prototyping to test the adopted solutions can be achieved using bread-boards in an early stage. However the laboratory was designed to have the capability of producing PCB for the prototypes and final versions of the projects. The availability of a CAD software and production machinery was then set as a requirement.

The laboratory needed also to assure the necessary conditions for testing and validating of the prototypes produced. In the education environment emphasis is given to the functionality of the systems developed rather than to the precision and accuracy. The technical requirements for the test and measurement equipment used in education environment were less stringent and a good value for money had to be found.

The existence of a test bench for the development of firmware was also set as a requirement so that such work could be decoupled from hardware development. Such a test bench should be composed by commercially available generic development boards. These boards must have a FPGA implemented and control and display devices to allow the quick development of firmware and functional testing. It was also considered the need for the associated software.

4.2 Installation

4.2.1 Premises

The e-CRLab was physically installed in a space located in the basement of the building where LIP-Lisbon is located. The space is composed by two rooms: one with 18 m^2 and the other with 15 m^2. There is also a small storage room with 2 m^2. The adaptation of the space required small civil work. The works were mainly concentrated in painting and electrical and network installation. Special care was taken with the power installation, namely with the grounding and insulation of

(a) (b)

Figure 4.1: Photographs of the e-CRLab.

the different workstations. A separate electrical ground was installed to reduce the electrical noise present in the electrical network of the laboratory. Groups of power sockets were created, one for each workstation, protected and isolated from each other in the main switch board. The laboratory was installed with workbenches and shelves.

The first space is dedicated to education activities, figure 4.2(a), where up to three groups of two students can be installed. In this space it is also installed the PCB production equipment taking advantage of the existing water and sewer installation. The second room is dedicated to research activities, figure 4.2(b). In this room four workstations are available.

4.2.2 Equipment

One of the key points of the installation of the e-CRLab was the selection of the equipment to be bought. The laboratory was installed from scratch and a whole set of equipment had to be acquired. For more expensive equipment, a preliminary market research was made followed by a budget submitted with the project proposal. Afterwards the items were negotiated directly with the manufacturers. A compromise between the performance and price of the equipment had to be found. A total budget of 80 000 Euro was available. The equipment installed in the laboratory can be grouped as generic, mid-range equipment and state of the art equipment.

The set of generic equipment is composed by mechanical tools, power supplies, a digital workstation for bread board prototyping, a memory programmer, multimeters, a signal generator and 100 MHz digital oscilloscopes. A system for PCB production was installed and is composed by an UV exposure unit, heated process-

ing tanks and a spray etching station (Rota-Station from Mega electronics). The suite Altium Designer was chosen as the PCB design software allowing to design the schematic diagram, route the board, simulate and export to standard format for fabrication. This suite has also the capability for the development of FPGA firmware which is not currently being exploited.

Several digital development kits based on Altera FPGAs were bought. The DE2 (Development and Education Board) from Terasic is a good development platform with a huge set of devices attached to the FPGA. This board will be the standard workbench for education activities. Thus several of these kits were acquired. More performant and specific development boards were bought: Digital Signal Processing (DSP) development kit, Nios Development kit and the PCI development kit. Most of the kits provide already the software from Altera for programming FPGA - QUARTUS II - as well as libraries with IP cores.

The highest performance equipment is exclusively dedicated to research activities and is composed of a 300 MHz bandwidth oscilloscope, an arbitrary function generator with a maximum frequency output of 240 MHz, a spectrum analyser for frequencies up to 3GHz with tracking generator, a 64 channel logic analyser capable of acquiring state data at 235 MHz and has a timing resolution of 125 ps. An oscilloscope with 1GHz bandwidth and a sample rate of 5 GS/s.

A probing system for compact PCB boards is also available in the laboratory. The system is composed of a 32× stereo microscope and four probe heads. The probe heads are fixed to any surface using vacuum and are suitable for probing pads with dimensions down to hundreds of micrometre.

4.3 Research

The research activities are centred on the development and test of firmware for FPGAs. A new version of LIP-PAD is being developed, LPV3. The firmware of GAW data acquisition boards is also being developed and tested in the laboratory

4.3.1 LPV3

The LPV3 is a multipurpose DAQ board with the capability of acquiring six analog signals and perform time synchronisation with an accuracy better than 10 ns. The LIP-PAD and the LPV3 are described in detail in chapter 5. The LPV3 is currently in the development phase. This new board is thought as a completely independent acquisition system capable of acquiring data by itself and send it via network. Many

new features had then to be introduced in the board design. An upgrade of the DAQ part of the board is being carried out to increase its performance. A preliminary design of the LPV3 board was done at the e-CRLab. The work in the e-CRLab was centred in the schematic design of the board and the test of the solutions for the different functionalities introduced. The solutions adopted were tested in simulation and also some components of the system were tested in the development kits available. It is a responsibility of the laboratory to implement the LPV3 firmware and to test the prototype board both for its functionality and performance. The performance test of the DAQ and synchronisation parts of the board assumes critical importance as the operation frequencies of such modules should reach 200 MHz.

4.3.2 GAW boards

Currently one of the activities at the e-CRLab is the development of firmware for the GAW experiment. Namely, the firmware for the digital acquisition board is being developed and tested. This board, named ProDAcq and the electronics of GAW are described in detail in section 6.2. For the interface of ProDAcq with the testing equipment it was necessary to develop a small interface board (LIP-CTRIG) for reading and control of the board. It was also necessary to develop an excitation source and interface (ProDAcq-Excite) for testing the response of the board and firmware to all the possible configurations of the digital data entering the ProDAcq. A first prototype of CTRIG was designed and produced in the laboratory for functionality tests. However the final version of the interface boards were designed at LIP, taking into account the constraints imposed by the high frequencies involved, and produced elsewhere for increased performance. In figure 4.2 a photograph of the prototype (left) and of the final versions (right) are shown.

The LIP group has also taken the responsibility to design and test the firmware for GAW triggering boards. The e-CRLab is prepared to start the test on the boards as soon as they became available.

The laboratory will have a complete acquisition set, provided by IASF-Palermo, composed by a PMT, a FEBrick, a ProDAcq and a trigger generation board. This system will serve as a test bench for a complete test of the acquisition system of GAW. An optical system to stimulate the PMT pixels and test the response of the electronics to different configurations of noise and signal is being studied.

(a)   (b)
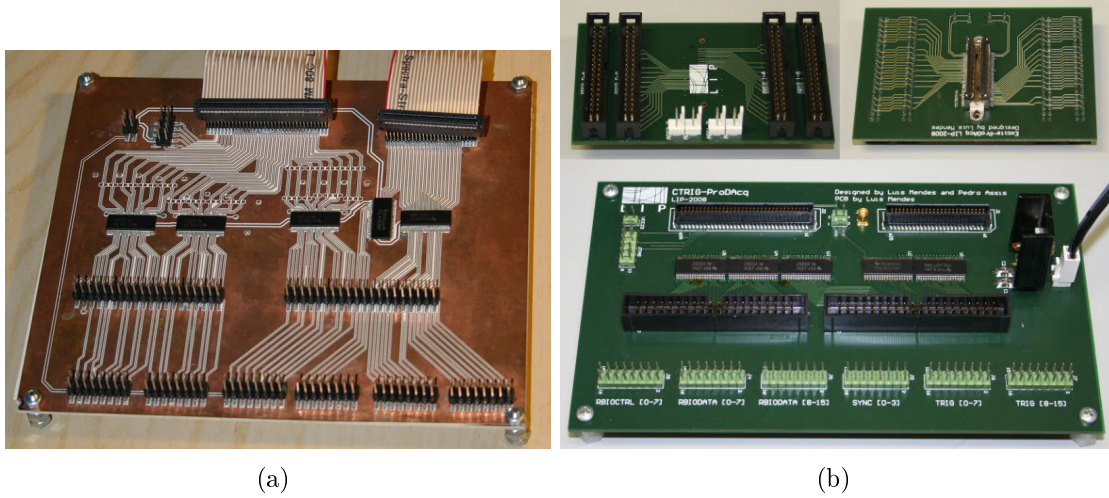
Figure 4.2: Photographs of the prototype of LIP-CTRIG (left) and final version of LIP-CTRIG and ProDAcq-Excite (right).

4.4   Education

4.4.1   Training programs in Digital Logic

Training programs on advanced digital electronics are being organised in the e-CRLab for first cycle students within the FCT program to integrate students in research activities. These activities allow the students to have contact with digital electronics and FPGAs in the first years of their higher formation. Most programs consist on the development of a small project that incorporates the use of an FPGA.

One of the projects that already started with a third year student consists on the development of a display of fluorescence events recorded by the Pierre Auger Fluorescence Detectors. The display consists on a grid of 440 LEDs, emulating the FD camera pixels. Each LED will be lit with an intensity proportional to the signal recorded by the corresponding pixel. The display will be able to show the development of the event in the camera in a time scale perceptible to the human eye. The LED matrix will be controlled using an FPGA development kit. Raw data from selected FD events will be pre-processed to produce film strips. Each frame will contain the signal intensity of each pixel in the matrix. This data will then be loaded in a memory. The FPGA will be programmed to read data from memory and light up the corresponding LEDs. The system should also have a mode in which is shown the integrated pixel signal for an event. One of the open questions still remaining is the emulation of the full geometry of the camera (hexagonal pixel, mercedes, support, etc.) due to its complex geometry.

Another project planned is to develop a PC-based digital oscilloscope using an FPGA and an ADC. For this project the DE2 development kit will be coupled to a data sampling module that will consist on a signal conditioning stage followed by an ADC. The FPGA will then have to be programmed to execute the basic functions of an oscilloscope (acquire ADC data and perform trigger) and communicate the acquired data to a PC. This project will also introduce students to the techniques used in data acquisition systems, namely in the LIP-PAD, a PCI acquisition board developed by LIP.

4.4.2 Course in digital electronics

In the second semester of 2008/2009 a course in digital electronics named "Projecto e Controlo em Lógica Digital" will start in the e-CRLab. The course will be given to fourth and fifth year MEFT students from IST that have already a background on digital electronics.

The course will cover mainly digital systems design using FPGA devices. The course will use the Verilog HDL for describing and implementing logic designs. Students will get acquainted with FPGAs and its programming languages. Logic designs will be developed and implemented in FPGAs and its implementation and performance compared to traditional implementations in bred-board. Students will also explore advanced functionalities of FPGAs and the techniques used for validation and performance tests of the solutions implemented. Namely students will learn how to use simulations and internal and external logic analysers to validate their designs.

Chapter 5

Design and implementation of an autonomous DAQ system

The need to have a simple, low-cost, stand-alone data acquisition system for cosmic ray experiments led to the development of the LIP-PAD board. The DAQ system of ULTRA and TRC were implemented using such boards. A new generation of LIP-PAD, named LPV3, is being developed in order to increase the acquisition performance and its autonomy. The LPV3 will have the capability to control external hardware, to acquire data by itself and communicate the data through network protocols.

5.1   LIP-PAD board

The LIP-PAD board was developed at LIP as a joint effort between the groups working on the ULTRA experiment and on the TRC project. The two main features characterising this board are:

  - sampling, synchronously, analog signals coming from PMTs;

  - time tagging the acquired data using an external synchronisation pulse (e.g. the pulse from a GPS unit).

The board communicates with a PC through the PCI protocol. A brief description of the board and its application in the ULTRA experiment are given in the next sections. A more detailed description of the board and its functionalities was presented elsewhere [29].

5.1.1   Board Description

The LIP-PAD board, shown in figure 5.1, has two main functional blocks: The
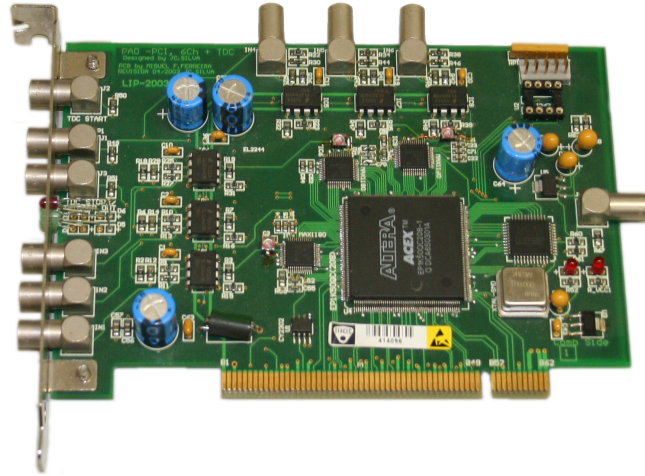
Figure 5.1: The LIP-PAD board (version 2).

Analog Acquisition Sub-system (AAS) and the Time Measuring Sub-system (TMS).
The main component of the board is a FPGA where most of the digital electronic
components are implemented.

The AAS performs the digitisation of analog signals from PMTs. It is composed
of six channels, each having a shaper followed by a 10 bit ADC running at 100 MHz.
The shaper stretches the PMT signal and inverts its polarity as required by the
ADC input. The outputs of the ADCs are directly connected to the FPGA. These
signals are routed internally to the trigger unit and to a buffer memory. A fraction
of a FIFO memory, that is constantly written and read, is used used to buffer the
data. When the triggering condition is met the FIFO memory is filled. In this way
the data acquired will have a pre-trigger and a post-trigger component.

The TMS measures the time between the trigger signal (internal or external) to
an external synchronisation pulse. If this pulse is synchronised to the UTC (as is the
case when GPS signals are used) it is possible to time-tag the trigger signal using
the UTC time. The time measurement is done using a counter and a clock running
at 50 MHz, implemented in the FPGA, and a TDC controlled by the FPGA.

The board has a control unit, responsible for the management of data and oper-
ation, and a PCI client, responsible for the interface with the host computer. The
board is designed so that the FPGA can be programmed by a PROM that will
load its contents to the FPGA when the host PC boots. However the board can
also be programmed using a cable connected to an external PC, making the board
extremely flexible since it can be easily reprogrammed.

5.1.2 Performance in the ULTRA experiment

The LIP-PAD board was the main block of the DAQ system used for the successful run of the ULTRA experiment at Capo Granitola, Sicily, Italy. The run setup is described in section 3.2 and also in [27].

DAQ configuration

The DAQ system was designed to acquire data from different types of detectors used in the experiment. The signals can be grouped in four different classes: high gain ETScope PMT signals, low gain ETScope PMT signals, UVScope PMT signals and Belenos PMT signals.

Each station of the ETScope is equipped with two PMTs that are operated with different gain settings thus extending the dynamic range of the station. The High-Gain PMTs can record the signal from low multiplicity events (down to a m.i.p. signal) while the Low Gain PMTs are able to collect high multiplicity events that saturate the High-Gain PMTs. The gain settings of the PMTs guarantee that the two dynamic ranges overlap, allowing inter-calibration of both PMTs. The lower threshold and faster response of the High-Gain PMTs makes them suitable to be used for triggering and for the estimation of the primary cosmic ray direction which is based on time differences. The synchronisation between the High-Gain PMT signals is thus crucial. The signals from the UV scope are used to measure the UV light reaching the detectors, scattered from the water. The Belenos detectors are UV detectors placed in the centre of the array to collect directly the UV light arriving with the EAS.

Figure 5.2 shows a scheme of the ULTRA DAQ system. In figure 5.3 photographs of the system on-site are shown. The DAQ system consists of four LIP-PAD boards configured in a Master - Slave scheme installed in one PC. The signals from the ETScope PMTs with high gain are connected to one board that acts like the master board. These five signals, connected to the same acquisition board, are acquired synchronously. Since all the channels on the board are sampled using the same 100 MHz clock, time differences between them have a precision of 10 ns. The signals from the ETScope PMTs with low gain are connected to the board slave #1. Slave #2 acquires signals from the two PMTs of UVScope while slave #3 acquires data from the Belenos PMTs. The master board defines a trigger using the information from all the five signals of the high gain ETScope PMTs and sends the trigger signal to the slave boards through a trigger bus. Each slave board receive this signal that act as an external trigger to the board. Although the acquisition is not synchronous
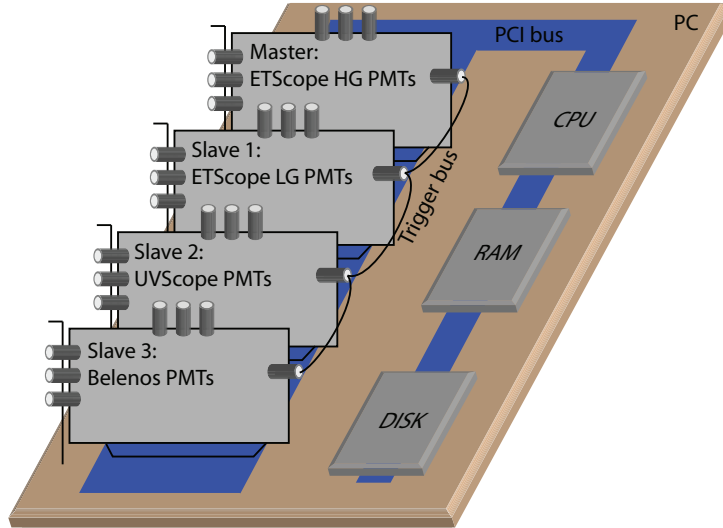
Figure 5.2: Scheme of the ULTRA data acquisition setup. The ULTRA DAQ consists of a PC with four LIP-PADs working in Master-Slave mode
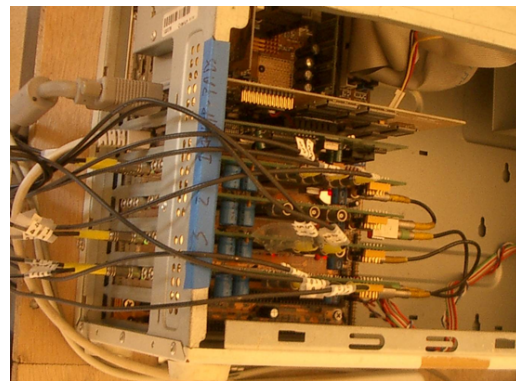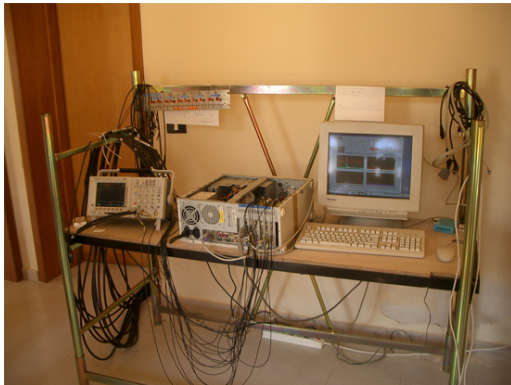
Figure 5.3: Photographs of the ULTRA DAQ at Capo Granitola. Left: Global view of the system. Signal cables arrive from the left and are connected directly to the LIP-PADs. Right: Detail of the four LIP-PADS installed in the acquisition PC.
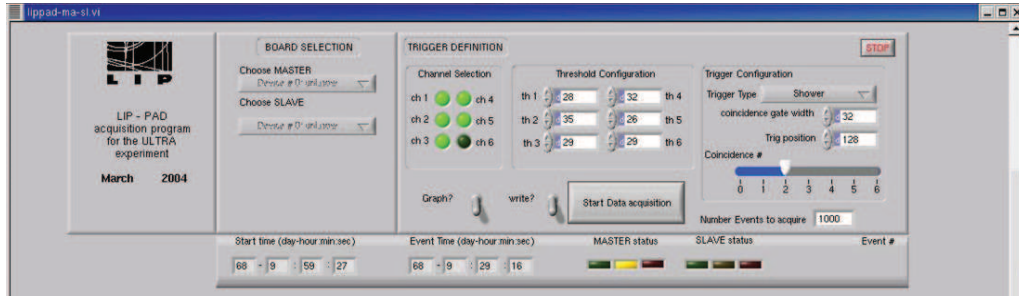
Figure 5.4: View of the GUI of the acquisition program from the Capo Granitola setup. In the figure it is shown the acquisition control menu of the GUI

between the boards, the data are acquired simultaneously within a latency of few tens of ns. This time latency is sufficient to ensure that the data recorded by all detectors belong to the same event.

Trigger system

The Trigger system implemented in the master board FPGA has two levels. The first trigger level consists of a digital threshold applied to the data acquired by each ADC. The threshold for each channel is defined independently from each other. The threshold chosen must take into account the baseline value and the noise of the corresponding channel. The second level trigger is an online logic trigger that can work, basically, in two modes: single event mode and shower mode. In the single event mode a first level trigger from any of the active channels causes the system to issue a trigger signal. In the shower mode coincidences between stations are searched. A first level trigger in a channel opens a time window defined by the user. During this time window each first level trigger signal sets a latch. At the end of the window the number of positive latch outputs give the number of channels with signal above the threshold value during the time window. This number is compared with the required number of coincidences and a second level trigger is issued if the condition is met. At the end of this process the latches are reset.

DAQ software

The DAQ software was implemented in LabView using a PCI driver developed at CERN [35]. The LabView GUI communicates with the LIP-PADs by reading and writing its registers mapped to the PCI memory space. Figure 5.4 illustrates the main screen of the GUI. The GUI allows the user to select the board to be used as master and the boards to be used as slaves, the threshold levels, the trigger

parameters, the file to store data and the number of events to be acquired. When the user starts an acquisition all the boards are programmed with the parameters chosen prior to the start of the acquisition. When the acquisition starts the GUI starts a process of polling to check if the master board has triggered. In this case all the four boards are read and then reset. During the acquisition the user has the possibility to view, in a graphic window, the data acquired by the system. Acquired data is saved in a binary file for offline analysis.

Signal reconstruction

The signal time and charge collected are estimated from the data acquired by the LIP-PAD which consists on a set of signal voltage samples taken in 10 ns intervals. The signal time and collected charge can be estimated directly from the data as, respectively, the time corresponding to the first sample that is above the threshold and the sum of all samples. A more sophisticated approach involves fitting an empirical parametrisation to the data and use the fit result to estimate the signal parameters. The data can be described by an empirical parametrisation of the form

$$V\left(t\right) = C \cdot e^{-\frac{1}{2}\omega^2 \log^2\left(\frac{t-t_0}{\Delta}\right)}$$

where C is the peak amplitude, ω is a shape factor, t_0 is the initial time of the signal and Δ is the rise time of the signal. This formula is fitted to the data leaving these parameters free. A first estimation of t_0 and C is done recurring to the time of the first sample above a threshold and the maximum value recorded, respectively. The parameters ω and Δ are initialized to constant values. The signal time is evaluated using a constant fraction discrimination set at 20%. The time is then given as

$$t_{20\%} = t_0 + \Delta \cdot e^{-\left(2\omega^2 \cdot \log(5)\right)^{1/2}}$$

The collected charge is proportional to the integral of the signal and can be evaluated as

$$Q \propto \int V\left(t\right) = C \cdot \Delta \cdot \omega \cdot e^{0.5\omega^2} \sqrt{2\pi}$$

A sample pulse acquired by the LIP-PAD is represented in Figure 5.5. The plot represents the signal amplitude in ADC units versus the time in 10 ns units. The baseline of the channel has been subtracted from the data. The solid line represent the fit result to the empirical formula.

Figure 5.5: A sample pulse from one DAQ channel is showed. The plot represents the signal amplitude in ADC units versus the time in 10 ns units. A fit is superimposed to the data. See text for details.
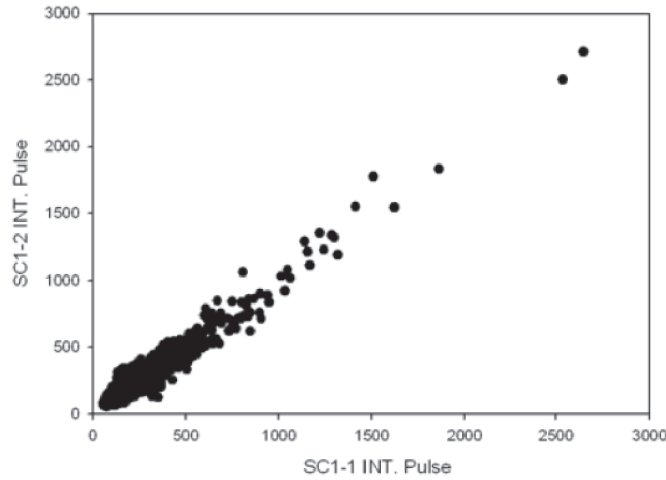
Figure 5.6: Plot of the integral of recorded pulses for PMT2 versus PMT1 in ADC
units. The HV was adjusted so that the gain of both PMTs is the same.

Calibration

The calibration of each scintillator was performed by measuring the Vertical Equiva-
lent Muon (VEM) signal of each scintillator. First, the high voltage power supply of
the low gain photomultipliers was raised so that the two PMTs of each station have
the same gain. Data acquired in this mode is represented in figure 5.6 where the
integral of each recorded pulse for PMT2 of station 1 is plotted against the value for
the PMT1 of the same station. The distribution of the collected charge in single ac-
quisition mode for both PMTs of station 1 is shown in figure 5.7 where the pedestal
peak in the lower part of the spectrum followed by the single particle spectra is
clearly seen. The pedestal, due to uncorrelated noise, was suppressed imposing a
coincidence trigger between the two PMTs as shown in figure 5.8. The value of the
integrated pulse corresponding to the most probable value for the deposited charge
in a PMT, when a single particle crosses the scintillator, was taken as the VEM
calibration constant. This constant allows the collected charge to be converted to
the equivalent number of particles crossing the detector.

Data runs

The data run lasted for seven months from spring to winter 2005. The setup worked
for ~ 309 h and a total of 5682 events were acquired. From these 216 have signal
both in the ETScope and in the UVScope. The data analysis of the collected data is
described in [36]. An example of a "golden" event is shown in figure 5.9. Each graph
shows the signal amplitude recorded by the DAQ system, in ADC units, versus the

(a) SC 1, PMT 1   (b) SC 1, PMT 2
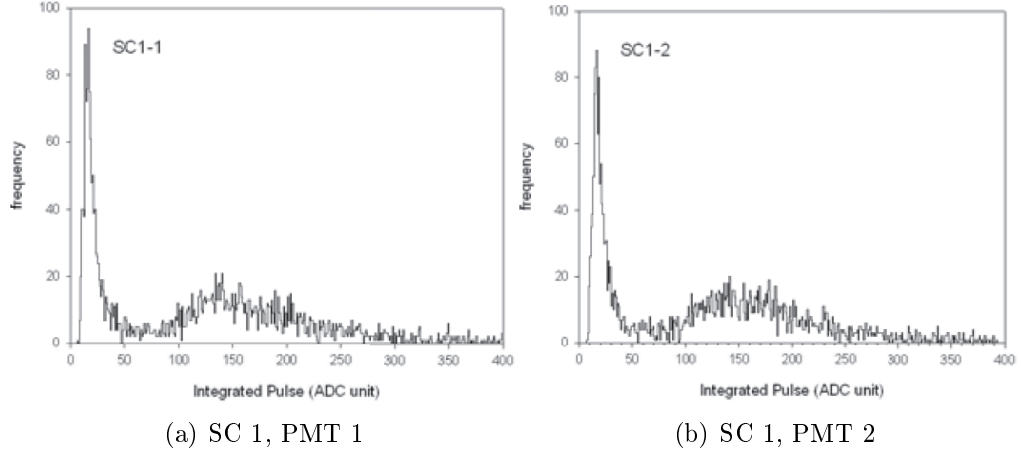
Figure 5.7: Distribution of the integral of acquired pulses in single acquisition mode for both PMTs of station 1. The gain of the PMTs is set to be equal.

(a) SC 1, PMT 1   (b) SC 1, PMT 2
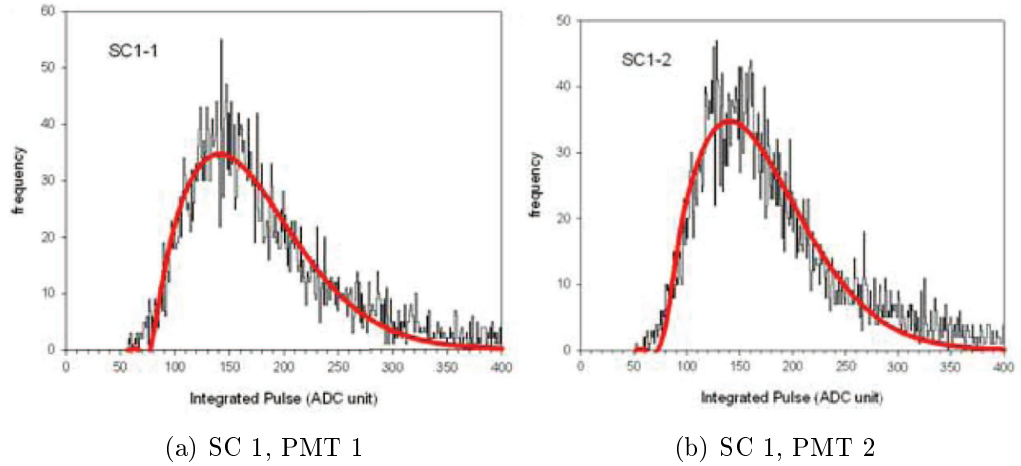
Figure 5.8: Distribution of the integral of acquired pulses in coincidence acquisition mode for both PMTs of station 1. The gain of the PMTs is set to be equal.
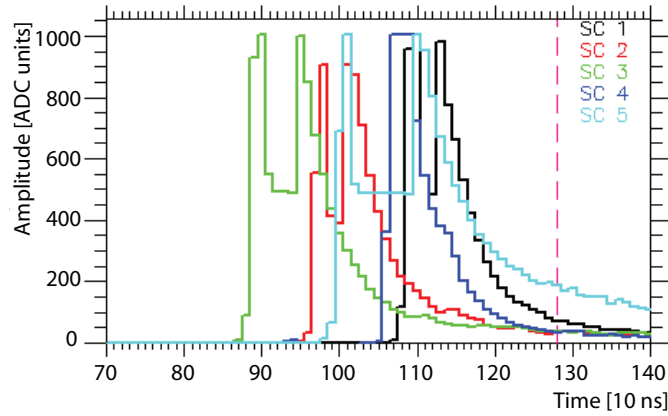
(a) High Gain ETScope PMTS
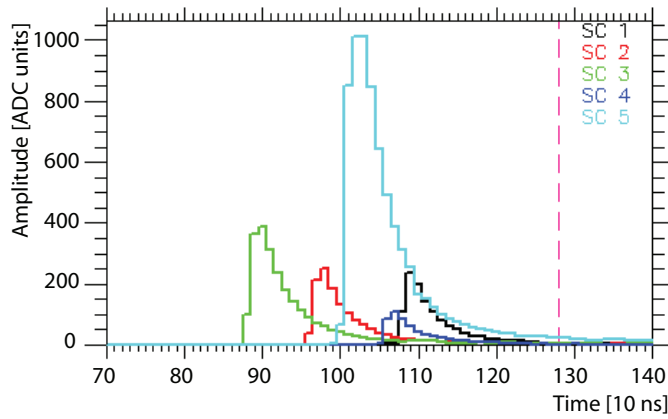
(b) Low Gain ETScope PMTs
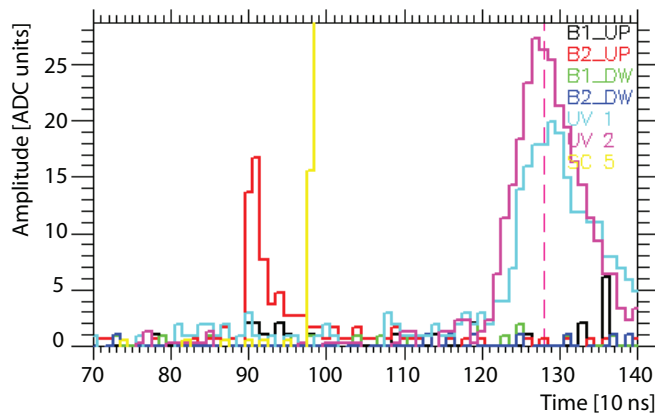
(c) Belenos and UVScope PMTS

Figure 5.9: A sample event recorded by the LIP-PADs. Each graph shows the signal amplitude in ADC units versus the time in 10ns units. (a) shows the signals recorded from the High Gain ETScope PMTs; (b) shows the signals from Low Gain ETScope Photomultipliers; (c) shows the signals from Belenos and UVScope Photomultipliers.

time in 10 ns units. The top graph shows the signal for High Gain PMTs where the saturation of most PMTs is visible. The middle graph shows the Low Gain PMTs signals where no saturation is visible. The bottom graph shows the data collected for the UVScope and Belenos. In every graph the expected time of arrival of the light at the UVScope is marked with a vertical dashed line. It can be seen, in the bottom graph, the good agreement of the collected signal by UVScope with the expected time of arrival.

In previous runs of the experiment a similar system based on LIP-Pads has been tested in comparison with a traditional one based on CAMAC and NIM [29] reproducing the results from the CAMAC system with the benefit of lesser saturation. The experiment gained also the sampling of the signals in time which was not possible with the NIM-CAMAC system. This feature was essential to discriminate particle and diffused Cherenkov light signals in the UVScope. The system proved to be efficient and reliable contributing decisively to the success of the experiment.

5.1.3 Application in the TRC

The Lisbon Cosmic Ray Telescope (TRC) [37] is an outreach project of cosmic ray physics aimed at high school students. The project consists of a network of cosmic ray detectors installed in high schools. Each high school counts with an autonomous detector of cosmic rays composed by three scintillator detectors, usually installed at the roof. The separation between the scintillators is constrained by the space available at the rooftop and is usually of few tens of metres. The network counts also with a central station installed at Instituto Superior Técnico (IST). The distance between the different 9 stations installed at Lisbon ranges from 2 to 10 km. Two other stations are installed in the city of Beja at a distance of ~ 137 km from the central station at IST. The stations can also operate in coincidence mode. In such mode data is acquired simultaneously with a predefined setup and the data can be joined. Using the recorded time for each event coincidences in data can be searched. Recently a test run in coincidence mode was performed with three schools and the central station at IST. A map with the participating stations is presented in figure 5.10 .

Each TRC station has a DAQ and control system, illustrated in figure 5.11, that consists of a LIP-PAD installed in a PC. The system controls the HV power supplies through an I2C link. The I2C protocol is emulated using the parallel port of the acquisition PC. The GPS communicates with the PC by an RS232 link connected to the serial port. The PPS signal from the receiver is connected directly to a

Figure 5.10: Map of the three schools and the central station at IST that participated in the run in coincidence.
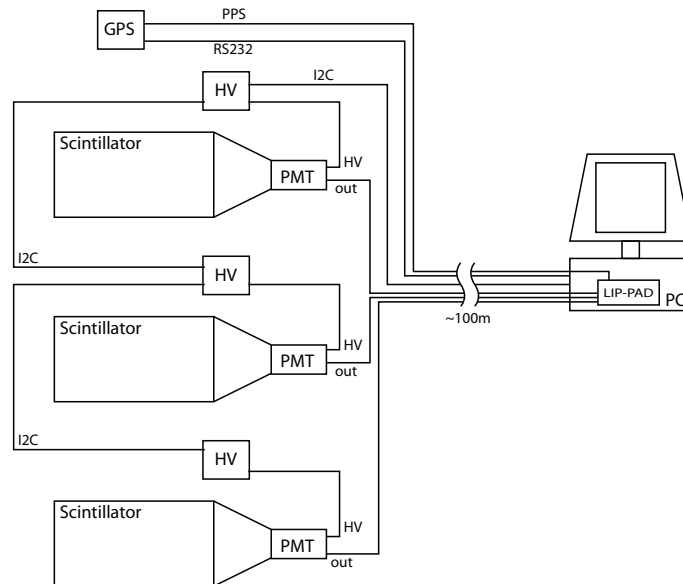
Figure 5.11: Scheme of the DAQ and control system installed in each station of the TRC project.

digital input of LIP-PAD. Each PMT signal is connected to an analog input of the LIP-PAD.

The detector is usually placed in the roof-top of the school while the DAQ system is placed in a room with restricted access. Thus, the detectors have a large separation from the DAQ and control system. The cabling of one TRC station comprises 3 signal cables, one for each PMT, a PPS cable, a RS232 cable, an I2C cable and one for 12V power supply. The distances involved in cabling are quite large, of the order of 100 m.

The main problems that arose in the TRC DAQ and control system are related with the time-tagging and the operation system stability and robustness. The problems in time-tagging derive from the performance of the DAQ PC that manages the TMS and the GPS. The time-tagging system requires that the time information stored in the LIP-PAD is combined with the GPS information received by RS232. The PC must also read and reset the timing registers of the board. Due to the high load of the DAQ polling process some times these operations are not performed within the necessary time causing the time-tagging system to fail.

Operation stability and system robustness of the TRC needs to be improved. Problems in the DAQ PC are common. Problems in cabling are also an issue to be addressed. The long distances involved complicate the system debugging, namely for cable testing

5.2 LPV3 (Lip-Pad Version 3)

A new DAQ board is being developed. This board is designed to be a complete DAQ and control system, thus eliminating the need for a DAQ PC, for small cosmic ray experiments that use up to six photomultipliers. Although inspired by the LIP-PAD board it is designed from scratch since all the elements have changed and some were added. This is reflected in the name LPV3 that derives from the acronym - LIP-PAD version 3.

5.2.1 Requirements

The LPV3 has evolved from the LIP-PAD board. LPV3 is intended to improve the performance of the LIP-PAD. Namely it has to meet two main requirements: operate in an autonomous way and improve the signal reconstruction with respect to the previous version. It is also expected that the new design will increase the maximum acquisition rate of DAQ systems based in the LPV3.
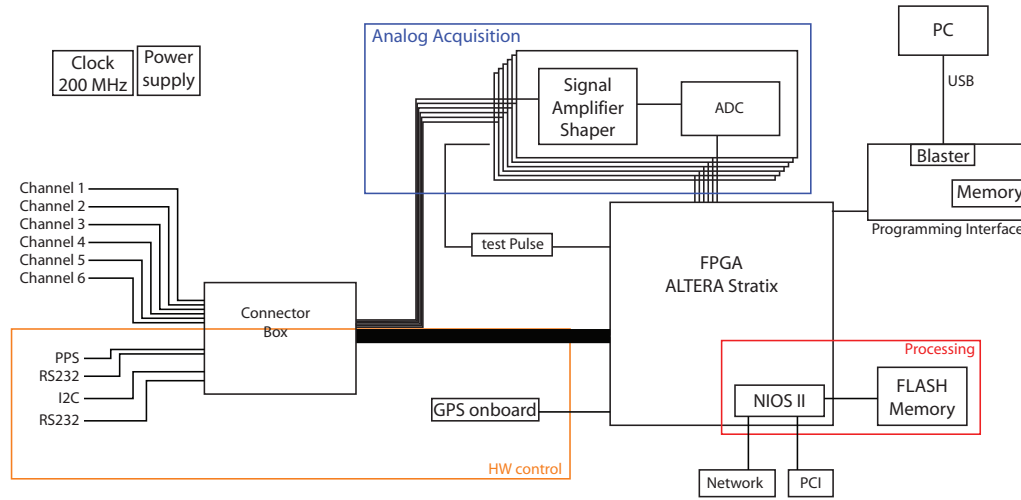
Figure 5.12: LPV3 block diagram

LPV3 is designed so that it can operate without being installed in a PC. In this case the control and read-out are performed using a network connection. In order to be a full DAQ and control system, the LPV3 must also control other hardware devices. Typically, cosmic rays experiments use PMTs, high voltage power supplies, GPS systems for synchronisation and weather stations that need to be interfaced by the LPV3. For this purpose standard protocols will be implemented (RS232, I2C). A general purpose Input - Output bank is foreseen so that other protocols can be implemented.

The communication through network and the ability to control other hardware implies that the LPV3 has processing capability and storage. This will be accomplished with the use of an embedded processor in the FPGA and an external memory.

The second main objective is to improve the estimation of each signal parameters: time and collected charge. This issue is addressed in two ways: (i) the sampling frequency and resolution of the ADC will be increased in LPV3 and (ii) the analog input stage will be redesigned so that the output signal of this stage will have a predefined shape and duration in response to a fast PMT pulse. The shaping parameters result from a compromise between having enough samples for the fitting procedure and the loss in time accuracy.

5.2.2 Design Options

The new LPV3 board will be implemented following the design requirements expressed in the previous section. Figure 5.12 shows the block diagram of LPV3. The main blocks of LPV3 are: programming interface; processing; analog acqui-

sition; hardware control; network interface; PCI interface. The implementation of these main blocks will be discussed in the following paragraphs. The core piece of the board will be the Altera Stratix FPGA[38] that provides sufficient resources to implement all the digital electronics of the board working at the required frequency.

Programming interface

The FPGA of the LPV3 will be able to be programmed using a cable connected to an external computer or by a memory. When the memory is used, the data contained in the memory will be transferred to the FPGA when the board is reset. The memory is non-volatile and can be reprogrammed using the external cable. This scheme will give total flexibility to the board. A stable configuration can be loaded in the memory, development firmware can be tested by reprogramming using a cable and the updates to the board firmware will then be performed by simply reprogramming the internal memory.

Processing

The imposed requirements forces the board to have processing capability. This will be achieved by implementing a NIOS processor in the FPGA. The board must be able to run acquisition software and to store the acquired data before sending it through network. A flash memory will be installed to store both the acquisition program and the acquired data. Flash memory was chosen because it is non-volatile and thus the acquisition program will be saved even without power.

Analog acquisition

The analog acquisition block is an essential part of the system and it is the one with more pressing requirements. As it can be seen from the block diagram (figure 5.12) this block is composed by six analog acquisition channels. In each channel there is an analog input stage followed by an ADC. The design of the analog input stage is not finalised as some of the solutions need to be tested in hardware. A prototype of LPV3 will be made with no signal conditioning stage. Instead the board will have a connector with the input, output and power lines. The signal conditioning stage will be then implemented in separate boards that will connect to the LPV3. In this way the different solutions will be tested. It is still to decide if the signal conditioning will be incorporated in the final version of the board or if the connector will be maintained. In this case the boards can be customised with different shaping and amplification circuits. However the connector might introduce more noise in

the analog channels than a standard solution and the final design requirements is
pending on the good performance in the prototype tests.

Hardware control

The board will be able to control several hardware. The LPV3 will have two RS232
connections, one I2C bus and an input line for the synchronisation signal. The GPS
unit will be controlled by RS232. Under study is the possibility to embed the GPS
in the LPV3 using a matching connector to the Motorola m12+ family of GPS. The
free pins of the FPGA will be used as general purpose I/O. These I/O lines will be
grouped in a generic connector. Several protocols can be implemented afterwards
in the firmware. A connector box will allow to interface the different connectors of
the protocols implemented.

Communications interface

The LPV3 will communicate both by PCI and by ethernet. The implementation of
the PCI will follow very closely the implementation of this protocol in the LIP-PAD
using the standard 32 pin 33 MHz PCI. The ethernet communication has already
been tested in development kits from Altera that include this protocol. In the kits
the NIOS and a driver for the implemented hardware was used. The hardware
implementation in the LPV3 will then be inspired in this design and will use the
same ethernet controller chip.

Chapter 6

Design and implementation of trigger algorithms in single photon counting systems

In this chapter the work carried out to develop Data Acquisition systems for detectors using the Single Photon Counting Technique with emphasis on the GAW project is presented. More specifically, the work on the trigger system and the development of firmware for the GAW electronics is reported.

6.1 Single photon counting systems

Single Photon Counting (SPC) is a well-established technique for the detection of very faint light levels [39]. For faint light levels, photons arrive individually to the photocathode of the PMT. For each photon a voltage pulse will be produced by the amplification chain of the PMT. Therefore, in the photon counting mode, individual pulses can be detected using a simple threshold. The number of detected pulses is an estimator of the light arriving to the PMT.

The front-end electronics based on the SPC technique is very simple and usually makes use of amplifiers and comparators to transform analog signal pulses into digital pulses by setting a threshold. This technique is very effective [40] in terms of stability, detection efficiency and signal to noise ratio, on the condition that pulses are properly resolved within the maximum frequency of the system. Unlike the charge collection technique, in which the analog signal is digitalised, there is no information about the amplitude of each signal. Consequently if several signal pulses arrive within the time resolution of the system they will pile-up and the system will

only count one photon. The phenomenon is usually named photon pile-up and is related to the saturation of the system.

The SPC technique is suitable for the instrumentation of the focal surface of a detector if the signal will not produce pile-up. This can be achieved by lowering the pixel size, and thus increasing the number of pixels, and by increasing the acquisition frequency. The use of such simple electronics allows the use of a very high number of acquisition channels with very good time resolution.

The triggering system of such detectors using the SPC technique are usually implemented with several levels. The first trigger level can be considered as the threshold applied to the analog signal. Higher trigger levels include the definition of a minimum number of detected photons at a given pixel, and algorithms that analyse the characteristics of the signal. The top level triggers analyse the pattern produced in the pixels, the number of photons detected, and its evolution in time allowing the elimination of the random and uncorrelated background events.

An analog acquisition system, with the same performance, would increase the information collected and thus represent a better DAQ system. Such system could be implemented using an integration ADC with a small gate defined from a fast threshold, by a flash ADC running at high frequency or by a peak-sensing ADC. However such solutions represent an enormous increase in the price and power consumption per channel. The design of an acquisition system will have to make a trade-off between the acquired information per channel and the number of acquisition channels. The performance of similar Imaging Atmospheric Cherenkov telescope layouts, using different approaches for the front-end electronics, has been studied and compared at the level of the trigger efficiencies and energy thresholds in [34]. The results obtained clearly favours the option for a focal surface with high pixelisation using the Single Photon Counting technique.

The Single Photon Counting Technique was adopted for the EUSO detector. EUSO is basically an UV telescope with a highly pixelated focal surface and aims to detect the fluorescence light from cosmic rays showers in the Earth's atmosphere. The high number of channels, the low light level produced by cosmic rays and the constraints imposed to space based experiments in terms of power, weight and telemetry led EUSO to adopt the Single Photon Counting Technique for the instrumentation of its focal surface.

In the focal surface of EUSO an Extensive Air Shower is imaged as a spot whose intensity and position evolves with time producing a track. High-energy shower events are clearly distinguishable from the background and a simple signal persistency trigger can be used. For lower energy events ($< 10^{20}$ eV) the signal to noise
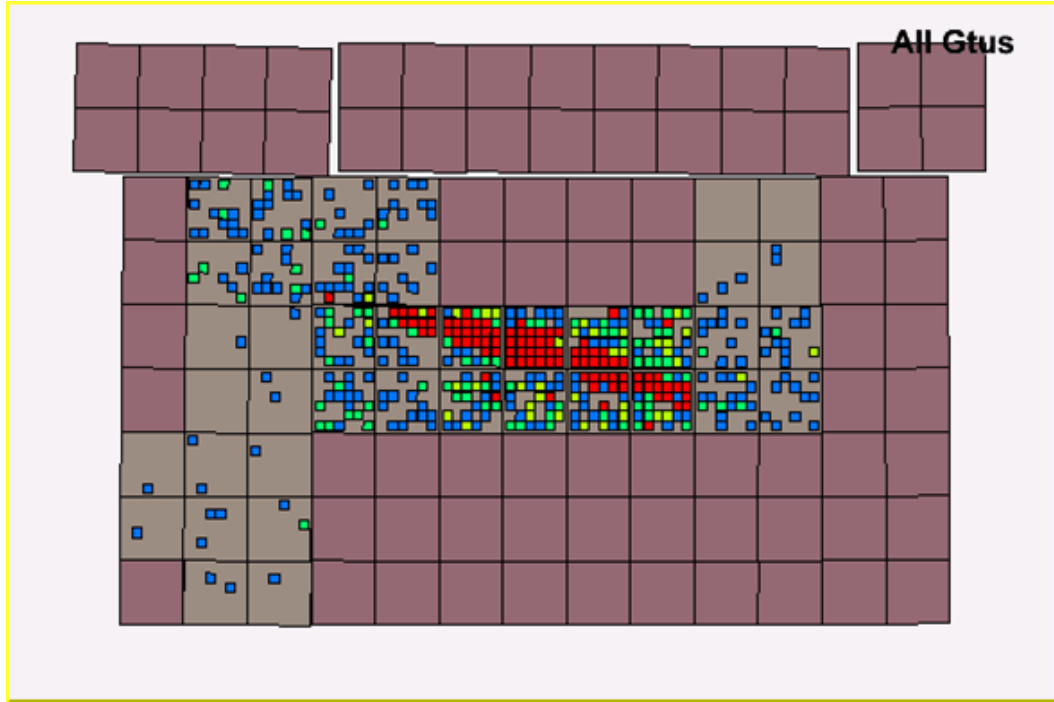
Figure 6.1: Simulated Shower in ESAF. Each big square represents a MAPMT while the small pixels represent the pixels. Active pixels are presented in colour which represents the number of collected photons.

ratio is reduced and the detection of the signal must rely on the identification of its properties, namely the space-time patterns, that differ a lot between events and background.

The EUSO trigger has been designed to provide a good discrimination of shower events from the background for energies as low as possible ($\sim 5 \cdot 10^{19}$ eV). An analog threshold is used for the definition of the single photon pulses. The pulses are counted in a time window and a digital threshold is used to define an active pixel. The second trigger level is a contiguity trigger that identifies the pattern of a cosmic ray in the focal surface of EUSO. The trigger is performed online and searches for a continuity of a line in time. This is done by searching if in consequent time frames there are adjacent pixels with signal. Such a scheme can be implemented using very simple electronics. The triggering system is described in detail in [41].

The triggering system simulation was firstly studied using IDL at Palermo [41]. It was implemented in the Euso Simulation and Analysis Framework (ESAF)[42, 43] at Lisbon and a first validation of the simulation was performed and reported [44]. Figure 6.1 represents a simulated shower using ESAF that met the trigger condition as implemented in the simulation. In the context of the study of cosmic ray space detectors, the performance of the detector was assessed, using ESAF, in more detail

in [45].

Unfortunately external conditions prevented EUSO to advance to the phase B of the project, although phase A was concluded successfully. During phase B the detector system was to be refined and the concrete implementation of its electronics system designed. The triggering system was to be studied more in depth, its parameters fine tuned and its implementation designed taking into account the constraints imposed by the electronics system foreseen.

The same approach of EUSO was applied in the context of an Imaging Atmospheric Cherenkov Telescope with large Field of View capability - the Gamma Air Watch (GAW) project. The DAQ and triggering system of the telescope, where the LIP group has taken particular responsibilities, will be discussed in the following section.

6.2 Data acquisition and trigger in the GAW experiment

GAW, described in section 3.3, is a wide field of view Imaging Atmospheric Cherenkov Telescope. GAW uses an innovative approach for the collection of Cherenkov light generated by EAS, in particular the Single Photon Counting Technique to acquire light signals.

6.2.1 Requirements

The GAW electronics has been designed to fully match the specific requirements imposed by the new proposed approach. A large number of active channels constitute the focal surface of the GAW telescope making it basically a large UV sensitive digital camera with high sensitivity and time resolution. The GAW electronics design is based on single photoelectron counting method [34](front-end) and free running method (data taking and read-out)

6.2.2 Electronics Layout

GAW Focal Surface Detector, represented in figure 6.2, is formed by an array of Multi-Anode Photo Multipliers (MAPMTs) coupled with the electronic instrumentation, UVIScope (Ultra Violet Imaging Scope), capable of conditioning, acquiring and processing, at a high rate, a large number of high speed pulse signals.
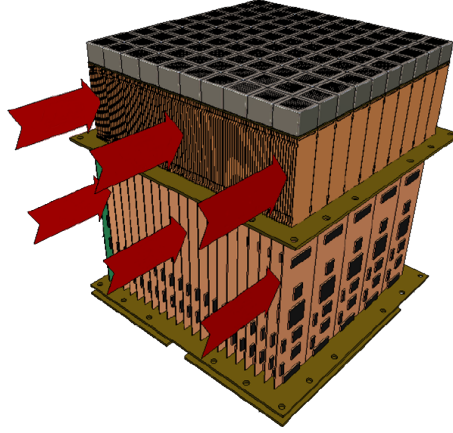
Figure 6.2: Artist view of the GAW Focal surface

The UVIScope is built as a modular system, the elementary unit being a Macro-cell. The Macrocell, represented in figure 6.3, is composed by four MAPMT, four FEBrick units, four ProDAcq and HV, LV and control boards. At the bottom of each Macrocell we can find a Trigger board. Each Macrocell unit can operate independently. A simplified scheme of a Macrocell unit is shown in figure 6.3. When inserted in the UVIScope the Trigger boards communicate with the adjacent ones and the control boards communicate with an external control board. The configuration, monitoring and read-out of the system will be performed through the external control board. The Macrocells will be mounted in a mechanical structure coupled to the Telescope body. In figure 6.4 it is represented the focal surface in its mechanical structure for the phase I (a) and phase II (b) of the project.

In the Phase I, a reduced focal surface, composed by 8×8 MAPMTs, will be used, covering a FOV of $6° \times 6°$. During this phase it is foreseen that the focal surface will be moved to different positions in order to test the performance of the telescope at off-axis angles up to $12°$.

In the Phase II the whole focal surface will be covered by 1600 PMTs, arranged in a grid of 40×40, providing a field of view of $24° \times 24°$. In order to minimise the effect of the optical aberrations the Macrocells height will be adjusted so that the MAPMT array will follow, as close as possible, the curvature of the ideal focal surface, as can be seen in figure 6.4(b).

MAPMT

The MAPMT used for GAW Focal Surface Detector is the Hamamatsu mod. R7600-03-M64 with 64 anodes arranged in an 8×8 matrix. The physical dimension of the
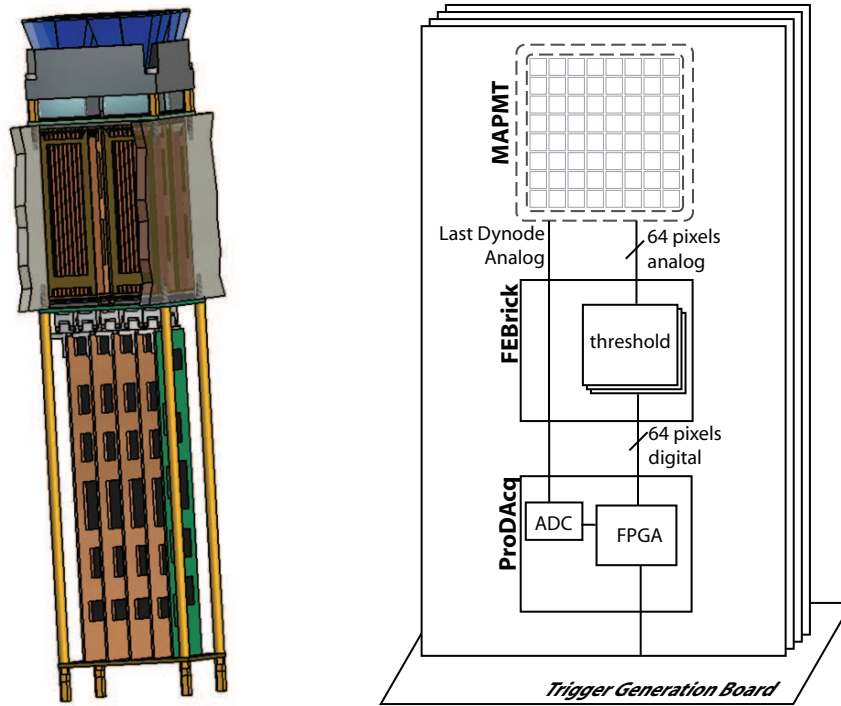
Figure 6.3: GAW Macrocell. Left: Artist view. Right: Simplified scheme

(a) Phase I

(b) Phase II
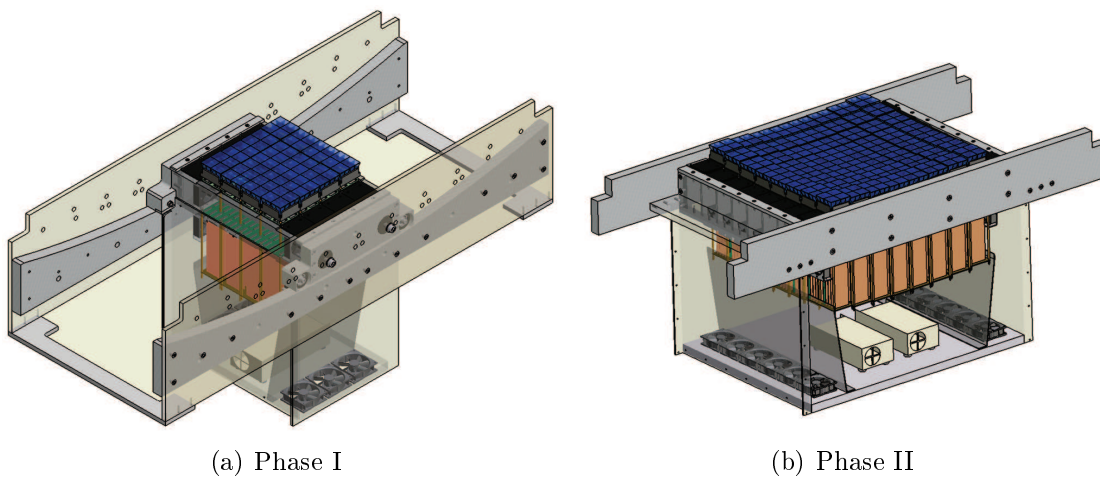
Figure 6.4: GAW Focal Surface

(a) with socket visible   (b) with PMT installed
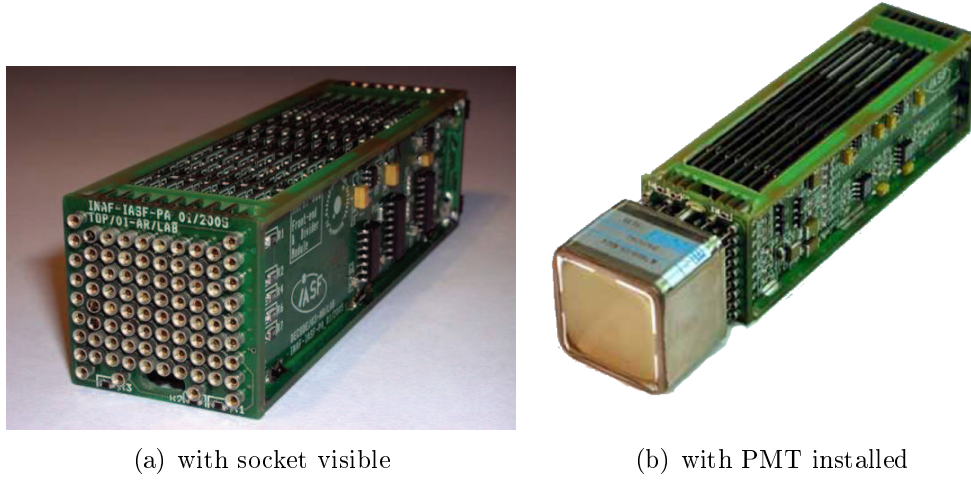
Figure 6.5: Photographs of a FEBrick unit.

tube section is $25.7 \times 25.7 \, \mathrm{mm}^2$ (minimum true area is $18.1 \times 18.1 \, \mathrm{mm}^2$), with length of approximately 33 mm and weight of 30 g. Each pixel has a size of 2×2 mm separated by a pitch of 0.3 mm. The crosstalk between pixels is $2\,\%$ and the anode dark current is $0.2 \, \mathrm{nA}$. The Phototube has a transit time of 10.9 ns with a spread of 0.3 ns. The output signal has a rise time of 1 ns. The tube is equipped with a bialkali photocathode and a 0.8 mm thick UV-transmitting window, ensuring good quantum efficiency for wavelengths longer than 300 nm, with a peak of 20% at 420 nm. The device has a Metal Channel Dynode structure with 12 stages, providing a gain of the order of $3 \cdot 10^5$ for a 0.8 kV applied voltage.

FEBrick

The front-end electronics of GAW is realised in a modular way. The blocks that compose the Front-End are called the Front-End Brick - FEBrick (Figure 6.5). The FEBrick is designed for a single MAPMT, implementing the front-end electronics for 64 anodic channels, working in single photon counting mode, and the last dynode signal that will be acquired as a high speed integration channel. The FEBrick also provides the HV power supply to the MAPMT and monitors the temperature.

The FEBrick develops on axis along the bottom of the MAPMT as an appendix of identical section ($25.7 \times 25.7 \, \mathrm{mm}^2$) with a length of $\sim 85 \mathrm{mm}$, that allows placing units side by side. Each FEBrick unit is connected, through a socket visible in figure 6.5(a), to the bottom of the MAPMT. In this way, the MAPMT is placed in a close contact with the input of the amplification channels in order to preserve the anodic signals.
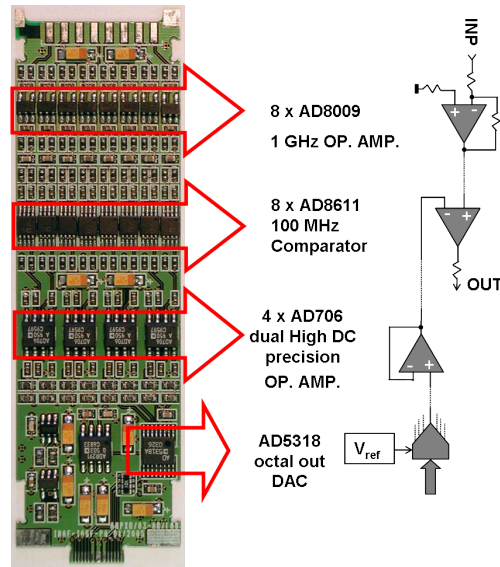
Figure 6.6: A module of the FEBrick showing the front-end scheme for an anodic channel.

A FEBrick is composed of 8 parallel boards, each implementing the electronics for a line of 8 pixels of the MAPMT. Figure 6.6 represents one of these boards and the chain of the front-end electronics for each anodic channel. Each channel is composed by a fast amplifier and a 7 ns accuracy discriminator channel for Single Photon Detection. The amplification channel is equipped with an amplifier of 1 GHz bandwidth, at unitary gain, and 5500 V/μs slew rate. The amplifier gain is set to $G = 10$ (obtaining a 320 MHz bandwidth) to increase sensitivity and detect very small signals. The discrimination is performed using a comparator with 100 MHz input frequency and 4ns propagation delay. The reference voltage of the comparator, that acts like the discrimination level, is generated by a 12 bit DAC and ranges from 0 to +250 mV in $\sim 60\,\mu$V steps. The discrimination level for each channel is set individually to make it possible to equalise input offset voltage differences between the discriminators and gain differences between the 64 anodes.

On the lateral sides of the FEBrick there are two boards in which the High Voltage Power Supply, the last dynode Front-End electronics and the Front-End management are implemented.

The Front-End electronics for the dynodic channel, operating as charge integrator, is equipped with a FET amplifier of 145 MHz bandwidth at unitary gain, 180 V/μs slew rate and 2 pA input bias current.

The FEBrick provides also the HV power supply to the MAPMT through a low power active high voltage divider. Two separate high voltage lines are provided:
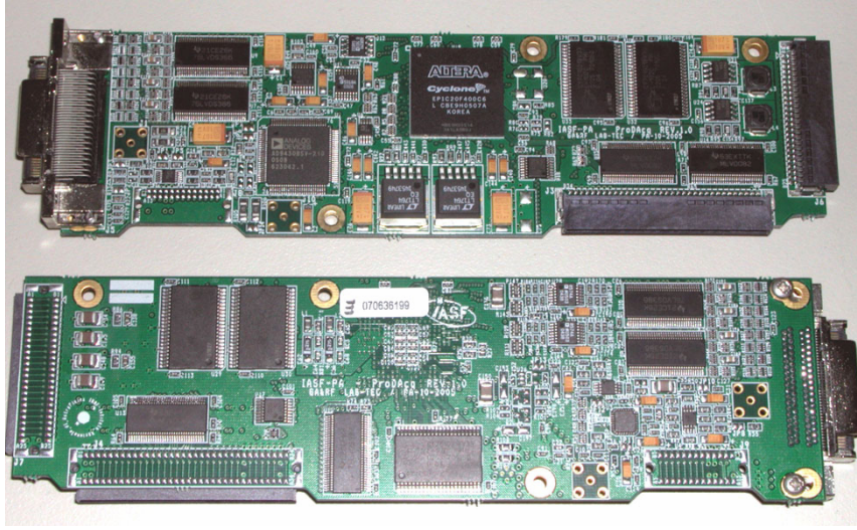
Figure 6.7: The ProDAcq Board

the first line supplies directly the last dynode and the second one supply the other dynodes through a low power active divider.

A temperature sensor detects FEBrick unit average temperature and outputs a direct digital value to provide thermal conditioning management. The temperature sensor can operate in the range of -35 to $+85°$C with an accuracy of $\pm 1°$C.

The FEBrick power consumption is about 10 W. A side-by-side assembling of many FEBrick units should need adequate thermal conditioning.

All FEBrick units, required for the whole focal surface, are placed together on the top of a backplane while on the bottom are placed the ProDAcq units. Backplane is in charge to connect FEBrick unit signals to the relevant ProDAcq units.

ProDAcq

The ProDAcq (figure 6.7) unit is internally managed by a reprogrammable FPGA. Figure 6.8 shows a simplified scheme of the ProDAcq, its operation and relation with the other components of the system. The ProDAcq samples the digital information from the 64 anodic channels with a frequency of 100 MHz and calculates the number of pixel-on. This information is then passed-on to the associated Trigger Generation board. Upon receiving a Trigger Strobe from the Trigger Generation board, the ProDAcq saves the event information in a memory. Digital signals are recorded inside three memory banks for 192 Kword storage capacities.

The ProDAcq is also responsible for the digitisation of the last dynode analog signal through two ADCs that sample the signal, one with a sampling frequency of 80 MHz and a resolution of 14 bits, the other with a higher acquisition rate of
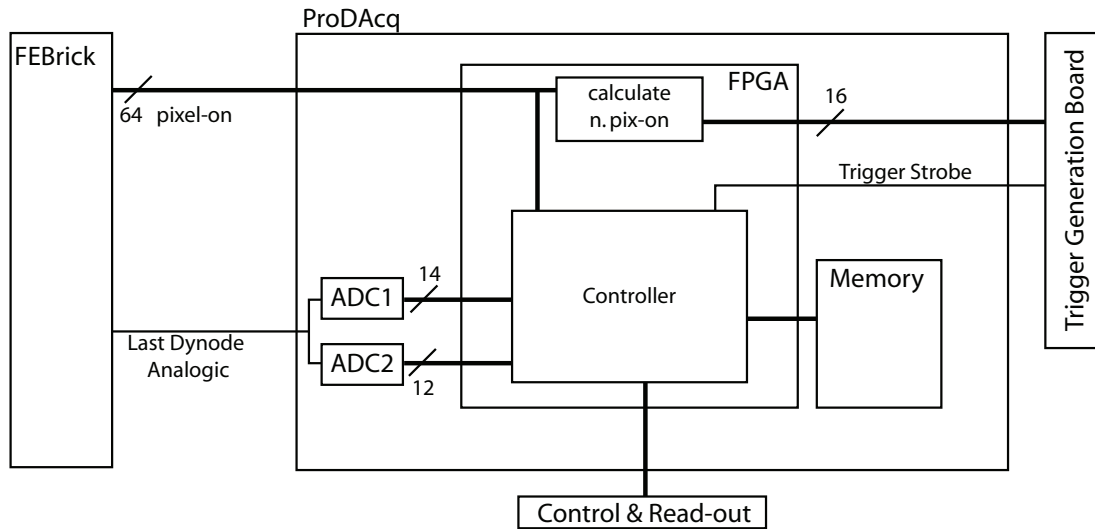
Figure 6.8: Simplified scheme of the ProDAcq board, its operation and relation with
the other components of the system.

210MSPS but a lower resolution of 12bits. In this way, the input analogue signal may
be sampled at high speed or with high accuracy, according to the wiring combination
of two ADC converters.

The ProDAcq units also sample an internal temperature sensor, signal alarm
conditions and allow access to the event memory for the read-out of triggered events.
The ProDAcq will also register the sky image seen by the PMT pixels, which is
recorded as the number of counts in each second for each pixel.

ProDAcq units are inserted on the bottom of the backplane through which the
signals of the relevant FEBrick units are received and are terminated on a Trig-
ger Generation Board equipped with Trigger and Timing Synchronisation devices,
instrumentation management, power supply and external host interface.

Trigger Generation Board

The trigger generation board is responsible for the generation of local trigger signals.
The DAQ system of GAW has an array of these boards, each connected directly to
four (2×2) ProDAcq boards and to their neighbours. Trigger generation boards are
composed, basically, by an FPGA that receives the number of active pixels from four
ProDAcqs, receives and sends data to their neighbours and evaluates if the trigger
conditions are met for the set of information available. If the condition is met the
board will issue a trigger signal that, when validated, will cause the ProDAcq boards
to save the event information for later retrieval.

6.2.3 Trigger system concept

The main requirement of the GAW trigger system is to be able to have a good efficiency at the lowest possible energy, keeping a high rejection power of the background, dominated by the Night Sky Background (NSB).

The Cherenkov signal will produce an image in the camera that adds up to the background. Since the focal surface is highly pixelated this excess light is translated directly into an excess of the number of activated pixels. The GAW triggering system relies on the detection of an increase in the number of activated pixels in a region of the focal surface. More specifically the system is a majority trigger that will search for, at least, a defined number of activated pixels in a square of $k \times k$ pixels.

The noise counting rate, n, of each telescope can be calculated knowing the average value of the background and applying the optical and geometrical characteristic quantities of the telescope. For an individual pixel n is then calculated as

$$n = \langle B \rangle \cdot A \cdot \Omega_{pix} \cdot \Delta t \cdot \varepsilon_{total}$$

where $\langle B \rangle$ is the average value of the Night Sky Background, A is the collecting area of the telescope, Ω_{pix} is the solid angle subtended by one pixel, Δt is the time interval of a Gate Time Unit (GTU) and ε_{total}, the global efficiency of the telescope. The option for a highly pixelized focal surface running at a high acquisition rate (100 MHz) makes the pixel solid angle and the Gate Time Unit (GTU) small, thus minimising the noise in each pixel.

The average value of the Night Sky Background was measured [46] at the Calar Alto Observatory and its rate is estimated by

$$\langle B \rangle = 2200 \, \text{photons} \cdot \text{m}^{-2}\text{ns}^{-1}\text{sr}^{-1}$$

For GAW $A = 3.5 \, \text{m}^2$, $\Omega_{pix} = 2.3 \times 10^{-6}$ sr, $\Delta t = 10$ ns and $\varepsilon_{total} = 0.06$[46]. With these parameters the mean noise counting rate, per pixel, is estimated to be $n \sim 0.01$ photoelectrons/pixel/GTU. The number of photoelectrons in each pixel and in each GTU then fluctuates according to a Poissonian distribution with a mean value of 0.01.

The Cherenkov signal is an intense and fast light pulse which produces an increase, during a short time (< 10 ns), in the number of pixels with signal in a small region of the focal surface ($0.5° \times 1°$). The concept of the GAW trigger system is to search, online, the whole focal surface for an increase in the number of pixels-on in predefined regions large enough for the signal to be contained inside.

6.2.4 Trigger system design

The GAW trigger system is designed to work in three levels. The first trigger level defines a pixel-on. The second trigger level searches the focal surface for an increase of pixels with signal. The third trigger level validates the second level triggers and signals the region of interest of the focal surface to be read. Each level is implemented in different parts of the GAW DAQ electronics described previously.

First Trigger Level

At the first trigger level the signals from the PMT pixels are subjected to a simple threshold and are transformed into digital signals. A pixel-on is defined here as a pixel which has a signal greater than the set threshold.

The first trigger level is implemented on the front-end electronics (FEBrick), namely as a fast discriminator. The specific detail of the electronics of this trigger is described in 6.2.2.

The thresholds are set independently for each front-end channel, taking into account differences in gain and amplification. The threshold is set below the single electron response of the pixel and above the electronics noise of the amplification chain, initially in the laboratory and are afterwards adjusted on site by means of a calibration run of the telescope.

After this first trigger level, the signal recorded in each of the 64 pixels of one PMT is transformed into 64 logic signals indicating the pixels that have signal. This information is passed directly to the second trigger level.

Second Trigger Level

The second trigger level, the core of the trigger system, searches for an excess in the number of pixels-on. This trigger level scans the digital information received from the first trigger level and searches the focal surface, online, for a given number of pixel-on inside all possible trigger-cells (squares of 2×2 PMTs). The second level trigger is digital and as such can be implemented in FPGAs. Due to its complexity and high number of channels involved, it is implemented in the ProDAcq boards and in the Trigger Generation boards.

The FPGA in the ProDAcq board receives digital information about the individual state of the 64 anode channels of the associated MAPMT and calculates the total number of pixel-on which is then passed to the Trigger Generation board to which the ProDAcq is connected to.

Each Trigger Generation board receives the number of Pixel-on from four Pro-DAcqs and is connected to their neighbour trigger generator board so that information essential for the generation of a local Second Level Trigger can be shared.

The trigger algorithm, implemented in the FPGAs of the Trigger Generation boards, works online in a pipeline with three steps. On the first step, each FPGA receives the number of Pixel-on from the four ProDAcq attached to it. On the second step it transmits information about relevant PMTs to its neighbour FPGAs on the right and on the bottom, receiving data from the top and left neighbours. This communication scheme allows for each FPGA to have access to the number of pixel-on for a set of 3×3 PMTS. On the third step each FPGA will search for a number of pixel-on greater than a programmable value in all possible trigger-cells with the information available to that FPGA. If this condition is met a second level trigger is generated and passed to the third trigger level. With this scheme implemented the whole focal surface can be searched for the trigger-cells that meet the trigger condition.

The timing for the triggering system is critical. Since the chain of operations must always take the same predetermined time so that the pipeline can work and the triggering data can be recovered from memory and saved.

Figure 6.9 represents this trigger scheme with an example of a focal surface of 6×6 MAPMTs. This corresponds to having a grid of 3×3 Trigger Generation Boards. The first step of the pipeline is represented in figure 6.9(a). In the right bottom corner is indicated the representation of a MAPMT and of a Trigger Generation board FPGA. In each FPGA $S_{i,k}$ represents the sum of pixels-on of the (i, k) MAPMT, i.e., the sum of the total number of pixels-on of the MAPMT located at the row i and column k. It is seen that each FPGA receives these values from the four MAPMT underlying it. For instance, the central FPGA receives, from the Pro-DAcqs, the values $S_{3,3}$, $S_{3,4}$, $S_{4,3}$ and $S_{4,4}$. In a second step the FPGAs communicate with their neighbours. Taking again the central FPGA, it receives from the top-left neighbour the value $S_{2,2}$, from the top neighbour the values $S_{2,3}$ and $S_{2,4}$ and from the left one the values $S_{3,2}$ and $S_{4,2}$. At the same time, this FPGA passes to their right, bottom and bottom-right the values $S_{3,4}$, $S_{4,3}$ and $S_{4,4}$. This process is represented in figure 6.9(b). In the end of this process the FPGA has information from a grid of 3×3 MAPMTS. In the third step of this trigger algorithm, also represented in the figure, the FPGA evaluates the total number of pixel-on for the four possible groups of 2×2 MAPMTs denoted by:

$$S_A = S_{3,3} + S_{3,4} + S_{4,3} + S_{4,4}$$
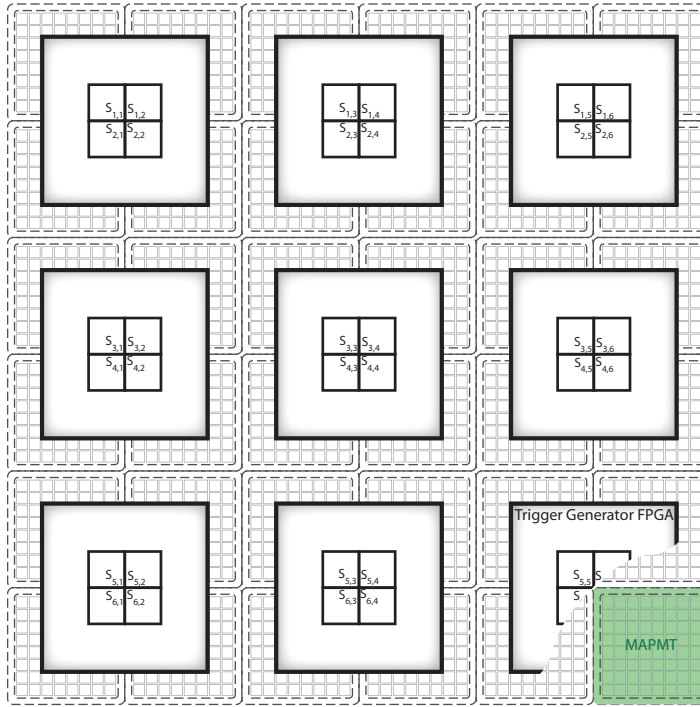
(a) first step of the pipeline
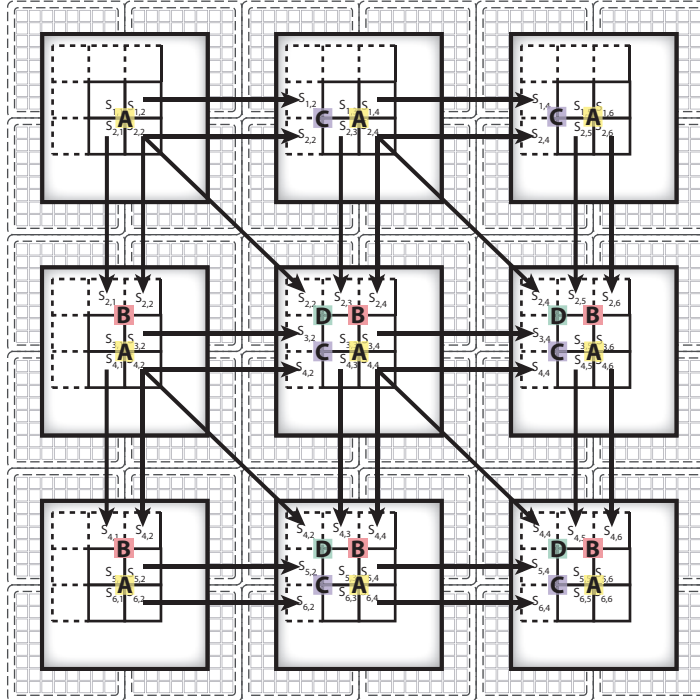
(b) second and third step of the pipeline

Figure 6.9: The second level trigger scheme.

$$S_B = S_{2,3} + S_{2,4} + S_{3,3} + S_{3,4}$$

$$S_C = S_{3,2} + S_{3,3} + S_{4,2} + S_{4,3}$$

$$S_D = S_{2,2} + S_{2,3} + S_{3,2} + S_{3,3}$$

If any of S_A, S_B, S_C or S_D is higher than the predefined threshold this FPGA issues a second level trigger signal.

The scheme exemplified is easily extended, for the whole focal surface, bearing in mind that the FPGAs in the edges do not communicate with some neighbours.

Third Trigger Level

In the third trigger level, the highest level in the GAW triggering system, the second level triggers are validated and a region of interest of the focal surface is defined to be read by the Data Acquisition system.

The third trigger level will be implemented on a FPGA that receives data from the second level trigger, i.e. from all the Trigger Generation Boards. Several modes can be implemented in this trigger level since the FPGA can be reprogrammed at any time.

In the basic mode a second level trigger in a GTU causes the whole focal surface to be read-out.

In order to reduce the bandwidth used, the third trigger level will have a mode that defines a Region Of Interest (ROI) to be read. The simplest algorithm is to define the ROI as the trigger-cells that produced a trigger and its neighbours. The number of neighbour trigger-cells to be read will be chosen to ensure that all the information belonging to an event is read. More sophisticated algorithms, including the rejection of specific noise patterns, may be implemented at this level.

In the final GAW configuration with three telescopes, a global event tag may be required. For this purpose it is foreseen that one of the telescopes can act as a central unit, receiving the third level trigger information from the other two telescopes. A temporal coincidence between the telescope triggers will be then performed and a global stamp will be issued and distributed.
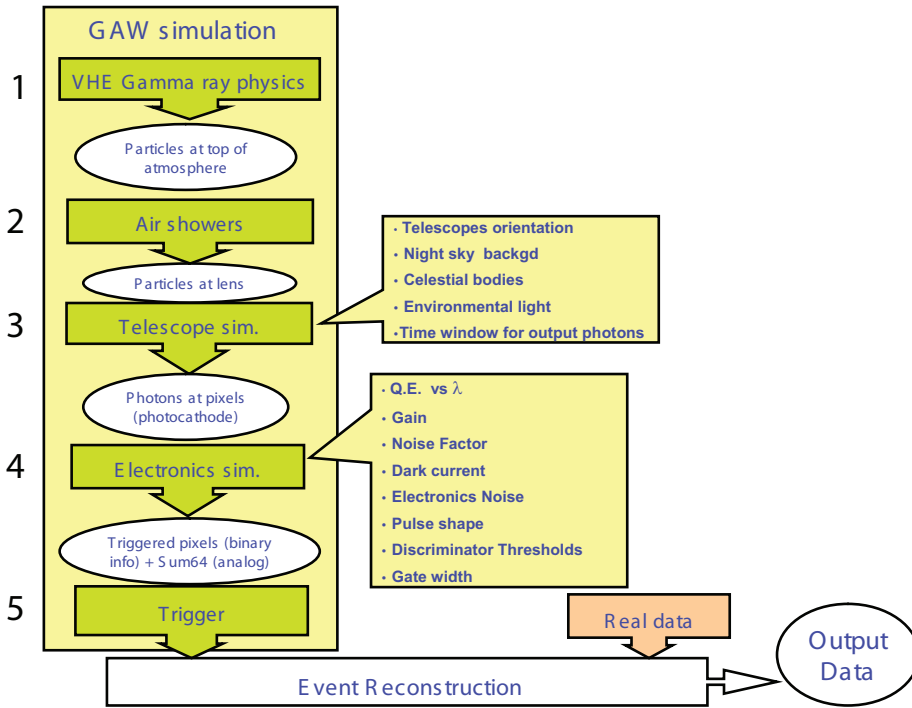
Figure 6.10: The GAW simulation Framework

6.2.5   Trigger expected performance

The triggering system performance is characterised by the capability to reject background events and by the efficiency for the selection of real events. To evaluate the trigger performance Monte Carlo simulations were developed at Palermo and at Lisboa.

At Palermo an IDL based simulation of the telescopes was used mainly to define the baseline design of the GAW telescopes. Background events were generated directly in IDL while gamma shower events were generated using CORSIKA [15] and the electronics and trigger were simulated afterwards in IDL. The specific details of such simulation are reported in [34]. A more exhaustive study on GAW performance [47] was made using CORSIKA and a custom program developed in Fortran that parametrises the lens response and simulates the Focal Surface and electronics.

At Lisboa, a global simulation framework for the GAW project was developed[48]. This framework defines the flow and the interfaces of the various programs and modules used to perform an end-to-end simulation of GAW. Figure 6.10 shows the structure of this framework. To assess the trigger performance the electronics and trigger simulation modules were implemented in the general framework using C++ and the ROOT toolkit. These modules allowed detailed cross-checks to be performed and provided an important tool for the study and development of trigger algorithms

and its implementation in the firmware.

Electronics simulation module

The electronics simulation module is a basic simulation of GAW electronics, including the noise generation due to the Night Sky Background and the simulation of the first trigger level. The focal surface, in this module, is composed of 80×80 pixels, corresponding to the focal surface of the first phase of the GAW project. The interface with GAW framework is performed through the file "Photons at pixels" generated by the Telescope Simulator which contains the information of each photon arriving at MAPMT the pixels. This information is read by the module and then a two-dimensional histogram is produced. Each bin of this histogram represents a pixel. Each photon is assigned to a bin, taking into account the PMT efficiency. A random number is uniformly generated between 0 and 1 and the photon is accepted if the value is lower than the efficiency factor. Thus each bin hold the number of collected photons. In this module the Night Sky Background (NSB) is introduced by generating for each pixel, and for each event, a random number following a Poisson distribution. The mean value of this distribution, $\langle B \rangle$, represents the average number of photo-electrons collected in that pixel due to the NSB and is chosen by the user, having a default value of 0.008 p.e./pixel/GTU.

For the purpose of this simulation it was assumed that the photomultiplier and the electronics do not introduce noise above the threshold of the first trigger level and that the first trigger level would operate with full efficiency for the detection of single photo-electrons. Thus if the number of photo-electrons in a pixel is greater than or equal to one the pixel is considered as a pixel-on. The output of this module consists of a pixel-on image of the focal surface.

A more detailed implementation of the first trigger level can be performed assigning a probability for the detection of the single photo-electron. Electronics noise, above the first trigger level threshold, can also be introduced at this level using the outlined scheme. It is planned to implement a more detailed description of the signal processing chain to be included in the general framework.

Second trigger level simulation module

The trigger module implements the simulation of the second level trigger. As described in section 6.2.2, this trigger level looks for an excess of pixels-on in trigger cells. These trigger cells are coded in the module, defining the pixels that constitute the cell. For each pixel-on image, a loop is performed in the trigger cells and, for
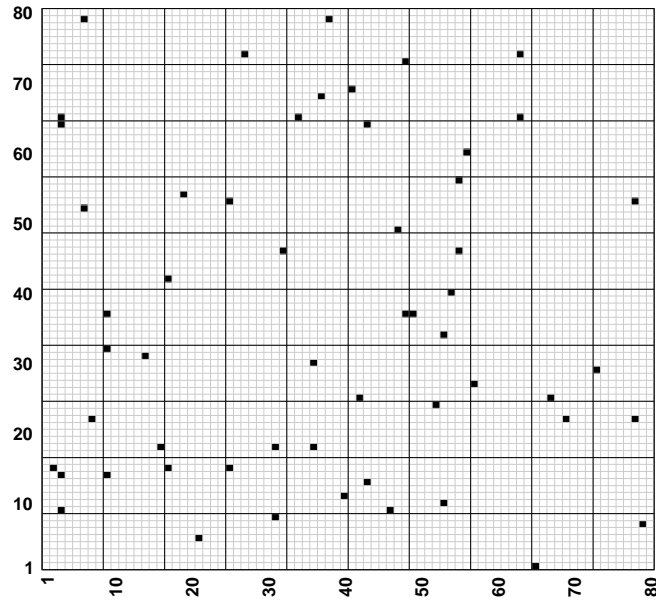
Figure 6.11: Image of GAW focal surface for a noise event. Each black square represents a pixel-on. The event was generated with a background level of $\langle B \rangle = 0.008 \, \text{pe/pixel/GTU}$

each one, the total number of pixels-on is calculated. The module outputs the maximum number of pixels-on in a trigger cell. A simple comparison with the second trigger level threshold can be performed afterwords to get a decision on the trigger of the simulated event.

Using the framework, and the developed modules, the rejection power of background and the efficiency for gamma events were studied and will be discussed in the following paragraphs.

Fake trigger rate estimation

Noise events were generated by simulating the pixel-on image formed in the Focal Surface due to the Night Sky Background. Figure 6.11 shows an image of the Focal Surface produced by a typical noise event produces for a background level of $\langle B \rangle = 0.008 \, \text{pe/pixel/GTU}$. In the image, the pixels-on are represented by black squares. Each event corresponds to the information present in the focal surface at each GTU of 10 ns. The output of the trigger simulator was used to increment a vector of the number of triggered events for several second trigger level thresholds. This vector holds thus the number of triggered events for the second trigger level
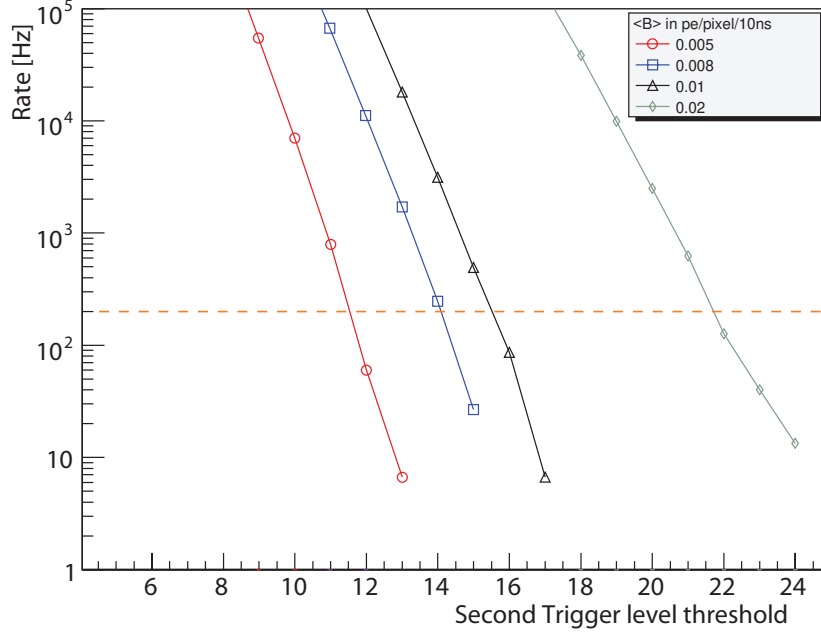
Figure 6.12: Fake trigger rate of a GAW telescope versus the second trigger level threshold. The different lines represent the fake trigger rate for several levels of background, $\langle B \rangle$ as indicated in the legend.

for each threshold level. The fake trigger rate at this level, η, is calculated as

$$\eta = \frac{\text{N. Triggered events}}{\text{N. generated events}} \cdot \frac{1}{\Delta t_{\text{GTU}}}$$

where Δt_{GTU} is the sampling period of the system.

The errors of the fake trigger rate, ε_η, were computed according to [49] as

$$\varepsilon_\eta = \sqrt{\frac{(k+1)(k+2)}{(n+2)(n+3)} - \frac{(k+1)^2}{(n+2)^2}} \cdot \frac{1}{\Delta t_{\text{GTU}}}$$

where k is the number of events that meet the trigger condition and n is the number of generated events.

The fake trigger rate as a function of the second trigger level threshold is shown in figure 6.12, for several levels of the background. The number of generated background events was 15×10^6. A reference value of 200 Hz of the fake trigger rate is indicated by an horizontal orange dashed line. This value is obtained in the GAW proposal [46] in the conditions of a background of $\langle B \rangle = 0.008$ pe/pixel/GTU and a second trigger level threshold of 14.
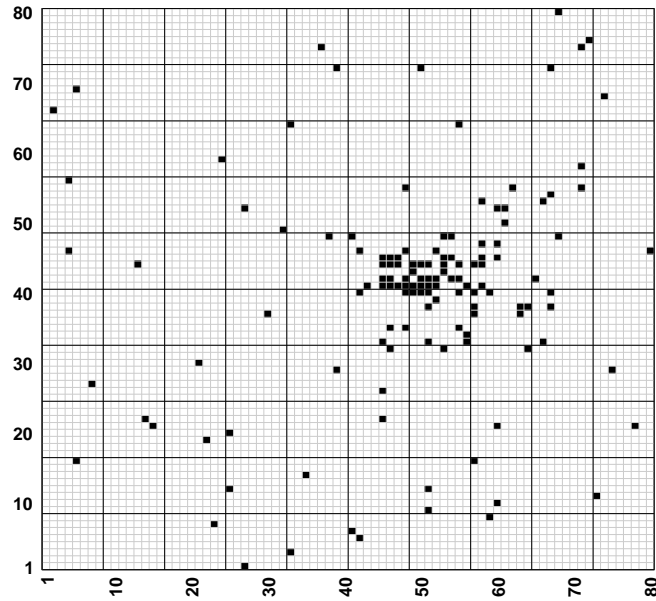
Figure 6.13: Image of a 1 TeV gamma event at the GAW Focal Surface

If the background level increases, e.g. in the presence of the moon in the sky, the fake trigger rate can be easily reduced by redefining the trigger threshold. From the figure it is seen that setting the second trigger level threshold at 22 a fake trigger rate lower than 200 Hz can be obtained even with a background as high as twice the typical one. Such background level can be found when a quarter moon is present in the sky at low zenith angles. However if the background increases too much the MAPMT looses its linearity and can even be damaged. An electronic protection is included in the front-end electronics to prevent damage to the PMT for very intense light levels.

Trigger efficiency estimation

The simulation framework was also used to study the trigger efficiency for different second trigger level thresholds. The CORSIKA program [15] version 6.617 was used to simulate gamma air showers, followed by the Telescope Simulator, developed in Geant4 [30, 31], the Electronics simulator and trigger simulator described before.

For this study, vertical gamma events were generated with the core of the air shower located at 100 m from the telescope, at fixed energies of 200, 300, 500, 700, 1000, 2000 and 3000 GeV. For each energy 100 events were generated. As an example, figure 6.13 shows a snapshot of the focal surface with a 1 TeV gamma
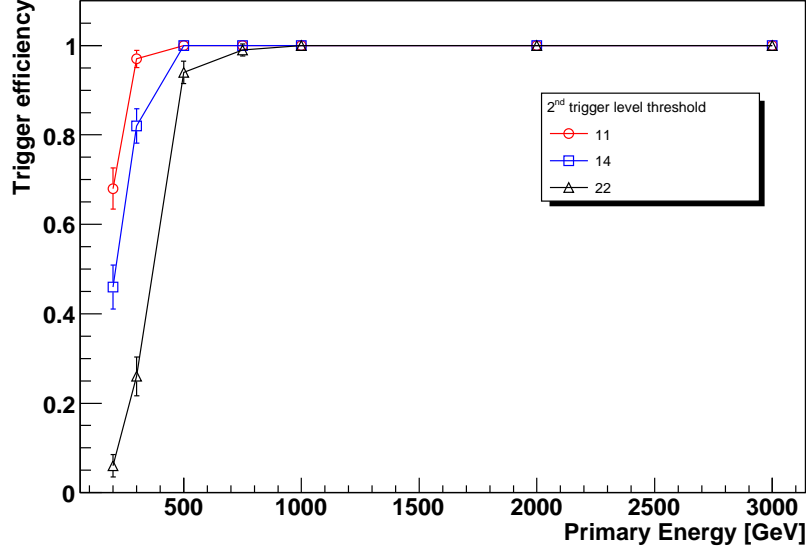
Figure 6.14: Trigger efficiency versus the shower primary energy for different trigger thresholds.

event, with each pixel-on indicated by a black square. For each event, the output of the trigger simulator was compared to three different thresholds of 11, 14 and 22. An efficiency was then calculated for each energy and each threshold as

$$\text{eff} = \frac{\text{N}^{\underline{\text{o}}} \text{ triggered events}}{\text{N}^{\underline{\text{o}}} \text{ generated events}}$$

with an error given by

$$\varepsilon_{\text{eff}} = \sqrt{\frac{(k+1)(k+2)}{(n+2)(n+3)} - \frac{(k+1)^2}{(n+2)^2}}$$

where k is the number of events that meet the trigger condition and n is the number of generated events. Figure 6.14 shows the obtained trigger efficiency as a function of the primary energy for each threshold. At low energies, the trigger efficiency is reduced with the increase on the trigger threshold, while energies above ~ 1 TeV have a very high trigger efficiency regardless of the threshold set.

The light signal reaching the telescope varies with the distance to the shower core. Thus the maximum distance at which a shower can be detected, and hence the sensitivity of the telescope, varies with the energy and the trigger efficiency. An increase in the trigger threshold will reduce the sensitivity of the telescope. However the telescope can work with higher background levels, with acceptable sensitivity

for high energetic showers, thus increasing the total exposure.

The estimation of the effective area with the energy and trigger threshold will require a large sample of showers at different energies and distances

6.2.6 System firmware

The system firmware for a great part of the acquisition electronics is a responsibility of the LIP group. Namely, LIP is responsible for the development of the firmware for ProDAcq boards and for the Trigger Generation boards.

A test bench to test the ProDAcq is installed in the e-CRLab that consists on a ProDAcq board, two interface boards and test and measuring equipment. An interface board, named ProDAcq-Excite, allows the ProDAcq signal inputs to be coupled to a signal generator or to an external FPGA. These external sources allow the output from a FEBrick unit to be emulated. The signal generators available allow four independent input signals to be produced. When coupled to a FPGA development kit it is possible to generate all the 64 input signals of the ProDAcq, allowing all possible configuration of the input signals to be tested. However, the output of the FPGA is digital and the shape and timing of the signals cannot be controlled as well as with the signal generators. Another interface board, named LIP-CTRIG, is used for power supply, programming interface and to connect the trigger and control bus to external equipment. The trigger information can be seen in a logic analyser or it can be coupled to a FPGA development kit which is also used to input data in the control and trigger bus. Although the use of an FPGA to interface the board adds extra flexibility, the performance tests need to be performed using the logic analyser to assure correct time measurements. In particular the logic analyser available is capable of performing timing measurement with sub-nanosecond accuracy.

Several firmware modules for the ProDAcq have already been developed, mainly for functional tests of the board. The ProDAcq board can operate in two distinct modes. The firmware takes that into account and the user can choose at run time the acquisition mode. Additionally every parameter that the firmware uses will also be programmable by the user.

In the first mode, used mainly for testing, the ProDAcq counts how many times each pixel has been activated. This count is performed with a sampling period that corresponds to the normal acquisition frequency for a pre-determined time interval (of the order of seconds). In this way the light flux at each pixel can be evaluated. This mode can be used to, e. g., estimate the background level or, if the telescope

is pointed to a star, to evaluate the optical spot produced in the Focal Surface.

In the second mode, the acquisition mode, the ProDAcq receives data from the FEBrick and saves it in a ring memory. At the same time it counts the number of pixels-on and outputs this value to the trigger bus. This algorithm is part of the pipeline scheme of the trigger system and needs to be performed each sampling period. Moreover the algorithm must always take the same time so that a reference to stored data is available. When a trigger strobe is received from the Trigger Generation boards, the ProDAcq saves the corresponding data that will be read through the control bus. The board firmware also comprises the implementation of the control and read-out protocol that is yet to be defined.

The firmware of the Trigger Generation board implements the trigger algorithm described before. In each sampling period, the board receives the number of pixels-on from four ProDAcqs. In a following step the board will exchange data with its neighbours and then applies the majority trigger algorithm. When the trigger condition is met the trigger generation board issues a trigger strobe to the relevant ProDAcqs. In the baseline design the ligh-guides are composed by 64 segments, one per pixel. Its fabrication and assembling showed to be a challenge. Thus, other options were studied, namely the option of reducing the number of segments by a factor 4. This fact has delayed the development of the Trigger Generation boards as the pitch between PMTs depends on the final design of the light-guides. The trigger firmware tests will start as soon as these boards become available.

Chapter 7

Studies of the Auger Observatory Fluorescence Telescope performance

The LIP group has developed a new simulation based on Geant4 where the complete geometry of the Auger fluorescence telescope is implemented. This new tool was used to study in detail the performance of the telescopes in terms of optical quality and efficiency. The results obtained were compared with the standard simulation and with laser events.

7.1   Auger Fluorescence Telescopes

The Auger Fluorescence Detector (FD) is composed of 24 Fluorescence Telescopes. The telescopes are disposed in four eyes overlooking the Surface Detector array. Each eye has a Field Of View (FOV) of $28.6° \times 180°$. Each of the 24 Fluorescence Telescopes is a modified Schmidt camera.

The Schmidt telescope design is based on the use of a spherical mirror with an aperture stop at the centre of curvature. This design produces uniform images in a spherical focal surface, with its centre of curvature coincident with the one of the mirror. A corrector plate in the aperture is introduced to correct the spherical aberration of the telescope. A more complete description of the Schmidt camera can be found in [50].

The scheme of the telescopes and a picture of one of them is shown in figure 7.1 where the filter, the corrector ring, the mirror and the camera are visible.
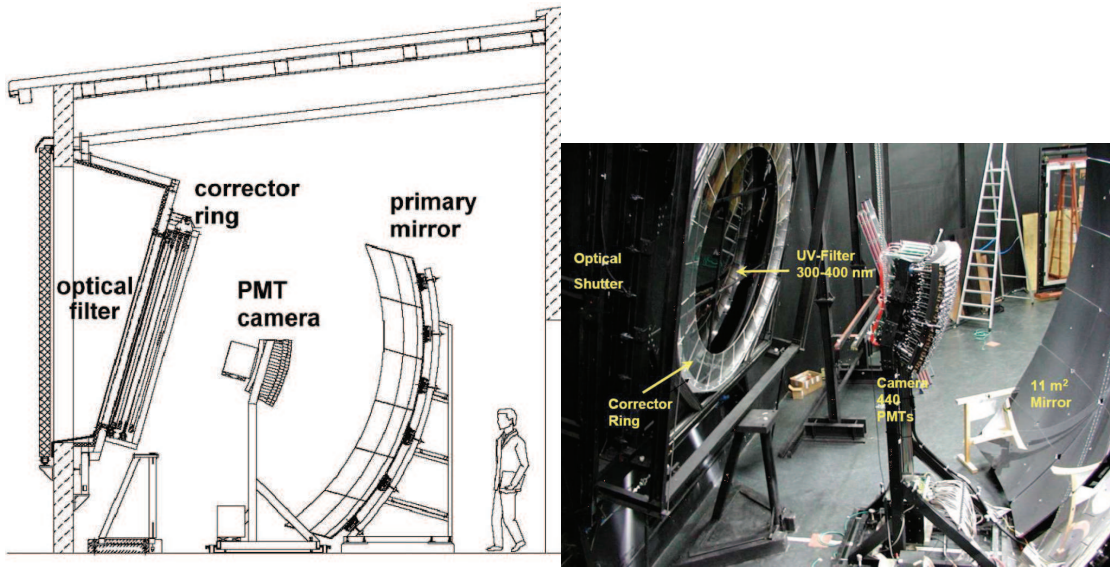
Figure 7.1: The Auger Fluorescence telescopes. Left: Scheme of the telescopes.
Right: Photograph of a telescope with its main components indicated.

Filter

The first optical component of the Auger fluorescence telescopes is an UV filter.
The filter is placed at the entrance pupil of the telescope. The main function of the
filter is to select the interesting wavelength range at the entrance of the telescope.
Besides its main function the filter also protects the telescope from exterior elements
such as wind, dust, rain, etc.

The filter is a glass plate made of Schott M-UG6 glass. It is reinforced, mechani-
cally, by a metallic grid. This filter presents a high transmittance in the UV-B region
and high absorption in the visible and infra-red regions. The detailed characteristics
of M-UG6 can be found in [51].

Corrector Ring

In telescopes with this design, a corrector plate is used to pre-correct the light rays,
that will arrive to the mirror, in order to reduce the spherical aberration introduced
by the use of a spherical mirror. The spherical aberration increases as the light rays
enter far from the optical axis. The requirements of the Auger FD of having a spot
size of 14/15 mm, that corresponds to an angular dimension of 0.5°, avoids the use
of this plate for a radius smaller than 0.85 m. Since the aperture of the telescope has
an outer radius of 1.1 m, a correction was still necessary. For simplicity a circular
ring was introduced to correct light rays that enter with a radius $0.85 < R < 1.1$ m.
This lens is called the "corrector ring".
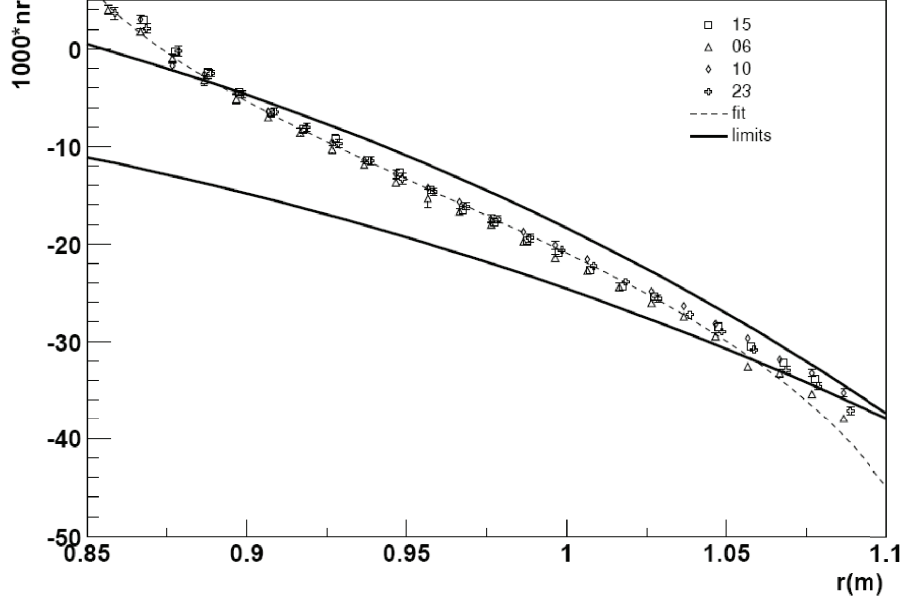
Figure 7.2: The corrector ring profile: radial component of the normal to the lens curved surface as a function of the radius. Solid lines represent the bounds used for quality control. The different markers represents the measurements performed in different samples.

The corrector ring is basically a lens with one flat side. A sixth order polynomial is used to describe the curved surface of the corrector ring. This design allows the spherical aberration to be corrected and the production of a spot within the requirements for the Auger FD. However such curvature is difficult to realise with the necessary optical quality. The profile of the lens has been optimised taking into account the production process and the fact that only a ring is used in the telescope. More details on the production of the corrector ring can be found in [52, 53]. The production process could not perfectly assure the form of the lens profile. However, the limits for the radial inclination of the surface were defined and used for quality control. Figure 7.2 shows the bounds for the radial component of the normal to the surface as well as measured profiles for different samples. It can be seen that the measured profile respects the bounds, except in the limit regions, i.e in the outer part of the ring where it goes above the bound and in the inner part where it goes below the bound. The corrector ring profile will be discussed in detail below in this chapter.

Mirror

The modified Schmidt camera of the Auger fluorescence telescope uses a spherical mirror. This mirror has a radius of curvature of $R = 3.4\,\mathrm{m}$. It has a square format and measures $3.6\,\mathrm{m} \times 3.6\,\mathrm{m}$ having a collection area of about $13\,\mathrm{m^2}$. Due to the large area the mirrors were built as an array of segments. Two eyes are equipped with mirrors built in Germany, which are made up by an array of rectangular mirrors. The other two eyes have installed mirrors from the Czech Republic which are made of an array of hexagonal-shaped mirrors.

Camera

The focal surface of the fluorescence telescopes is defined as a spherical surface concentric with the mirror surface. The focal surface has a radius of $1.743\,\mathrm{m}$, corresponding to the surface where the disc of least confusion is located for the different incident angles.

The fluorescence light from an EAS is focused onto the focal surface where a PMT camera [54] is installed. The camera, which can be seen in figure 7.1, is composed by 440 hexagonal pixels distributed in an array with 22 rows and 20 columns. The pixel has a side-to-side distance of $45.6\,\mathrm{mm}$ that corresponds to an angular distance of $1.5°$. The pixels are spaced in equal steps of azimuthal angle and equal steps of elevation angle. The FOV of the telescope is of $30°$ in azimuth and of $28.6°$ in elevation. The smaller FOV in elevation, even with a higher number of rows than columns, is due to the stacking of the hexagonal pixels to produce a continuous focal surface

The PMTs used for the Auger fluorescence telescopes have an hexagonal shape. A gap between adjacent PMTs is needed for mechanical reasons. In addition, the PMTs are quite inefficient near the borders. To overcome these problems, light guides were introduced. The light guides define a pixel in the ideal focal surface and direct the light, that would otherwise be lost, to the active region of the PMTs, where it can be detected.

The light guide is realised with six reflecting pieces called Mercedes. A scheme of the light guide and a photograph of a detail of the camera with Mercedes stars are shown in figure 7.3. Each Mercedes is a star with three arms separated by $120°$. The cross section of each arm is an isosceles triangle with a base of $9.2\,\mathrm{mm}$ and a height of $18\,\mathrm{mm}$. The top of six Mercedes define a pixel in the ideal focal surface.

The PMTs are place behind the light guides. The PMT used is a XP3062 from Photonis. The XP3062 is an 8-stage PMT with a hexagonal window and a standard
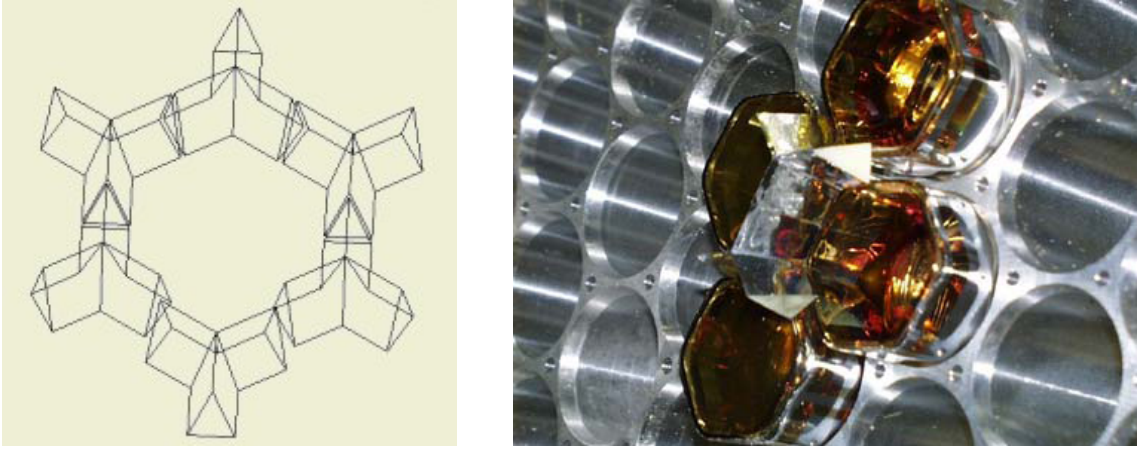
Figure 7.3: The Light Guides of the Auger Camera. Left: Scheme of six Mercedes that are joined to form a pixel light guide. Right: Photograph of a detail of the camera with four PMTs and two Mercedes stars installed.

bi-alkaline photocathode. Its quantum efficiency is evaluated as 25% for wavelengths of $250-400\,\text{nm}$. The nominal gain for FD operation is set at 5×10^4. The electronics of the fluorescence telescope samples the signal collected by the PMTs each 100 ns.

The camera body is approximately of square shape, measuring 93 cm in the horizontal dimension and 86 cm in the vertical one. The camera is held in place using a simple support of two legs. The legs of the camera are made of C-shaped steel 5 cm wide. The camera, including its body, electronics and support structure will produce an obscuration in the telescope mirror, reducing the light collection area.

7.2 Simulation of the Telescopes

7.2.1 The simulation framework

The Pierre Auger Observatory has developed a general framework for the simulation of the detector and for data reconstruction and analysis - the $\overline{\text{Off}}\,\underline{\text{line}}$ [55].

This framework was mainly developed using the C++ programming language and several toolkits and external libraries like ROOT, Geant4, BOOST, Xerces, etc. The $\overline{\text{Off}}\,\underline{\text{line}}$ is a modular software, each module performing a specific simulation or reconstruction task. XML files are used to configure the software. Each module used has an associated XML file where the module parameters are configured. The sequence of modules to be run is also configured with a XML file. Data are exchanged between the different modules through the use of a C++ class that contains the event

data.

The simulation of a fluorescence event consists of several steps required to estimate the signal recorded by each telescope when a shower develops in its FOV. First the longitudinal profile of the shower is generated. Then the amount of light arriving at the telescope pupil is estimated. To do this the production of the fluorescence light is simulated as well as the propagation and attenuation of this light in the atmosphere. Currently the fluorescence light arriving at the telescope pupil is described in the following way. The arrival times are binned with a time constant of 10 ns, which is ten times lower than the time sampling of the telescope electronics, and arrays with the number of photons and the viewed direction in each time bin are filled. Using this information, photons are then generated at random positions in the diaphragm of the telescope. For each time bin, photons are given the direction of the bin, a random position in the diaphragm and a weight. The sum of the weights of all generated photons corresponds to the total number of photons for that direction. The simulation of the telescope will then propagate these photons in the telescope and record the signal (in photons) registered in the focal surface. Noise is then added and the electronics and the trigger system are simulated. These tasks constitute the core of the simulation and are performed by different modules. Other modules execute more general tasks like the generation of the event structure and the output of the result in several formats. Several modules can be chosen alternatively to execute a specific task simply by changing the module sequence configuration file. For example the shower longitudinal profile can be generated by a module that uses a parametrisation or by a module that reads data from an external simulation program. This module, in turn, can be configured to read data from AIRES, CORSIKA or CONEX. The simulation of the fluorescence telescope can now be performed using one of two modules: the TelescopeSimulatorKG or the TelescopeSimulatorLX, the new simulation developed at Lisboa using the Geant4 toolkit.

7.2.2 The TelescopeSimulatorKG

The TelescopeSimulatorKG is a custom ray-tracing module developed by the Karlsruhe Auger Group. Currently this module is used as the standard telescope simulation module in the $\overline{\text{Off}}$ $\underline{\text{line}}$. A photon entering the diaphragm is passed, sequentially, by the several optical elements, always in the same order. This fact makes it possible to develop a simple custom ray-tracing code that simulates, in sequence, the several optical elements of the telescope.

A photon enters the telescope diaphragm with a certain direction, position and weight. This weight, w, allows one simulated photon to represent w photons that are propagated like a bunch. Such a photon is passed from the PhotonGenerator module to the TelescopeSimulator module. Then the interaction with the filter is simulated. The position and direction of the photon is maintained but its weight is multiplied by the filter transmittance. Next the corrector ring is simulated. If the position of the photon has a radius, relative to the optical axis, greater than the inner radius of the corrector ring the photon suffers two refractions in the two surfaces of the corrector ring. First the photon is refracted in the curved surface of the corrector ring. Then the position of the photon in the flat surface is calculated with the direction of the photon after the first refraction. Finally the photon suffers the second refraction in the flat surface. The weight of the photon is once again altered by taking into account the transmittance of the corrector ring. Thus, the corrector ring changes the position, direction and weight of the photon. Afterwards the position at which the photon will hit the mirror is calculated. In this step it is verified whether the photon will hit the back of the camera, and thus be killed, as well as whether the photon will pass outside the mirror area. If the photon hits the mirror, it is reflected taking into account the mirror reflectivity in the photon weight. Next the position of the photon in the camera is calculated. If the photon hits a light guide, one or more reflections are simulated until the photon hits a PMT. The reflectivity of the light guides is taken into account at each reflection. The fact that the photon can be reflected in the PMT window before hitting the photocathode of the PMT is taken into account. The quantum efficiency of the PMT is also introduced in the photon weight. When a photon hits a PMT photocathode it is added to the signal of that PMT with a weight (representing the number of detected photons) that reflects the input weight (which represents the number of photons at the diaphragm) multiplied by the efficiencies of the several optical elements of the telescope.

The simulation is performed for a normalised wavelength of $\lambda_{\mathrm{norm}} = 370\,\mathrm{nm}$. The different photon wavelengths are taken into account by introducing a relative efficiency by which the output weight is multiplied.

7.2.3 The TelescopeSimulatorLX

Overview

The TelescopeSimulatorLX is an $\overline{\mathrm{Off}}\,\underline{\mathrm{line}}$ module for the simulation of the Auger fluorescence telescopes using the Geant4 toolkit [30, 31]. This module was developed

in Lisboa with the aim of performing a cross-check with the standard simulation and of performing detailed studies of the fluorescence telescopes. Three persons from LIP (Patrícia Gonçalves, Bernardo Tomé and me) were involved in the development of this code representing a total effort of about 2 FTE (Full Time Equivalent). Patrícia and Bernardo were responsible for the implementation of the geometry and processes in the Geant4 framework while I was responsible for its integration in the $\overline{\text{Off}}\, \underline{\text{line}}$ framework and the development of the analysis tools. To allow for direct comparisons with the previous code, the TelescopeSimulatorLX was integrated inside the TelescopeSimulatorKG that had to be altered to record the properties of photons at the different locations.

Geant4 is a software toolkit developed in the C++ programming language. It simulates the passage of particles through matter. The user defines the geometry and composition of the media, as well as a primary particle and its properties, and then passes the control of the simulation to the kernel of Geant4. The kernel will then take care of the tracking and interactions of the primary and secondary particles throughout the defined "world", taking into account the properties of the traversed materials. Whenever a particle (a photon in the present application) interacts with a "sensitive detector", the relevant information is saved. The kernel will return when there are no more particles to be tracked. Besides the actual sensitive detectors existing in each detection system (the PMTs in the present case), virtual sensitive detectors can be introduced in any part of the system in order to save the particle information. This feature is used for testing purposes throughout this chapter.

The TelescopeSimulatorLX module was developed taking advantage of the capability to define arbitrarily complex geometries in Geant4 and of its ability to track optical photons and simulate the various optical processes. In the TelescopeSimulatorLX the geometry of the Auger fluorescence telescopes is implemented with their detailed optical properties. The implementation of the several components will be discussed in the following paragraphs.

For each photon generated by the PhotonGenerator module of the $\overline{\text{Off}}\, \underline{\text{line}}$ a primary optical photon, with the same characteristics (position, direction and wavelength) is defined in Geant4. At this point the Geant4 kernel takes control of the simulation of that photon in the telescope. The photon interacts with the several pieces of the telescope. In this process the characteristics of the photon are changed and the photon can even be killed. The photons are killed with a probability that reflects the several inefficiencies of the optical system. Several sensitive detectors are implemented so that detailed studies of the different components of the telescope can be performed. The properties of the photons that hit these sensitive detec-

tors are recorded in a separate ROOT file for analysis. The PMTs are simulated using sensitive detectors. When a photon hits one of these detectors the signal is added to the PMT trace, the photon is killed and Geant4 returns the control to the TelescopeSimulatorLX that will call Geant4 with the next photon.

The implementation of the telescope geometry and material definition was the key task in the development of the simulation using the Geant4 toolkit. For each optical component of the telescope a solid in space with the correct geometry must be defined, as well as the optical properties of the component material. The main challenges in this work were the detailed definition of a relatively complex geometry, and the use of Geant4 for optical applications, which is not very common.

Filter

The filter of the Auger fluorescence telescopes is implemented as a disk made of M-UG6. The disk has a diameter of 2.2 m and a thickness of 3.25 mm. The filter is positioned perpendicular to the optical axis of the telescope, 10 cm before the corrector lens geometric centre. Its centre coincides with the optical axis. The optical properties (refractive index and transmittance) are described in the simulation following the manufacturer datasheet [51] for this type of material. The refractive index is described in the simulation as 1.526, independent of the photons wavelength. The bulk absorption in the material is implemented as a tabulated function of the absorption length versus the photons wavelength. The absorption length is calculated from the transmittance that assumes a nominal value of 0.83 at a wavelength of 370 nm for a thickness of 3.25 mm.

Corrector Ring

The corrector ring is a fundamental piece of the telescope. It influences directly the quality of the optical image produced. The lens is implemented using the Geant4 class G4Polycone. This class allows the implementation of a revolution solid by defining the section of the solid and the angular limits for the revolution. The section is defined through a series of points (r, z) that are joined by straight lines. Figure 7.4 shows three visualisations of the corrector ring. In the figures the curvature of the corrector ring is exaggerated to be visible in the picture. The figure on the left shows a revolution of $3/2\pi$. The figure on the centre is a magnification of the left one. The figure on the right shows a corrector ring segment in which the profile of the curved surface was described using only four points, to make visible the discretisation of the curved surface. The corrector lens profile can be characterised by the radial
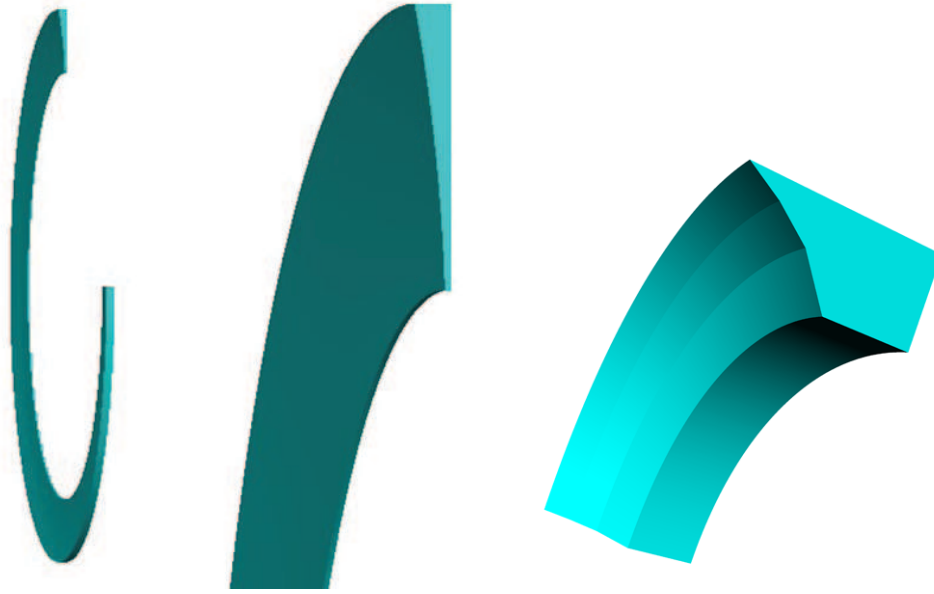
Figure 7.4: The Auger FD corrector ring.

component of the normal to the curved surface, n_r, since the other component
can be obtained from the normalisation condition. In the TelescopeSimulatorLX
four corrector lenses with different profiles are implemented. The first one called
"KG" corresponds to the profile implemented in the TelescopeSimulatorKG and to
the theoretical profile described in [53]. The radial component of the normal as a
function of the radius is described by

$$n_{r_{\text{KG}}}\left(r\right) = \frac{4}{32\left(n-1\right)f^3} \cdot r^3 - \frac{3R_d^2}{32\left(n-1\right)f^3} \cdot r^3$$

where $n = 1.5$, $f = 1.657\,\text{m}$ and $R_d = 0.85\,\text{m}$. The second one is called the "circular"
profile and corresponds to a profile cut with a circular disk of radius R displaced
from the centre by y. This profile is described by

$$n_{r_{\text{Circ}}}\left(r\right) = \frac{r-y}{\sqrt{R^2 - \left(r-y\right)^2}}$$

where $R = 8.383\,\text{m}$ and $y = 0.79527\,\text{m}$. The third and fourth corrector lens profiles
implemented in the code correspond to the upper and lower limit for n_r in the
figure 7.2. The upper and lower limit curves in the figure were fit with third order
polynomial functions,

$$n_r\left(r\right) = a_1 \cdot r + a_2 \cdot r^2 + a_3 \cdot r^3$$

yielding, for the upper limit curve, $a_1 = 5.906 \times 10^{-3}$ m^{-1}, $a_2 = 94.52 \times 10^{-3}$ m^{-2}, $a_3 = -118.8 \times 10^{-3}$ m^{-3} and $a_1 = -22.25 \times 10^{-3}$ m^{-1}, $a_2 = 85.2 \times 10^{-3}$ m^{-2}, $a_3 = -87.52 \times 10^{-3}$ m^{-3} for the lower limit profile curve. These four profiles are represented in figure 7.5(a) versus the radius of the lens. The corrector ring is implemented in Geant4 by defining its physical dimensions, in particular the height z. Figure 7.6 illustrates the geometry of the lens surface and the relation between the normal vector and the height. The height of the curved surface can be defined from $n_r(r)$ by:

$$z(r) = \int_{r_0}^{r} \frac{n_r(r')}{\sqrt{1 - n_r^2}} dr' \sim \int_{r_0}^{r} n_r(r') \, dr'$$

The four profiles then take the form:

$$z_{\text{KG}}(r) = z_0 + \frac{1}{32(n-1)f^3} \cdot r^4 - \frac{3/2 \cdot R_d^2}{32(n-1)f^3} \cdot r^2$$

$$z_{\text{Circ}}(r) = z_0 - \sqrt{R^2 - (r-y)^2}$$

$$z_{\text{Low}}(r) = z_0 + \frac{a_1}{2} \cdot r^2 + \frac{a_2}{3} \cdot r^3 + \frac{a_3}{4} \cdot r^4$$

$$z_{\text{Up}}(r) = z_0 + \frac{a_1}{2} \cdot r^2 + \frac{a_2}{3} \cdot r^3 + \frac{a_3}{4} \cdot r^4$$

or, numerically,

$$z_{\text{KG}}(r) = 0.00358557 + 0.0137377 \cdot r^4 - 0.0148882 \cdot r^2$$

$$z_{\text{Circ}}(r) = 8.38282 - \sqrt{70.2747 - (r - 0.79527)^2}$$

$$z_{\text{Low}}(r) = -0.00201816 + 0.011125 \cdot r^2 - 0.0284 \cdot r^3 + 0.02188 \cdot r^4$$

$$z_{\text{Up}}(r) = 0.00597899 - 0.002953 \cdot r^2 - 0.0315067 \cdot r^3 + 0.0297 \cdot r^4$$
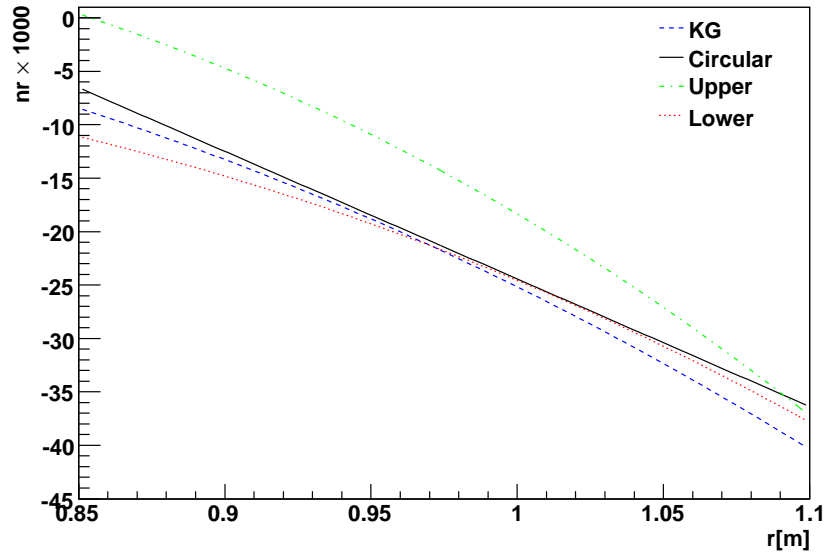
(a) Radial component of the normal to the curved surface of the corrector ring
versus (n_r) the radius of the lens.
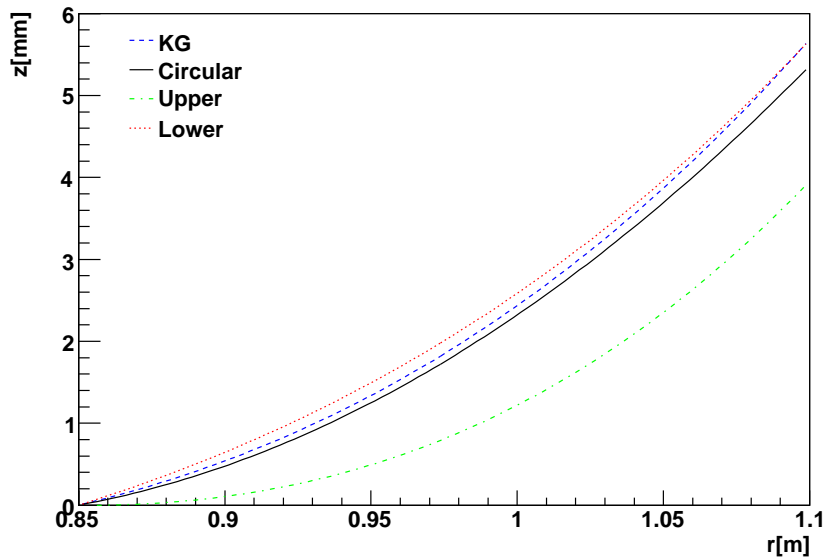
(b) Height of the curved surface of the corrector ring (z) versus the radius.

Figure 7.5: The profiles of the corrector ring
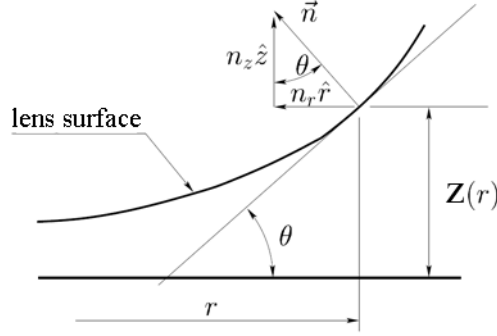
Figure 7.6: Relation between the lens height $z(r)$ and its normal vector $\vec{n}$. r is the distance to the centre and n_r and n_z are, respectively, the radial and vertical components of the normal. Figure adapted from [53].

where the integration constant z_0 is used to set all profiles to zero at the radius $r = 0.85$ m. These four profiles are represented in figure 7.5(b). In the Geant4 simulation, the lens profile is defined by taking points according to these formulae. Two extra points define the the planar surface of the lens. The points are set such that the lens has a thickness of 5 mm in the inner part of the lens. The segmentation of the corrector lens is also implemented in the simulation. The lens is segmented in 24 petals, each with an angular width of 14.735°. The corrector lenses are made of BK7 glass. The optical properties (refractive index and transmittance) of this material are implemented in the Geant4 simulation as a tabulated function of the photon wavelengths. Figure 7.7(a) describes the refractive index of the material while the transmittance for 1 cm of material is shown in figure 7.7(b).

Mirrors

In the TelescopeSimulatorLX the Auger fluorescence telescopes mirrors made of hexagonal elements are implemented in full detail. The mirrors are composed by 64 mirror elements arranged in 8 rows. These elements are quasi-hexagonal spherical mirrors, and their exact shape depends on the position they occupy in the telescope mirror. There are thus different types of mirror elements. The implementation of the mirror elements exploits the Constructive Solid Geometry (CSG) functionalities in Geant4, that allows to build complex solids from simple ones using boolean operations. To build the mirror elements, 3 to 5 (depending on the type of element) trapezoids are joined and the resulting solid is intersected with a spherical shell. The inner radius of the spherical shell is the curvature of the mirror element. Figure 7.8 shows a visualisation of a mirror element. In the left picture the 5 trapezoids
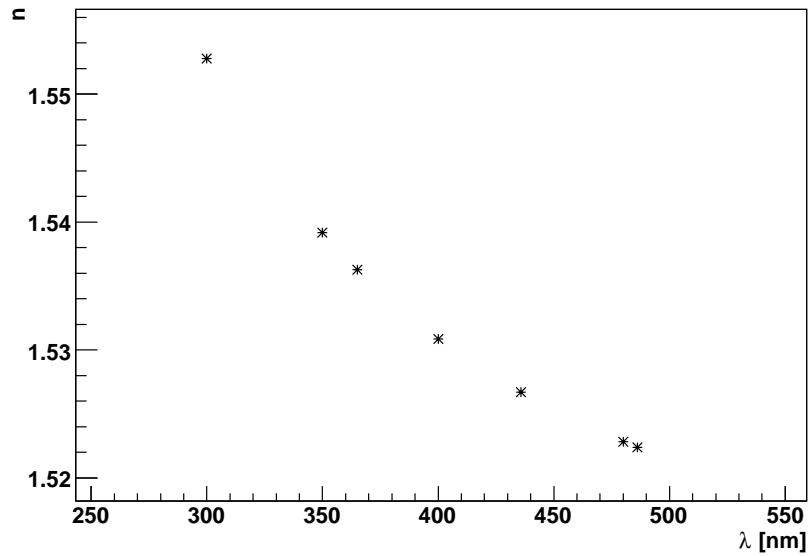
(a) Refractive index of the corrector ring material as a function of the wavelength (λ).
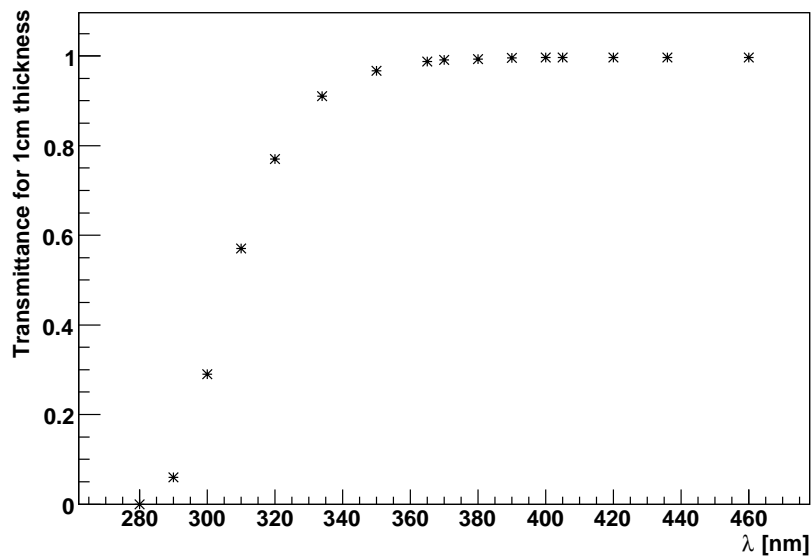
(b) Transmittance for 1 cm of corrector ring material as a function of the wavelength (λ).

Figure 7.7: Optical properties of the corrector ring material.

Figure 7.8: A segment of the Auger FD mirror. Left: the components of the mirror are artificially misaligned to show the internal structure. Right: the mirror segment with all segments properly aligned.

were intentionally misaligned to show the internal structure. Each mirror element is placed according to the vertical and horizontal angles with the vertex, with the alignment point situated in the geometrical centre of the corrector lens. The positioning of the elements emulates the alignment procedure performed in the real telescopes. Each element is placed in such way that the distance from the segment to the alignment point is equal to the segment curvature radius. A visualisation of the complete mirror implemented in the simulation is presented in figure 7.9 . The optical properties of the mirror are implemented by defining the reflectivity in the interface surface between the air and the mirror. The value of reflectivity is constant with the wavelength. The curvature radius, positioning angles and reflectivity are read from an external file containing all the values measured for each segment. An ideal mirror composed of a simple spherical shell is also available in the simulation for testing purposes.

Camera

The camera is composed by the light guides, the photomultipliers and the supporting structure. The light guides are Mercedes stars placed in the vertexes of each photomultiplier. Each Mercedes star is made by the union of three triangular prisms, each built using the Geant4 class G4Polyhedra. The surface interface is defined has having a reflectivity of 0.9 for all wavelengths. A representation of several Mercedes is shown in figure 7.10. The Photomultipliers are hexagons. To simulate the entrance window of the photomultiplier a solid is implemented with a constant refractive index of 1.458. A sensitive detector is placed inside the PMT to simulate

Figure 7.9: Visualisation of the Auger FD mirror as implemented in TelescopeSim-ulatorLX.
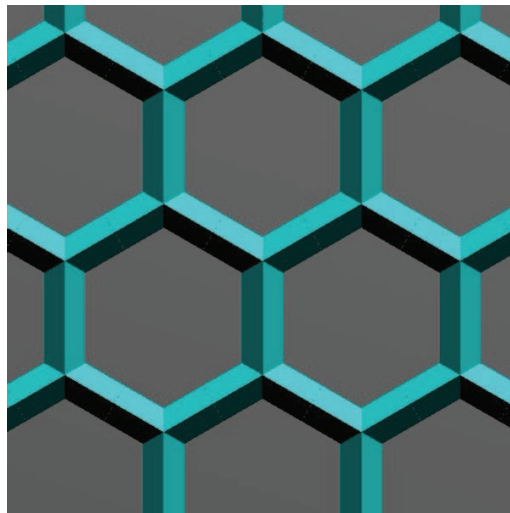
Figure 7.10: The Mercedes stars of the Auger FD as implemented in the TelescopeS-imulatorLX.
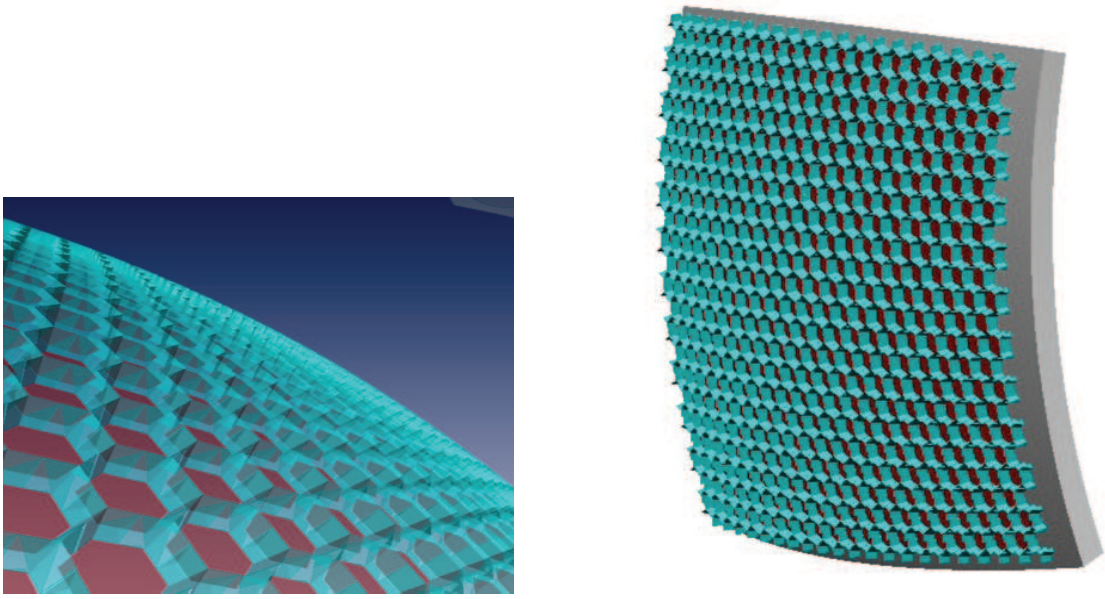
Figure 7.11: The Auger FD camera as implemented in the TelescopeSimulatorLX. Left: detail; Right: the full camera.

the detection of photons in the photocathode. The quantum efficiency is taken into account a posteriori by applying it to the recorded signal at each pixel. Both the PMTs and the light guides are placed following the curvature of the camera. Figure 7.11 shows a visualisation of the camera as implemented in the TelescopeSimulatorLX. On the left, a detail of the camera is shown. On the right, the whole camera is represented, including the camera support in the back of the focal surface. The camera support and feet are implemented to simulate the shadow effect produced due to these elements. A simplified version of the camera is also implemented and used for testing purposes. It consists basically of a spherical surface for the detection of photons placed at the ideal focal surface.

The whole telescope is visualised in figure 7.12. Several sensitive detectors are implemented to allow the passage of photons through the different components of the telescope to be recorded. These sensitive detectors are implemented after the filter, the corrector ring, the mirror and on the ideal focal surface.

A compact version of the module TelescopeSimulatorLX is distributed with the $\overline{\text{Off}}$ $\underline{\text{line}}$. In order to comply with the $\overline{\text{Off}}$ $\underline{\text{line}}$ code policy, this compact version does not implement the output to a separate ROOT file. The output of this version is thus limited to the hits recorded in the PMTs. The other sensitive detectors are not included in this version. Also the visualisation routines are disconnected in this version. The complete version of the module is available upon request.
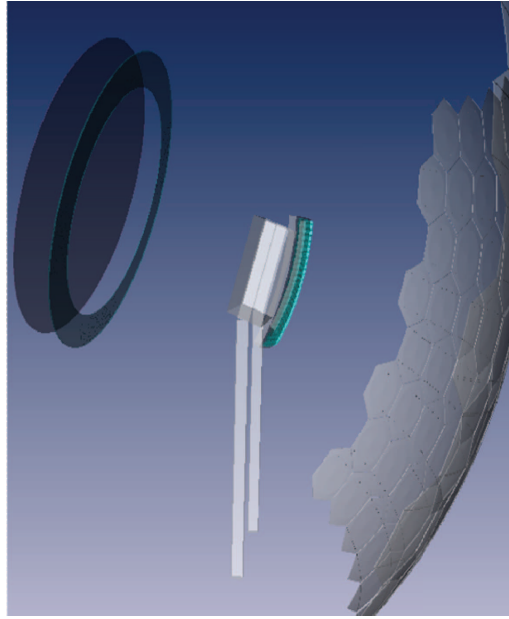
Figure 7.12: The full Auger FD geometry as implemented in the Geant4 simulation
in TelescopeSimulatorLX.

7.3 Telescope Performance Evaluation

The simulation tools were used to evaluate the telescope performance. The optical
spot and the telescope efficiency were studied using the two available simulation
tools.

7.3.1 Simulation Setup

The influence of the optical components is evaluated by characterising the image
produced in the ideal focal surface by parallel rays entering the telescope pupil.
For this purpose four sets of $100\,000$ photons were generated with input angles of
$\theta = 0°$, 5°, 10° and 15° and $\varphi = 135°$. The simulations were performed using the
TelescopeSimulatorKG and the TelescopeSimulatorLX codes. The zenithal angle,
θ, and the azimuthal angle, φ, are defined in the telescope coordinate system. In
this coordinate system the z axis is aligned with the optical axis of the telescope,
pointing outwards, the y axis is horizontal and the x axis is orthogonal to the y and
z axis, pointing downwards. The origin of this coordinate system coincides with the
geometrical centre of the telescope lens.

The position in the camera is defined by the elevation angle, $\alpha = \arcsin\left(x/R_{\mathrm{FS}}\right)$,
and the azimuth angle, $\beta = \arcsin\left(-y/R_{\mathrm{FS}}\right)$ where R_{FS} is the radius of curvature
of the Focal Surface.

For each generated photon its expected position angles $(\alpha_{\text{expected}}, \beta_{\text{expected}})$ in the ideal focal surface are calculated assuming an ideal optical system. For a given photon, the expected position is calculated as the position that a photon, with the same direction, passing in the centre of curvature of the mirror would have in the camera. Then a relative position, in angle, is calculated. The two new variables are then defined as $\alpha_{\text{rel}} = \alpha - \alpha_{\text{expected}}$, $\beta_{\text{rel}} = \beta - \beta_{\text{expected}}$. This definition has the advantage of measuring the deviation of each photon from the ideal situation.

The angular distance (ζ), to the expected position, of a photon in the Focal Surface can be defined as

$$\zeta = \arcsin\left(\frac{\sqrt{(x - x_{\text{exp}})^2 + (y - y_{\text{exp}})^2}}{R_{\text{FS}}}\right)$$

that can be approximated, for small angles, as

$$\zeta = \sqrt{\alpha_{\text{rel}}^2 + \beta_{\text{rel}}^2}$$

This new variable allows an absolute estimation of the deviation of each photon to the expected position to be obtained.

The position of all photons, simulated using the TelescopeSimulatorLX, in the ideal focal surface of the telescope is represented in figure 7.13. In the figure the position of each photon is marked with a dot in a graph of β versus α. The different colour indicated in the figure represent the different incident angles θ. From the figure it can be seen that there are four spots accompanied by some scattered photons.

7.3.2 The Optical Spot with no Obscuration

The fluorescence telescopes have a completely symmetrical geometry with respect to the optical axis, except for the camera obscuration. In a first step its optical properties were studied when there is no camera. For this study the camera implemented in the Geant4 simulation was replaced by a virtual Focal Surface.

The contribution to the optical spot of the photons that pass through the corrector ring and from the photons that pass through the hollow part of the lens was studied.

Figure 7.13: Spots produced in the ideal focal surface for incident angles of 0°, 5°, 10° and 15°. The photons were simulated with no camera obscuration. Each photon is represented by a small dot with a colour corresponding to the input direction: 0°- black; 5° - red; 10°- green; 15° - blue.

Figure 7.14: Spots produced in the ideal focal surface for incident angles of 0°, 5°, 10° and 15°. The photons were simulated with no camera obscuration. For these plots only the photons that do not pass through the corrector lens were selected

Photons with $R_{in} < .85$ (with no corrector ring)

The optical spot produced in the Focal Surface by the photons that do not pass in the corrector ring is presented in figure 7.14. In the figures each photon position, in terms of $(\alpha_{rel}, \beta_{rel})$, is represented by a dot. The photons were selected to have a position in the lens plane with a radius $R < 0.85\,\mathrm{m}$. The input angles are indicated in the graphs.

The spot is quite featureless, presenting a complete circular symmetry, expected from the complete circular symmetry of the Schmidt telescope (camera excluded). Moreover the spots for the different input angles are very similar, which is also explained by the geometric symmetry of the telescopes.

Photons with $R_{in} > .85$ (with corrector ring)

The contribution from photons that pass through the corrector lens ring is shown in figure 7.15. For the photons with an input angle of $\theta = 0°$ the circular symmetry is maintained. For larger angles the symmetry is lost and the spot is deformed in the same direction as the input direction of the photons. The corrector ring shape depends only on the radius R. However, for inclined photons, the angle between the
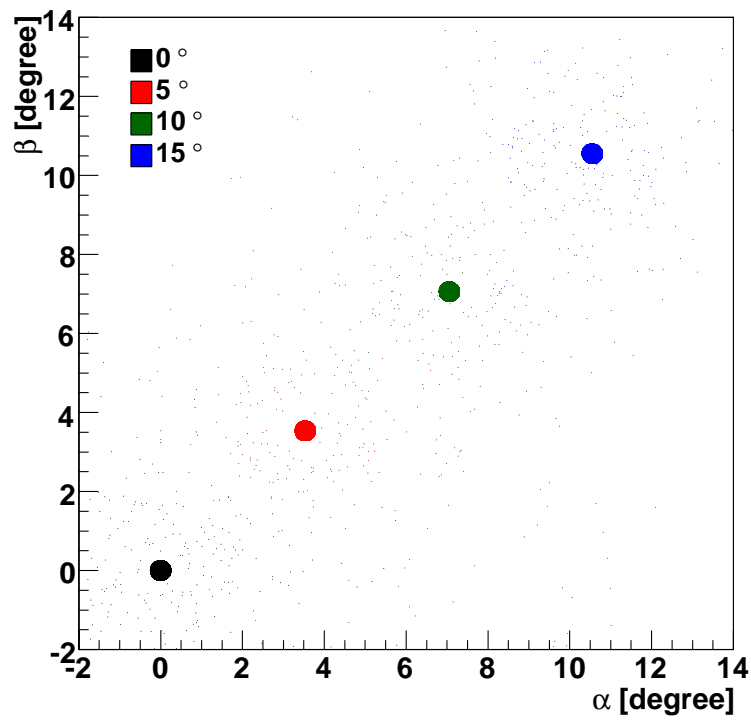
Figure 7.15: Spots produced in the ideal focal surface for incident angles of 0°, 5°, 10° and 15°. The photons were simulated with no camera obscuration. For these plots only the photons that pass through the corrector lens were selected.

input photon and the normal to the curved surface has a dependence in φ, for the same R. Thus the correction to the photon angle introduced by the lens will have a dependence with φ, producing the asymmetrical spots seen in figure 7.15.

All Photons

The optical spot produced by all the photons passing through the diaphragm at four incident angles are represented in figure 7.16.

To have an insight of the dependence of the spot size with the input position of the photons, in the diaphragm, is shown, in figure 7.17, the deviation from the expected position in the focal surface (ζ) versus the input radius of the photon. In the figure it is indicated in grey the zone where the camera shadow will cut the photons and the zone where the input photons pass through the lens. In the region of $0.4 < R_{\text{Diaphragm}} < 0.85$ m, where there is neither camera shadow nor lens, the aberration has a minimum at $R_{\text{Diaphragm}} \sim 0.75$ m and a maximum at $R_{\text{Diaphragm}} \sim 0.45$ m. The later one is translated in figure 7.14 by the clear cut on the spot edge. It is also seen that the aberration starts to rise quite rapidly from the minimum with the input radius having a value of $\sim 0.23°$ for an input radius
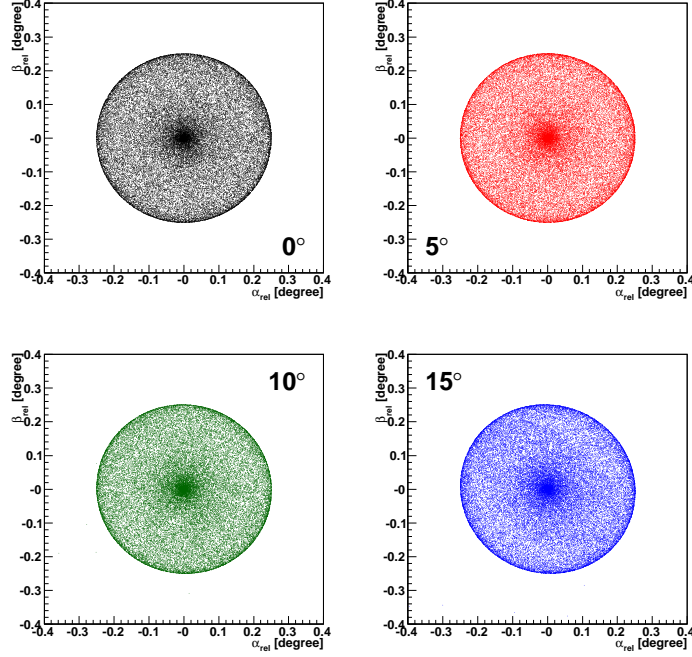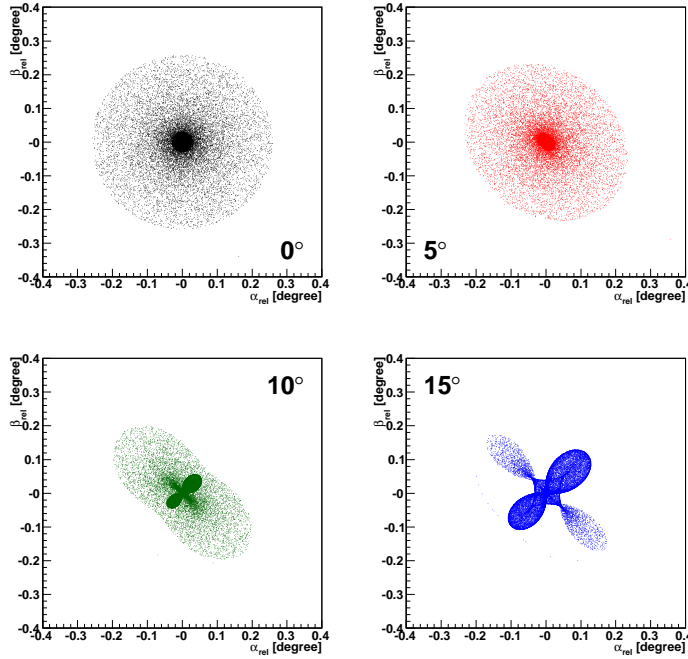
Figure 7.16: Spots produced in the ideal focal surface for incident angles of 0°, 5°, 10° and 15°. The photons were simulated with no camera obscuration.

of $R_{\mathrm{Diaphragm}} = 0.85$ m. For a fluorescence telescope with no corrector ring and a radius of 0.85 m the maximum aberration would be then given by the maximum at $R_{\mathrm{Diaphragm}} \sim 0.45$ m. However, if the aperture radius were to be increased without the introduction of a corrector ring the aberration would continue to rise quite rapidly taking a value of $\zeta \sim 1.375°$ for a radius of 1.1 m. This aberration value corresponds to a spot with a radius of about 42 mm. The introduction of the corrector ring increases the pupil area of the telescope from $2.27\,\mathrm{m}^2$ to $3.80\,\mathrm{m}^2$ (67% increase) maintaining the aberration of the telescope. However, taking into account the reduction due to the camera shadow of about $0.8\,\mathrm{m}^2$, that is present in both cases, the collection area is doubled from $1.47\,\mathrm{m}^2$ to $3.00\,\mathrm{m}^2$.

7.3.3 Obscuration Effects

The shadow of the camera plays an important role in the fluorescence telescope, reducing the collection area by a factor greater than 20%. Moreover the square shape of the camera breaks the symmetry of the optical system. The camera, its body and support structure are described in detail in the TelescopeSimulatorLX module. Figure 7.18 presents the spot for different input angles when the camera shadow is taken into account in the simulation. The contribution to the spot shape
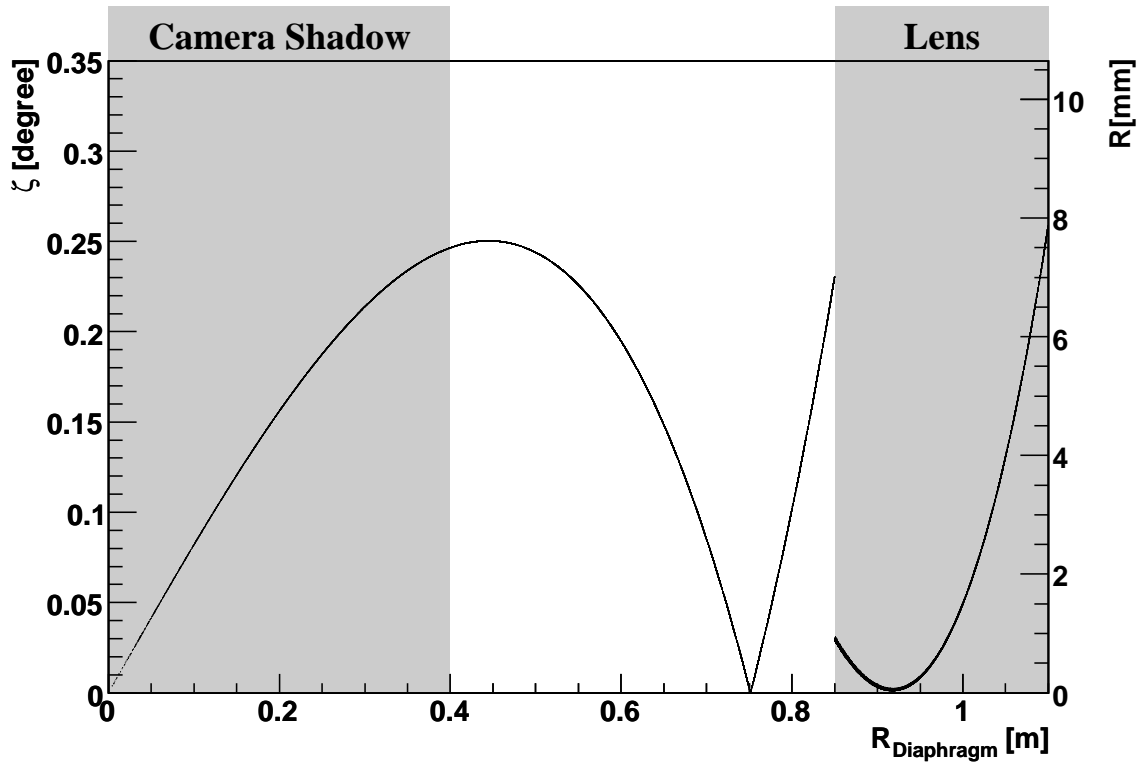
Figure 7.17: Deviation from the expected position in the focal surface in angle, ζ, as a function of the input radius, $R_{\text{Diaphragm}}$. The camera and lens zone are indicated in grey. Photons were generated with incident angles of $0°$.

Figure 7.18: Spots produced in the ideal focal surface for incident angles of 0°, 5°, 10° and 15°. The camera obscuration was simulated.

from the photons that pass through the hollow part of the lens and from the photons that pass through the corrector ring are presented in figure 7.19 and figure 7.20, respectively. To better understand the camera shadow it is plotted in figure 7.21 the position of the photons in the mirror, in $(\alpha_{rel}, \beta_{rel})$, for the four simulated input angles. The shadow of the camera produces the white hole seen in the figures. The square part corresponds to the camera body while the two "thick lines" correspond to the legs that support the camera in place. The photons that pass through the lens are represented in red while the others are plotted in black. For the input angles of 0°and 5° it is seen that the camera shadow only affects the photons that pass through the hollow part of the lens. For 10°and 15° some of the photons that pass through the corrector ring are shadowed. However the percentage of photons killed is smaller for these photons than for the ones that pass by the hole in the lens.

From figure 7.18 it is clear the asymmetry introduced by the camera obscuration reflected in the spots shape. From the two plots where the contribution to the spot is separated it is clear that most of the asymmetry arises from the photons that pass through the hollow part of the Lens. It is also seen in figure 7.19 that for higher input angles there is a reduction of the photon density in a quarter to a half spot. This introduces a shift on the barycentre of the spot. However this shift is very small since the centre of the spot has a very high density of photons.

121
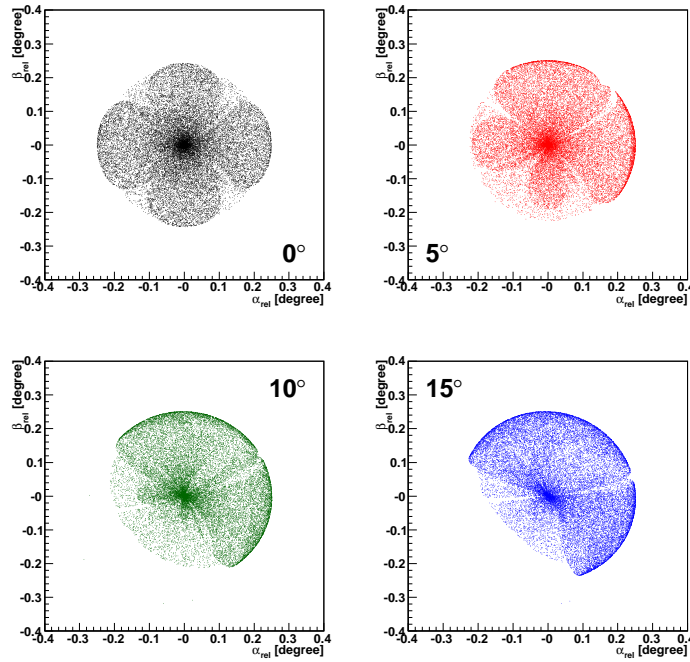
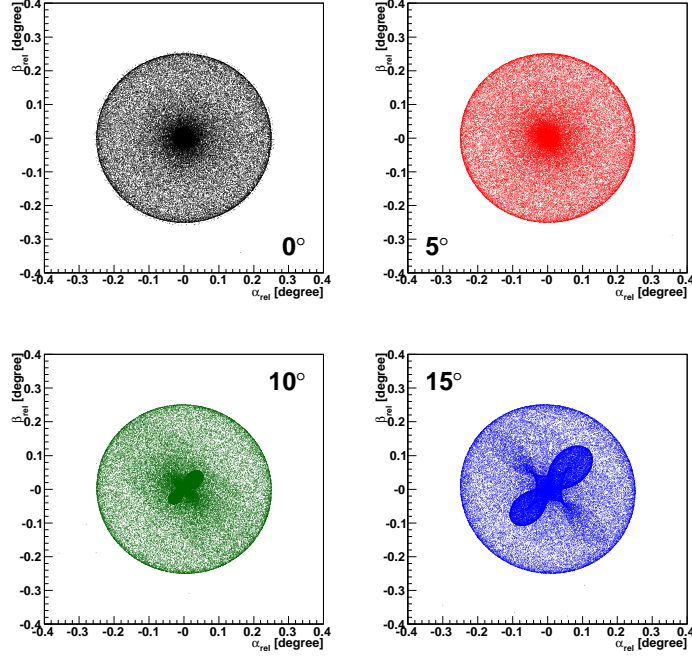Figure 7.19: Spots produced in the ideal focal surface for incident angles of 0°, 5°, 10° and 15°. The photons were simulated with camera obscuration. For these plots only the photons that do not pass through the corrector lens were selected

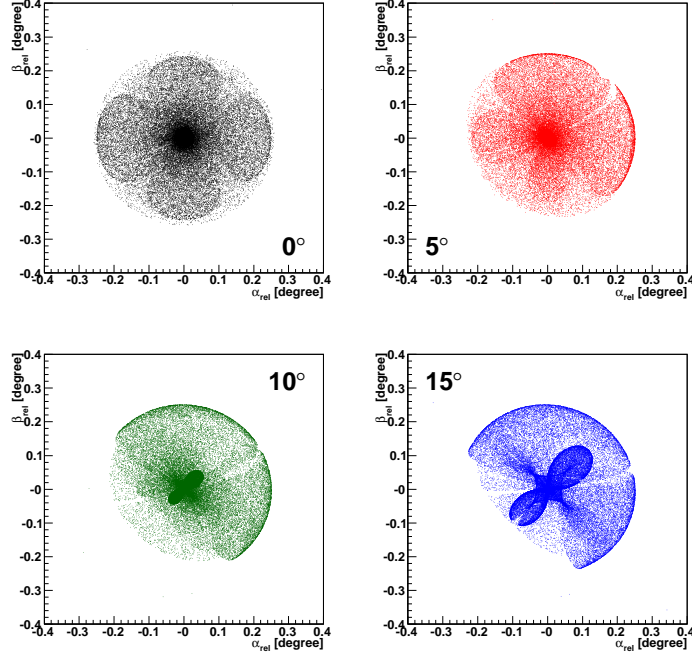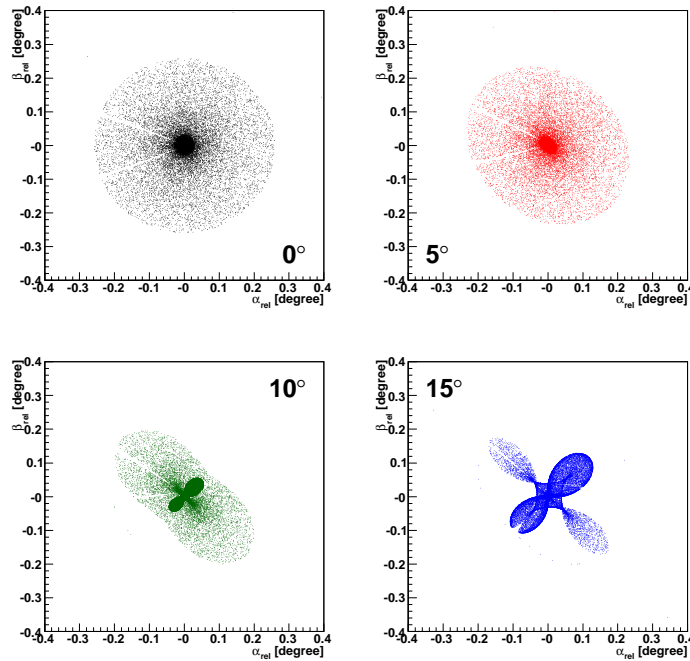Figure 7.20: Spots produced in the ideal focal surface for incident angles of 0°, 5°, 10° and 15°. The photons were simulated with camera obscuration. For these plots only the photons that pass through the corrector lens were selected.
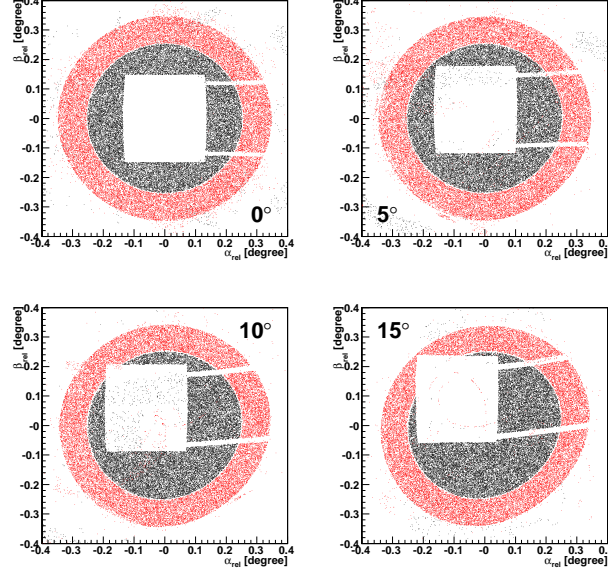
Figure 7.21: Photons in the mirror for incident angles of 0°, 5°, 10° and 15°. The photons were simulated with camera obscuration. The photons that pass through the hollow part of the lens are plotted in black while the photons that pass through the lens are plotted in red.

7.3.4 Spot Size

The simulations produced were used to study the spot size at the focal surface. The effect of the lens on the spot size and its dependence with the lens profile and incidence angle were evaluated.

The Effect of the Corrector Ring

Figure 7.22 represents the distributions of ζ for the photons in the ideal focal surface for photons simulated with the TelescopeSimulatorLX (solid lines) and the TelescopeSimulatorKG (dashed lines). For each simulation the distribution of the photons that pass through the hollow part of the lens is represented in red and for the photons that pass through the lens in blue. The distribution for all detected photons is represented in black. From the left plot it is evident that most of the photons lie in the region of $0° < \zeta < 0.25°$. However, for the TelescopeSimulatorLX, there are a small fraction of photons that have higher ζ in the focal surface up to 6.2°. The photons with $0.25° < \zeta < 6.2°$ represent a fraction of 0.34% of the total number of photons. From the figure it can also be seen that all of these photons pass through the corrector ring. It was also seen from the simulation that these photon give hits in the filter with a different position than the one they were generated with.

123
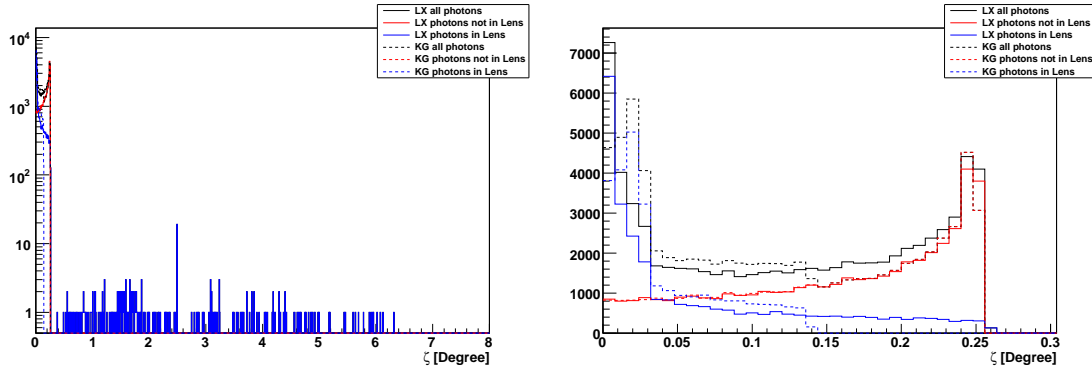
Figure 7.22: Distribution of ζ for the photons in the ideal focal surface. The right plot is a zoom of the left one in the range $0° < \zeta < 0.30°$

This facts suggest that these photons are reflected in the lens, coming back to the filter and then reflected again. In the right plot it was made a zoom to region of $0° < \zeta < 0.30°$. In the figure it can be seen that there is a good agreement in the simulation of photons that pass through the hollow part of the lens. The agreement is not so good for the photons that do pass in the lens and this is reflected in the overall distribution. To better understand the spread of the photons in the focal surface, the cumulative distribution of ζ is drawn in figure 7.23. The curves follow the same colour scheme of the previous image. In this figure the cumulative curves for all detected photons are normalised to 1. The curves for individual contributions are normalised to one over the total number of detected photons to represent the relative contribution to the overall cumulative curves. A horizontal dashed line is drawn to indicate 0.9 of the cumulative distribution, allowing the size of the spot that contains 90% of the photons to be easily estimated. In the figure it can be seen the good agreement between the two simulations for the photons that do not pass through the lens. The two simulation show a difference for the photons that pass through the lens which is reflected in the cumulative curve for all detected photons up until $\zeta < 0.25°$. Although the two simulations present such difference the spot size, that contains 90% of photons, is in both simulations equal to 0.24°.

Dependence with the Corrector Ring Profile

The corrector ring plays an important role on the fluorescence telescope. The shape of the lens influences directly the spot shape and thus the performance of the telescope. To study the spot shape the TelescopeSimulatorLX was used to simulate four sets of photons, each with 100 000 photons, with an input angle $\theta = 0°$ and different lens profiles. The cumulative curves for the different profiles are shown in figure

Figure 7.23: Cumulative curves of ζ for the photons in the ideal focal surface simulated with the TelescopeSimulatorLX (solid) and the TelescopeSimulatorKG (dashed). The contributions of the photons that pass through the lens (red) and the photons that pass through the hollow part of the lens (blue) are represented as the overall (black) cumulative curve.

7.24 . In a dashed black line the cumulative curve obtained using the TelescopeSimulatorKG simulation code is represented. The solid lines were obtained using the TelescopeSimulatorLX simulation code. The profiles used correspond to the "KG" profile (in black), the "circular" profile (in red), the "upper limit" (in blue) and "lower limit" (in green) profiles. The first thing to note in the figure is that the two simulation codes are in agreement, provided that the TelescopeSimulatorLX uses the profile implemented in the "KG" code. The cumulative curves have small variations, apart from the "upper limit" curve, showing values for the spot size, at 90%, in the range $0.20° < \zeta < 0.22°$. The curve for the "upper limit" shows a spot size of $\zeta = 0.24°$. However at a $\zeta \sim 0.25°$ the curves seem to converge. This indicates that if the spot size is defined to include 99% of the photons there is very small variation of the spot size with the lens profile.

The Effect of the Gaps in the Corrector Ring

Due to the large size of the corrector lenses (2.2 m outer diameter) they had to be manufactured in pieces. In the design [52] it is specified that each lens was sectioned in 24 segments of 15°. However, in situ, it was observed that the gaps between the segments were not regular and could, in the worst case, amount to
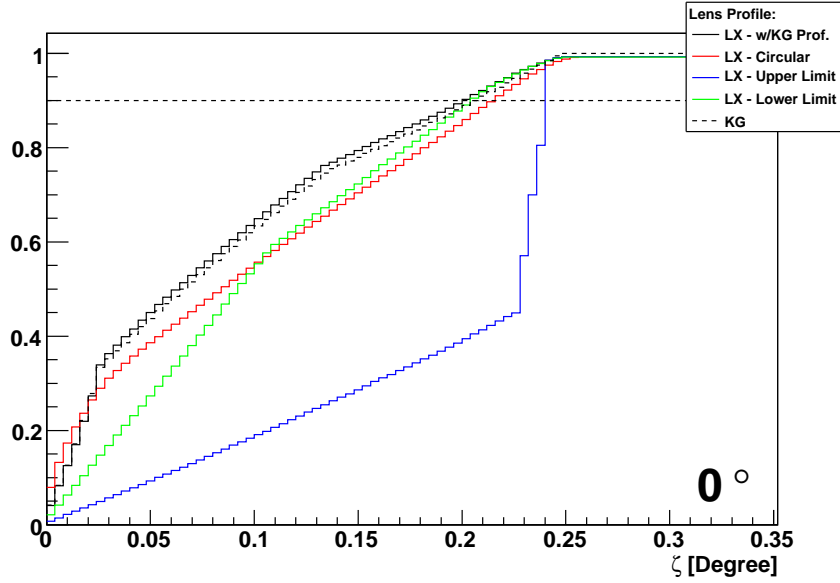
Figure 7.24: Cumulative curves of ζ for the photons in the ideal focal surface simulated with the TelescopeSimulatorLX. Black - "KG" profile; Red - Circular profile; Blue - "Upper Limit" profile; Green - "Lower Limit" profile. A dashed black curve represents the cumulative curve simulated with the TelescopeSimulatorKG code.

several centimetres. The effect of these gaps on the spot in the focal surface was studied using the TelescopeSimulatorLX code. In face of the lack of measurements of these gaps, the gaps were implemented by reducing, evenly, the covered angle of each segment to 14.735° and equally spacing the 24 segments.

The Spot produced by an unsectioned corrector ring is shown in the left image of figure 7.25 while in the right image the spot produced using the sectioned corrector ring is shown. It is evident that a star-like effect appears in the spot. Photons lying in the "arms" of this star are photons that passed through the gaps of the corrector lens and its direction was thus not corrected by the lens. These photons have a maximum deviation from the expected position of $\sim 1.5°$ which corresponds to the spot size that would be obtained if the corrector ring was not used. However, the fraction of "uncorrected" photons is small and corresponds to the area of the gaps over the total pupil area that amounts to $\sim 0.7\%$.

Dependence with Incidence Angle

The dependence of the spot size with the input angle, and different simulations, is studied by plotting the respective cumulative curves in figure 7.26. In the figure the solid lines are obtained using the TelescopeSimulatorLX code while the dashed
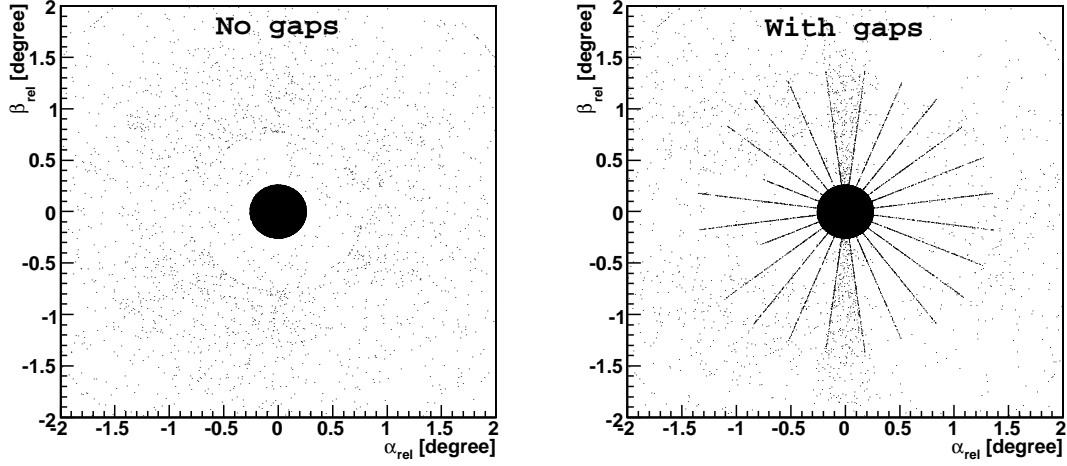
Figure 7.25: Spots produced in the ideal focal surface. The left image was obtained by simulating the corrector ring without gaps. In the right image the corrector ring was sectioned in 24 segments of 14.735°.
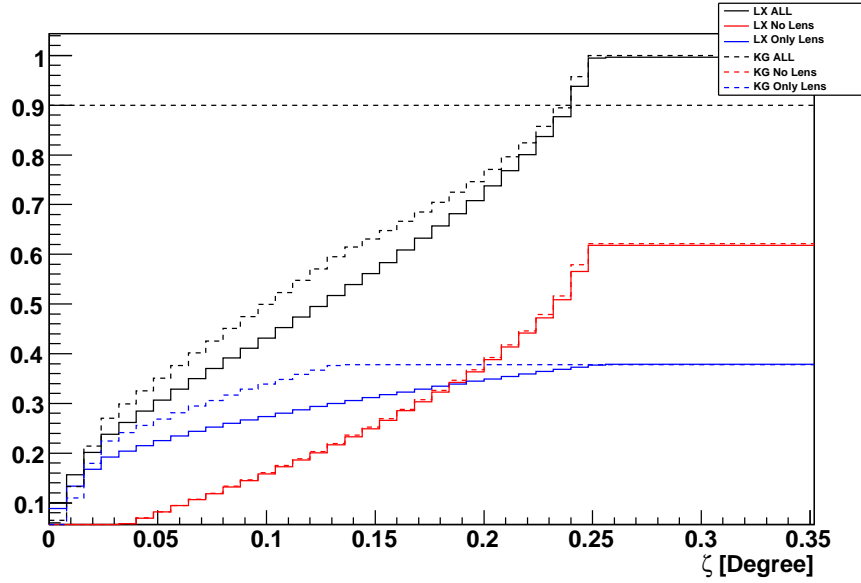

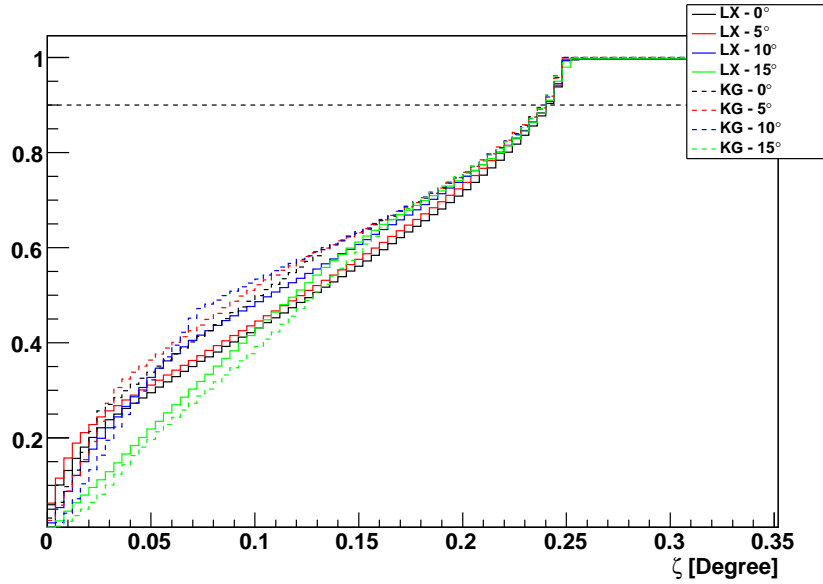Figure 7.26: Cumulative curves of ζ of the photons in the focal surface simulated with the TelescopeSimulatorLX (solid) and TelescopeSimulatorKG (dashed). The input photons have input angles of 0° (black), 5° (red), 10° (blue) and 15° (green).

lines are for the TelescopeSimulatorKG code. The curves for photons with input
angles, θ, of 0°, 5°, 10° and 15° are respectively represented in black, red, blue and
green. As expected from the previous figure there are small differences between the
cumulative curves using the TelescopeSimulatorLX and the TelescopeSimulatorKG.
Moreover the shape of the cumulative curve, and thus the spot shape, varies with
the input angle. However the spot size, at 90%, does not vary with the input angle
and simulation code.

7.3.5   Photon Distribution in the PMTs

Photons in the focal surface propagate reaching the Photomultipliers placed behind.
The inefficiency areas between the PMTs are overcome by the use of the Mercedes
stars where the photon reflects to a PMT. In figure 7.27 the position of the photons
in the PMT are represented. In the top figures, 7.27(a) and 7.27(b), each photon is
represented by a dot. Black dots represent the photons that hit a PMT directly while
the blue dots represent photons that have at least one reflection in the Mercedes
before hitting the PMT. Red dots represent the last reflection in the Mercedes for
photons that will reach a PMT while the green dots represent the same for photons
that aren't collected in a PMT after reflecting. A violet circle with a radius of 0.25°
is drawn as a reference to indicate the spot size in the focal surface. In the bottom
figures, 7.27(c) and 7.27(d), are presented histograms where the photon density is
represented in a logarithmic colour scale with the same range. In all figures solid
blue lines are drawn to indicate the pixel boundaries and dashed ones to indicate the
Mercedes boundaries. The figures in the left were obtained by simulating photons
with an expected position in the centre of a pixel. The input directions were set
with $\theta = 0.866°$ and $\varphi = 0°$. On the other hand the photons in the right plots were
generated with $\theta = 0°$ in order to have an expected position in the centre of the
camera and thus in the vertex of a Mercedes star.

The first fact to notice from the figures is that the spot is larger in the PMT than
in the Focal Surface. This is due to the fact that the photons reach the focal surface
with large incident angles. This can be seen from figure 7.28 where the distribution
of the incident angles for the photons that hit the focal surface is plotted. The
photons in the figure were generated with an input angle $\theta = 0°$. The gap in the
plot at an incident angle of $\sim 29°$ is directly related to the low photon density in
a circular zone in the mirror seen in figure 7.21 which, in turn, derives from the
internal border of the corrector lens. As the PMTs are recessed by $\sim 18\,\text{mm}$, the
height of the Mercedes light guides, a photon with an incident angle of 30° deviates,

(a) Photons directed to pixel center

(b) Photons directed to mercedes center

(c) Photons directed to pixel center

(d) Photons directed to mercedes center
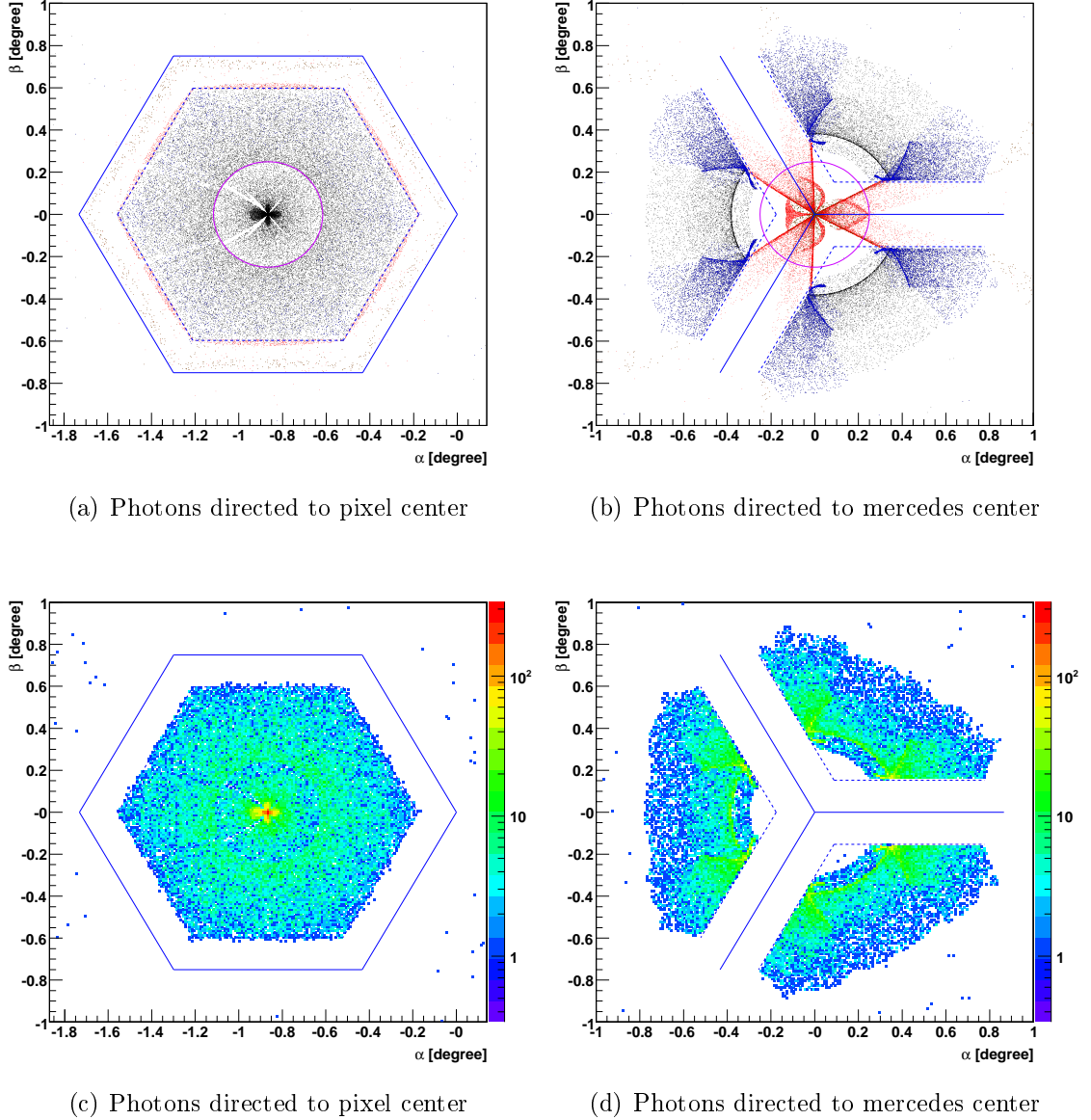
Figure 7.27: The spot seen in the PMTs. Top figures are scatter plots of the position of the photons. The photons that hit directly the PMT are represented in black while in blue are represented the photons that have at least one reflection in the Mercedes before hitting a PMT. In red is represented the last hit in the Mercedes. In green are represented the hits in the Mercedes for photons that do not hit a PMT. A violet circle with a radius of 0.25° represents the size of the spot in the focal surface. Bottom figures are histograms of the photon density in the PMT. The density is indicated by a logarithmic colour scale. In all figures blue lines are drawn to represent the pixel boundaries (solid) and the Mercedes boundaries (dashed).
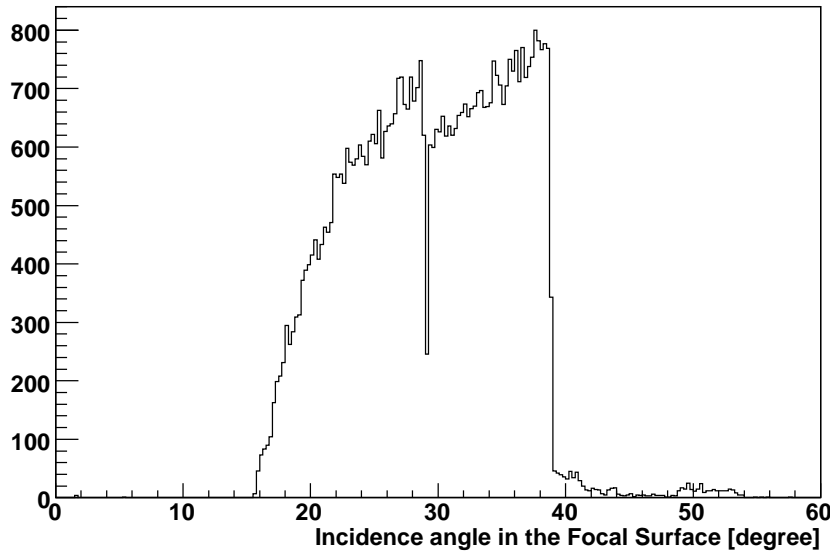
Figure 7.28: Distribution of the incident angles for the photons that arrive to the ideal focal surface for photons generated with an input angle $\theta = 0°$.

horizontally, approximately 10 mm from its position in the focal surface.

Despite this enlargement, the spot in the left images of figure 7.27 is contained inside the pixel with few hits on the Mercedes and consequently few photons hitting the PMT with a previous reflection on the Mercedes. From the bottom left histogram it can be seen that there is a high density region in the centre of the pixel.

When the photons are directed to the Mercedes centre the three adjacent PMTs are hit. It can be seen from figure 7.27(b) that there is a direct component of hits in the PMT that is enlarged as in the previous case. However there is a large fraction of photons reflected in the Mercedes. These photons hit the PMT in very specific zones near the Mercedes, seen in the figure by the high density zones of blue dots. It can also be seen that the photons that do not reach a PMT are in the central region of the Mercedes. The figure 7.27(d) shows the density of photons in the PMT and is drawn using the same colour scale and range as the left one. It can be seen that there is no region with such high density as the central region in the bottom left figure. Also it can be noticed that there is some kind of a circle, centred in the Mercedes vertex, where there are no photon hits in the PMT. This is due to an effect of shadowing of the Mercedes star. The density of photons has a circular symmetry around the centre of the Mercedes. The highest density of photons is located near one of the vertexes of the hexagonal PMT.

Regarding the efficiency there are some differences between the two studied cases.

130

When the photons are directed to the pixel centre, 1.7% of the photons are lost after reflecting in a Mercedes. On the other hand, when the photons are directed to the Mercedes vertex, this number rises to 4.4%. The overall efficiency, defined as the number of photons detected in a PMT over the number of photons in the focal surface is of 94% and 88%, respectively. Part of this efficiency reduction is explained by the decrease of the number of photons arriving on the PMT window after reflection in a Mercedes. The other part is probably due to reflections in the PMT window before hitting the photocathode of the PMT. The reflection probability depends on the impinging angle and thus different configurations can lead to different efficiencies.

From the two cases studied it can be concluded that the "illuminated" zones of the PMTs vary with the position of the spot centre. The collection efficiency of a PMT varies with the distance to its centre. Such dependency influences the overall telescope efficiency with the spot centre position. If necessary, the effect can be easily taken into account in the TelescopeSimulatorLX simulation code, if a model of the PMT efficiency dependence with the radius is provided.

7.3.6 Telescope Efficiency

The optical efficiency of the telescope results from the convolution of the different efficiencies of the optical components and relates the number of photons that are able to reach the focal surface with the number of collected photons. The efficiency was evaluated using the simulations described before. The efficiency is then defined as the ratio between the photons that arrive to the focal surface and the generated photons:

$$\varepsilon = \frac{N_{\mathrm{FS}}}{N_{\mathrm{generated}}}$$

In figure 7.29 the optical efficiency of the fluorescence telescope is presented as a function of the input radius at the diaphragm ($R_{\mathrm{Diaphragm}}$) for photons with a direction perpendicular to the input pupil. The curves represent the efficiency obtained using the TelescopeSimulatorKG (red) and the TelescopeSimulatorLX (blue) and the efficiency obtained if the requirement that the photons fall inside a circle such that $\zeta < 0.27°$ for the TelescopeSimulatorKG (orange) and for the TelescopeSimulatorLX (violet). The red curve is not visible as it is overlapped by the orange one. In the region where $0 < R_{\mathrm{Diaphragm}} < 0.4\,\mathrm{m}$ all the photons are killed by the shadowing of the camera. For higher input radius the efficiency curve grows as the camera is square shaped and the fraction of photons killed is reducing until the efficiency of the system is given by the convolution of the filter transmittance and the mirror reflec-
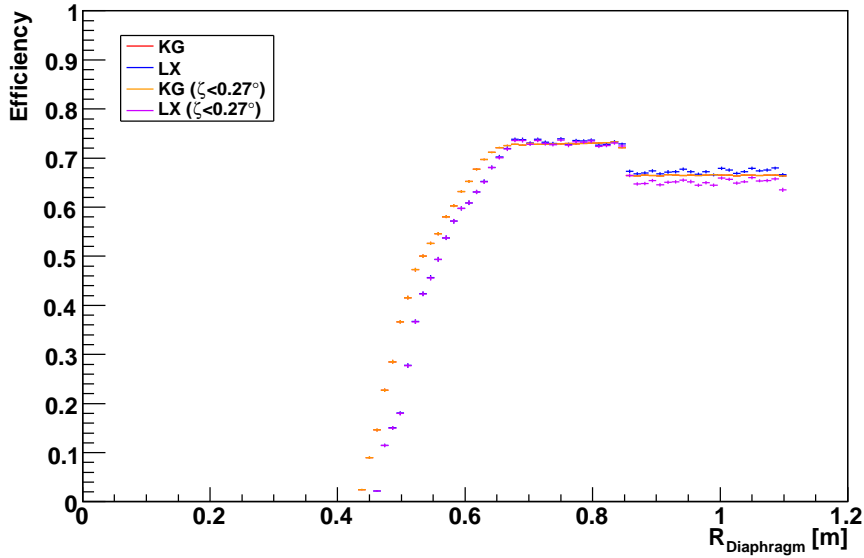
Figure 7.29: Telescope efficiency versus the radius at the diaphragm of incident photons. The photons were generated with an incident angle $\theta = 0°$.

tivity. For $R_{\text{Diaphragm}} > 0.85$ m the photons pass through the corrector lens and its inefficiency causes the global efficiency to drop. It is probable that the camera structure has slight differences in its description on the two simulation codes, producing slightly different obscurations of the camera which is translated in a difference on efficiency in the region where $0.4 < R_{\text{Diaphragm}} < 0.7$ m. The overall efficiency for the two simulation codes is estimated as 54.17% for the TelescopeSimulatorKG and 53.11% for the TelescopeSimulatorLX representing a difference of $\sim 1\%$. The spots generated using the TelescopeSimulatorLX code have a small component of photons with high ζ that will be considered as noise in the analysis of the events. Discarding the photons with a $\zeta > 0.27°$ reduces the optical efficiency to 52.22%, representing a reduction of $\sim 1\%$.

Figure 7.30 is equivalent to the previous one but the photons have an input angle of $\theta = 10°$ at the entrance pupil. In this case there are evident differences between the two simulation codes used in the regions where the photons start to enter the corrector ring of ($R_{\text{Diaphragm}} \sim 0.85$ m) and near the end of the diaphragm ($R_{\text{Diaphragm}} \sim 0.85$ m). This difference is explained by the fact that in the TelescopeSimulatorLX the filter, a circle that defines the input pupil and has the same size of the corrector ring, is placed, following the specification design and confirmed on site, 10 cm before the corrector lens and thus 10 cm before the centre of curvature of the mirror. In the TelescopeSimulatorKG the filter is placed in the plane of the
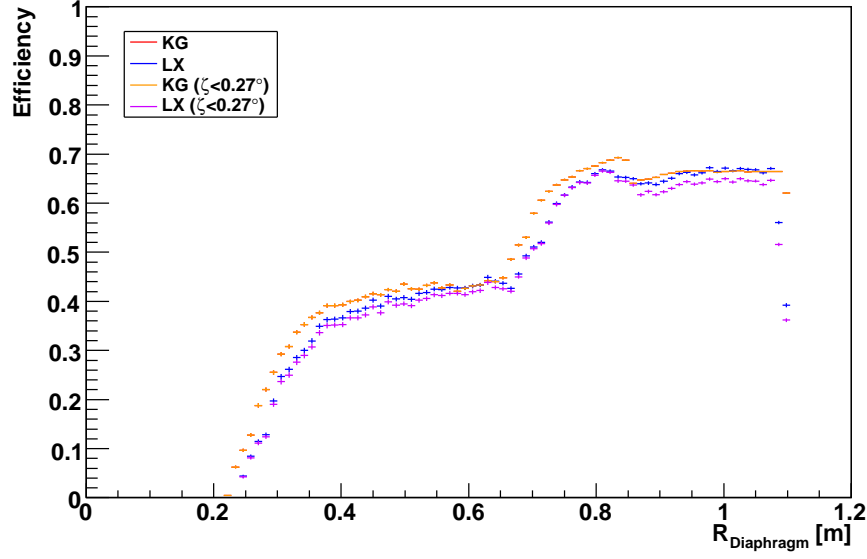
Figure 7.30: Telescope efficiency versus the radius at the diaphragm of incident photons. The photons were generated with an incident angle $\theta = 10°$.

lens. Thus, in the TelescopeSimulatorLX, there is an effect of a projection of the pupil circle in the lens circle, reducing the collection area for inclined photons. The overall efficiency for the two simulation codes is, in this case, estimated as 53.83% for the TelescopeSimulatorKG and 51.63% for the TelescopeSimulatorLX representing a 2.2% difference. Moreover if the cut at $\zeta < 0.27°$ is imposed, the efficiency using TelescopeSimulatorLX would be of 50.28%, representing a reduction of $\sim 1.4\%$.

A test was performed, placing in the TelescopeSimulatorLX the filter near the lens. The resulting curves for the efficiency are shown in figure 7.31 . It is clear that the differences between the simulations are reduced. In this test the overall efficiency, estimated with the TelescopeSimulatorLX yields a value of 52.29%, if all photons are considered, which represents a reduction of $\sim 1.5\%$. If only photons with $\zeta < 0.27°$ are considered an efficiency of 50.89% is obtained which represent a reduction of 1.4%.

Two spots images are shown in figure 7.32 where it is evident a component at large angles. One million photons were simulated with the TelescopeSimulatorLX with input angles of $\theta = 0°$ (left) and $\theta = 10°$ (right). The spot appears, in both cases, in the expected position with its star structure due to the corrector ring gaps. In the first case, $\theta = 0°$, the photons with $\zeta > 0.27°$ amount to 8898 and the ones with $\zeta > 8°$ to 72 (of 10^6 generated photons). In the second case, $\theta = 10°$, the spot image presents additional structures besides the spot centred at $(\alpha, \beta) = (7°, 7°)$.

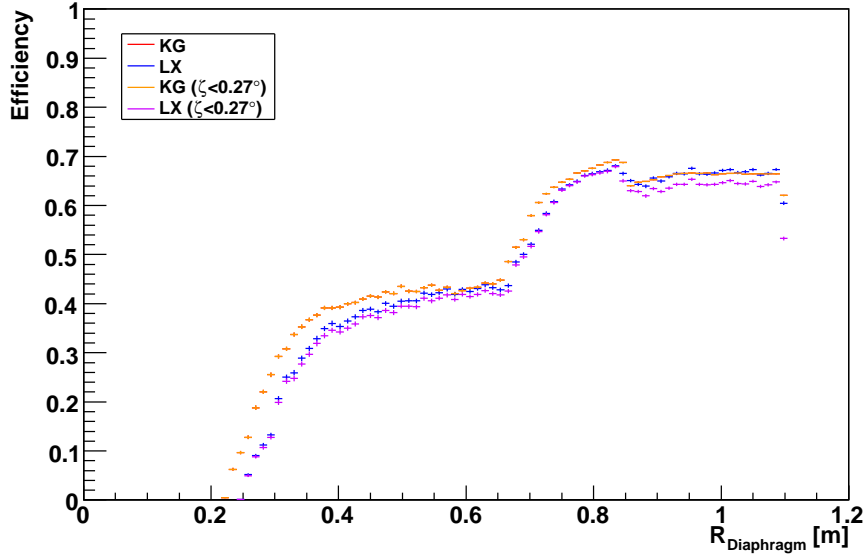Figure 7.31: Telescope efficiency versus the radius at the diaphragm of incident photons. The photon were generated with an incident angle $\theta = 10°$. The filter was placed close to the corrector lens in the TelescopeSimulatorLX
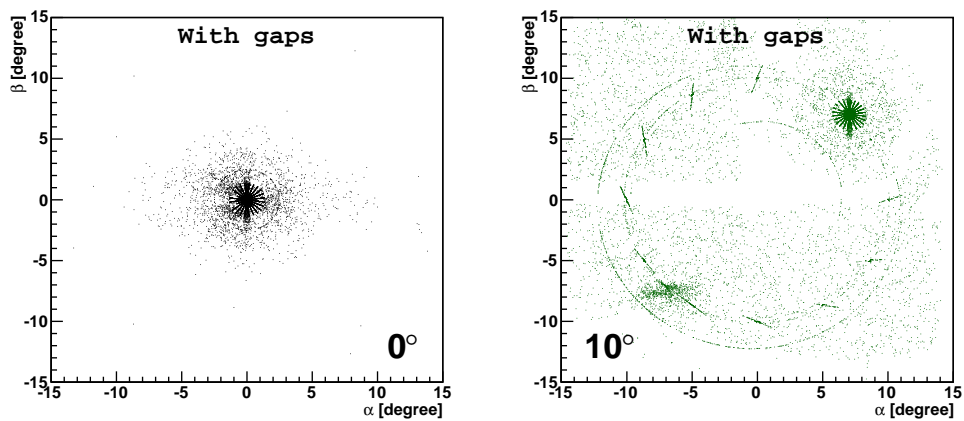
Figure 7.32: Spots in the focal surface simulated with the TelescopeSimulatorLX. Photons were generated with an input direction $\theta = 0°$(left) and $\theta = 10°$.
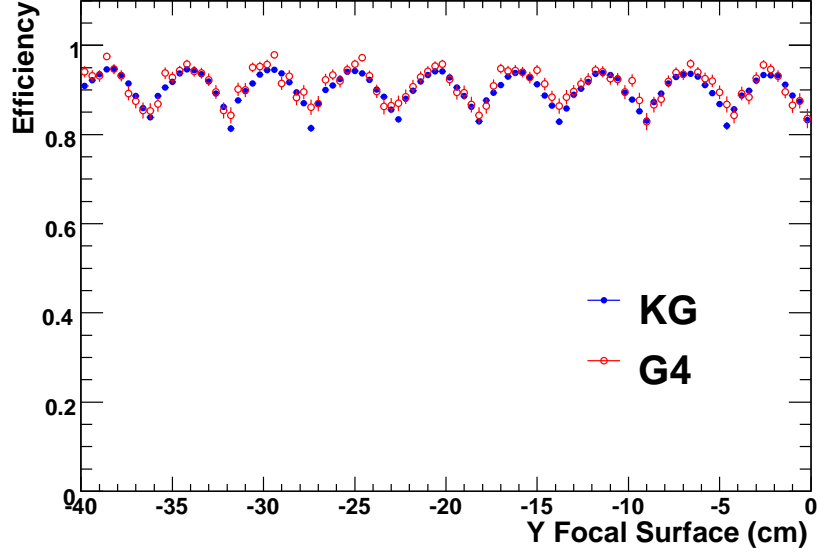
Figure 7.33: Efficiency versus the horizontal position in the camera.

Two circumferences, some lines and also a ghost spot at $(\alpha, \beta) \sim (-7°, -7°)$ appear. The circles and lines are related to reflections in the lens segments surfaces. The ghost spot is the result of photons that get reflected in the camera, travel back to the lens and/or filter where they are reflected and imaged again in the camera. The photons that are imaged with $\zeta > 0.27°$ amount to 13449 and the ones with $\zeta > 8°$ to 7327 (of 10^6 generated photons).

The efficiency of the Mercedes and PMT was evaluated by simulating photons with random incidence direction in order to illuminate the whole camera. A thin strip in the centre region was then selected. The photons in this strip were used to plot the efficiency as a function of the horizontal position in the camera. This plot is seen in figure 7.33. The zones of higher efficiency correspond to the photons arriving directly to the PMTs and the low efficiency zones are due to the reflections in the Mercedes before hitting the PMTs.

7.4 Comparison Between Simulation and Data

7.4.1 Comparison with Laboratory Data

Using TelescopeSimulatorLX, the uniformity measurements described in [56] were simulated. In this measurement, a small version of the camera with seven pixels was used. In the absence of an optical system, the optical conditions of the Auger

135
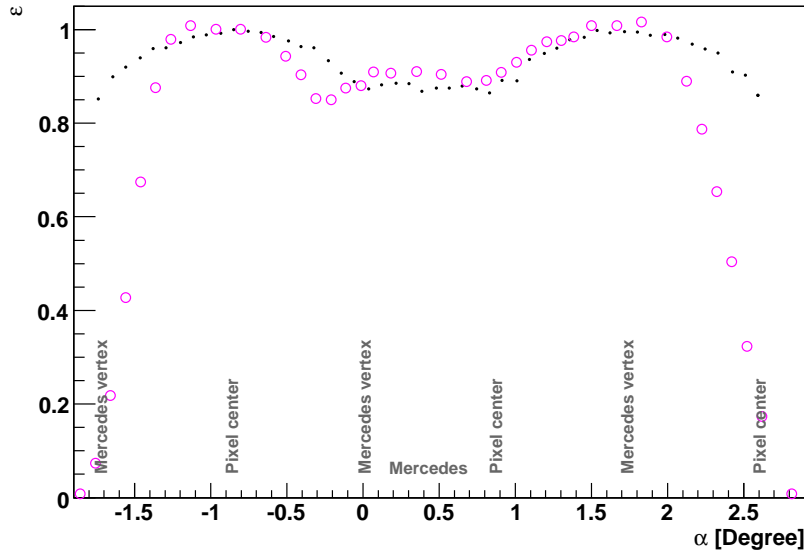
Figure 7.34: Relative efficiency along a vertical line passing through Mercedes ver-
texes. The black dots are the simulation results and the white circles are the mea-
surements from [56].

FD were approximately reproduced by diffusing the light from a Xenon flash lamp
inside a cylinder made in such a way that the realistic angles of incidence in the
camera were obtained (approximately between 10° and 30°, due to the shadow of the
camera and the aperture of the diaphragm, respectively). Since the FD optics is fully
simulated with Geant4, this setup is easily simulated using TelescopeSimulatorLX
by fully illuminating the diaphragm with parallel light rays with incident directions
such that a scan of the seven central pixels was performed.

As in [56], two scans, one passing over the Mercedes arms and one passing over
the Mercedes vertexes, were performed. The position of the photons in the camera
is defined here by the elevation angle, $\alpha = \arcsin\left(x/R_{\mathrm{FS}}\right)$, and the azimuth angle,
$\beta = \arcsin\left(-y/R_{\mathrm{FS}}\right)$ where R_{FS} is the radius of curvature of the focal surface. The
efficiency is defined as the ratio between the number of photons that arrive at the
PMTs and the number of generated photons. The efficiencies are normalised to
the efficiency value in the centre of the central pixel. The results are shown in
figures 7.34 and 7.35, where the measurements in [56] are shown for comparison.
Good agreement is found in both cases, and the efficiency variations are of the
order of 15% over the camera surface. The result of 0.85 for the lowest value of the
efficiency obtained in the measurements is thus reproduced by the simulation. The
steep fall in the extremes of the scan in the laboratory data is due to the fact that
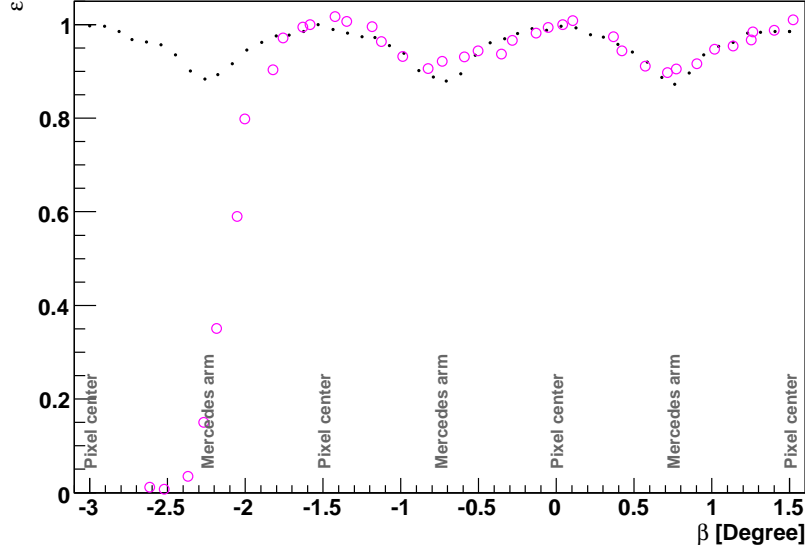
Figure 7.35: Relative efficiency along a horizontal line passing through pixel centres. The black dots are the simulation results and the white circles are the measurements from [56].

in the laboratory setup only 7 pixels were present.

7.4.2 Comparison with Laser Events

The Central Laser Facility (CLF)[57], placed within the array at a position equidistant from the Los Leones, Los Morados and Coihueco FDs, fires 355 nm vertical or inclined laser pulses with an energy of 8 mJ. The light from the laser beam is diffused in the atmosphere and detected by the FDs. As the light from the laser beam travels upwards in the atmosphere it is isotropically diffused. Some of this diffuse light is emitted towards the Fluorescence Telescopes. The light propagates through the atmosphere for around 30 km suffering attenuation until it reaches the detector. At each moment in time the CLF can be considered as a point source, producing a spot in the focal surface dominated by the optical properties of the telescope.

In figure 7.36 the track of a vertical laser shot in the FD camera is shown in (α, β) coordinates along with a zoom of the region of interest. The corresponding measured light profile (number of photons as a function of time) is shown in 7.37 . This typical profile is the convolution of the attenuation and scattering of the upgoing laser beam with the attenuation of the light from the laser to the fluorescence telescope and the non-uniformities of the FD camera. Here we are interested in isolating this last effect. In this study, the lower part of the shower track was

Figure 7.36: Track of a vertical laser shot. A zoom is presented in the image on the right.

Figure 7.37: The laser light profile.

discarded to avoid the region in which Mie scattering cannot be neglected. In the same way, the upper part of the shower track was discarded to avoid the timeslots with low statistics.

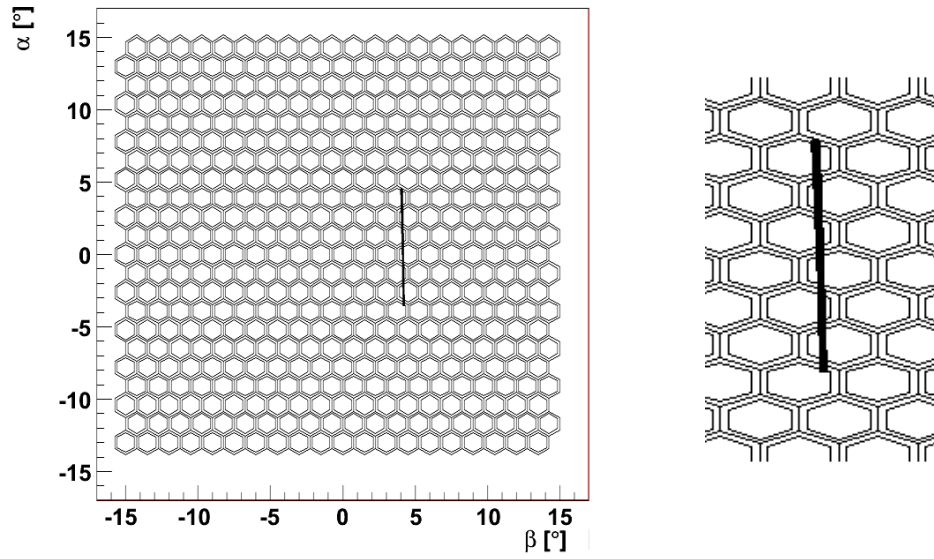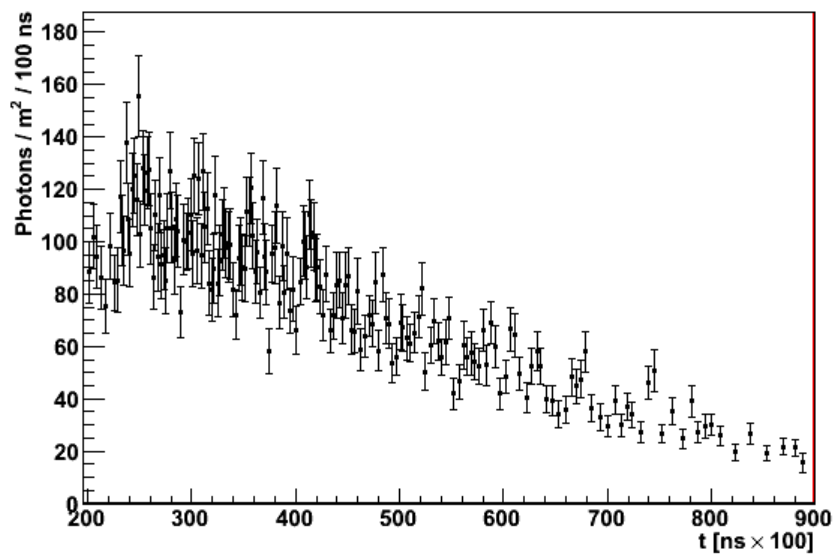The expected number of photons arriving at the telescope diaphragm, N_γ^{lens}, with a direction falling within a given (α, β) bin can be parametrised as:

$$N_\gamma^{\text{lens}} = I_0 \times exp\left(-\frac{d_1}{d_0}\right) \times dir(h) \times \Delta\Omega(h) \times exp\left(-\frac{d_2}{d_0}\right)$$

where I_0 is the laser intensity, the first exponential term describes the attenuation of the upgoing laser beam in terms of the atmosphere traversed d_1, the function $dir(h)$ describes the beam scattering at the height h, $\Delta\Omega(h)$ is the solid angle subtended by the telescope aperture at a given point of the laser beam and the second exponential term describes the attenuation of scattered photons when they traverse an atmospheric depth of d_2 in its propagation from the scattering point in the beam to the eye. In fact, $dir(h)$ describes the direction dependence of Rayleigh scattering (in other words its differential cross-section) and is well described by a second degree polynomial:

$$dir(h) = a_0 + a_1 cos\theta_z + a_2 cos\theta_z^2$$

where θ_z is the photon scattering direction with respect to the direction of the up going laser beam.

The number of photons expected in the camera, N_γ^{camera}, in the same (α, β) bin is given by

$$N_\gamma^{\text{camera}} = N_\gamma^{\text{lens}} \cdot \varepsilon_{\text{telescope}}$$

where $\varepsilon_{\text{telescope}}$ is the telescope efficiency and can be expressed as

$$\varepsilon_{\text{telescope}} = \varepsilon_{\text{mean}} \cdot \varepsilon_{\text{relative}}$$

where $\varepsilon_{\text{mean}}$ is the average efficiency of the telescope and $\varepsilon_{\text{relative}}$ contains the efficiency variations along the camera. This relative efficiency is thus given by the ratio between the number of detected photons, N_γ, and the average expected signal, $\overline{N_\gamma^{\text{camera}}} = N_\gamma^{\text{lens}} \cdot \varepsilon_{\text{mean}}$.

Taking into account that the constant terms like I_o and $\varepsilon_{\text{mean}}$ can be absorbed by the free parameters, that there is a one-to-one transformation between the laser curve camera coordinates (α, β) and the time slot and assuming that the atmospheric density varies with the height h as $\rho(h) \propto e^{-h/L}$, the average number of photons in
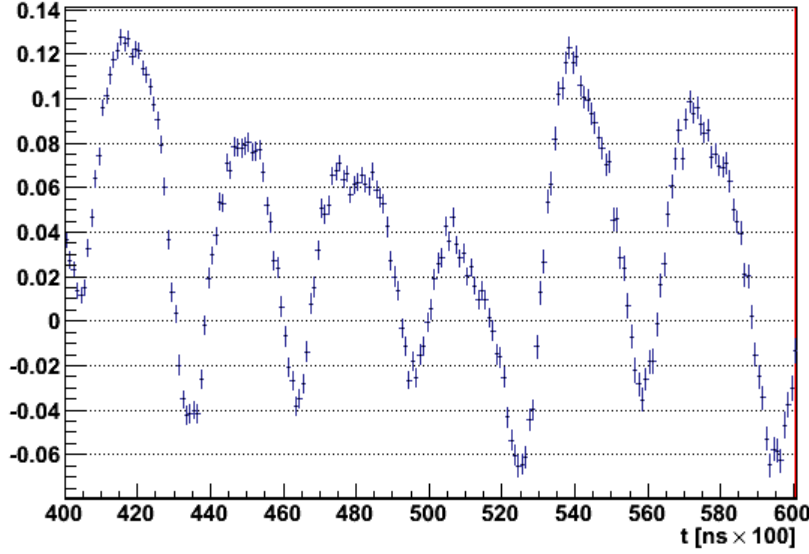
Figure 7.38: Relative differences of the fitted and measured number of photons. The
average over one month of laser data is shown.

each time bin can be expressed as

$$\overline{N_\gamma^{\text{camera}}}(t) = \frac{2c^2t^2}{c^4t^4 + l^4} \cdot \left(\frac{P_3}{t^2} + P_2 \cdot t + P_1\right) \times$$

$$\exp\left\{\left[\frac{-1}{L}\left(\frac{c^2t^2 - l^2}{2ct} - \left(\frac{c^2t^2 - l^2}{2ct}\right)^2 + \left(\frac{c^2t^2 - l^2}{2ct}\right)^3\right)\right]\frac{1}{2(c^2t^2 - l^2)}\right\}$$

where c is the speed of light, l is the distance from the laser to the fluorescence
telescope and P_1, P_2, P_3 and L are free parameters. These free parameters are fixed
fitting this formula to the laser light profile.

The relative differences between the fitted value and the measured number of
photons (N_γ), given by

$$\frac{N_\gamma - \overline{N_\gamma^{\text{camera}}}}{\overline{N_\gamma^{\text{camera}}}}$$

are shown in figure 7.38. In the figure the data result from the average of the laser
data available in one month. The distribution of the values in the figure have a
mean value of 0.03. The same analysis for other months shows that the mean value
is stable and varies between 0.03 and 0.04. The non-existence of a trend in these
data indicate that the method used to extract the relative efficiencies is reliable and
stable.

In figure 7.39 the relative efficiencies $\varepsilon_{\text{relative}} = \frac{N_\gamma}{N_\gamma^{\text{camera}}}$ for 18 months of laser data
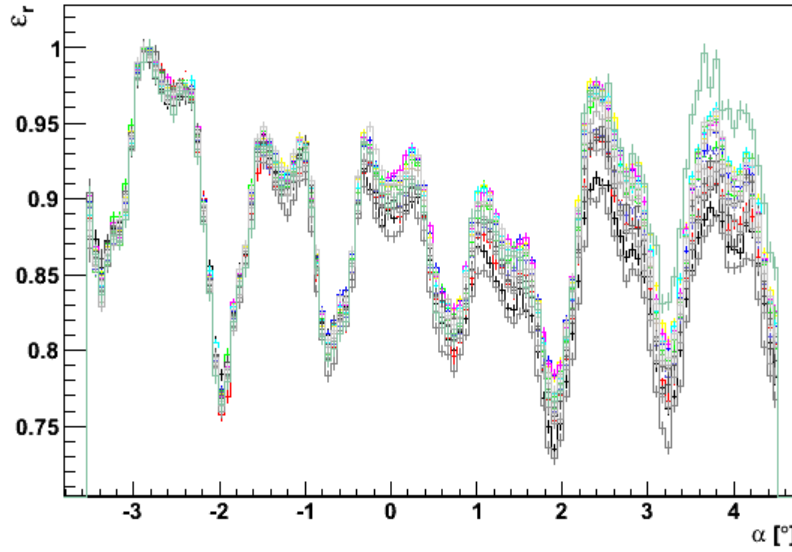
Figure 7.39: Relative efficiency across the FD camera for 18 months of CLF laser shots.

are shown. The values obtained were rescaled setting the maximum to 1. In this figure the reduction in the efficiency due to the Mercedes is clearly visible. It is also clear that the relative efficiency is quite stable over this 18 month period. It can also be seen that there are variations in the maximum and minimum efficiencies from pixel to pixel which is unexpected if all the pixels were equivalent.

In figure 7.40 the relative efficiency estimated with laser data is compared to the one obtained with the $\overline{\text{Off}}$ line standard laser simulation. While the overall shapes agree, there are some differences between the simulation and the data. In particular, the data show deeper valleys than the simulation and do not reproduce some features that seem to be related to individual pixels.

The variations from pixel to pixel can be smoothed out by folding the laser data into a virtual pixel. In this virtual pixel a vertical laser shot actually scans two different regions of the pixel in β. The virtual pixel with the positions scanned by the laser track is shown in figure 7.41. To better evaluate the efficiency drop between the central region of the pixel and the peripheral region, six regions were defined in the virtual pixel, as shown in figure 7.42. Regions 1 and 2 are defined near the centre of the pixel and should be the areas of the pixel with higher efficiency, while regions 3, 4, 5 and 6 are defined in the Mercedes area and should present a reduced efficiency, due to the Mercedes inefficiency. The efficiency for all the points that fall inside each region was averaged and the results are shown in figure 7.43. The ratio

141
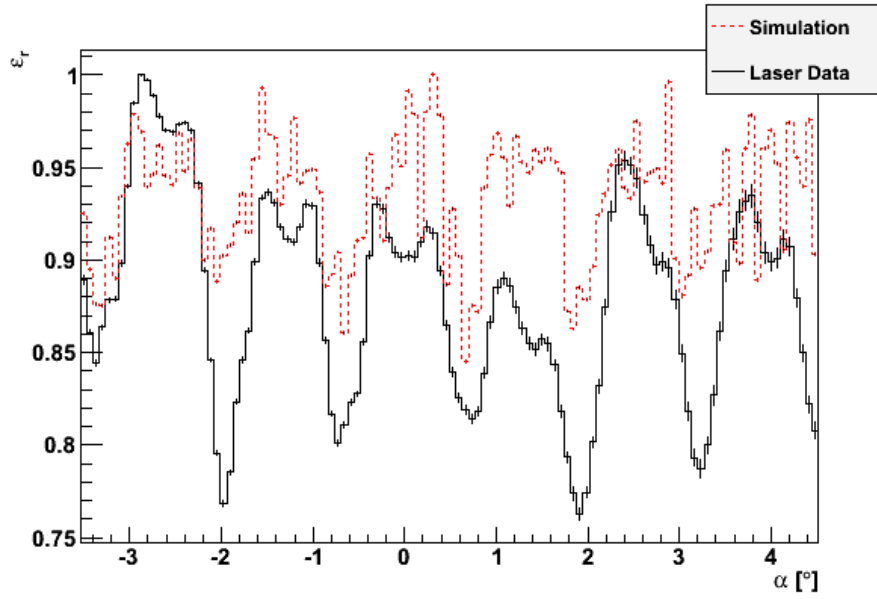
Figure 7.40: The relative efficiency across the FD camera measured from CLF laser
shots (solid black line) and obtained with the standard $\overline{\text{Off}}$ $\underline{\text{line}}$ simulation (dashed
red line).
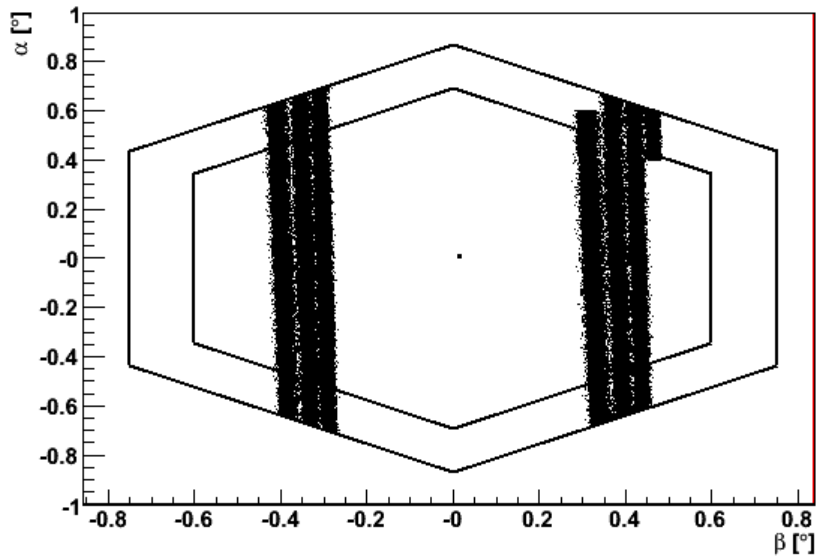
Figure 7.41: The virtual pixel with the folded laser track represented.
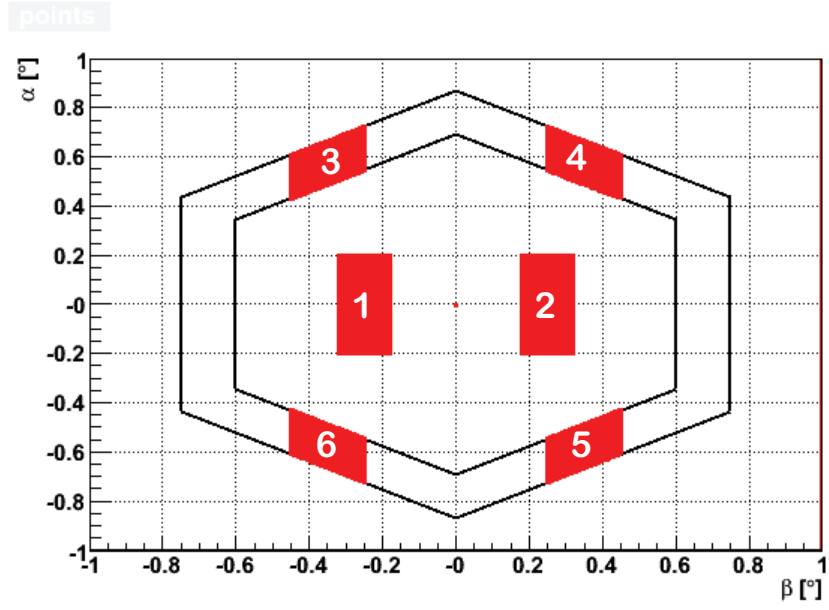
Figure 7.42: The six regions defined on the virtual pixel for the calculation of the R parameter.
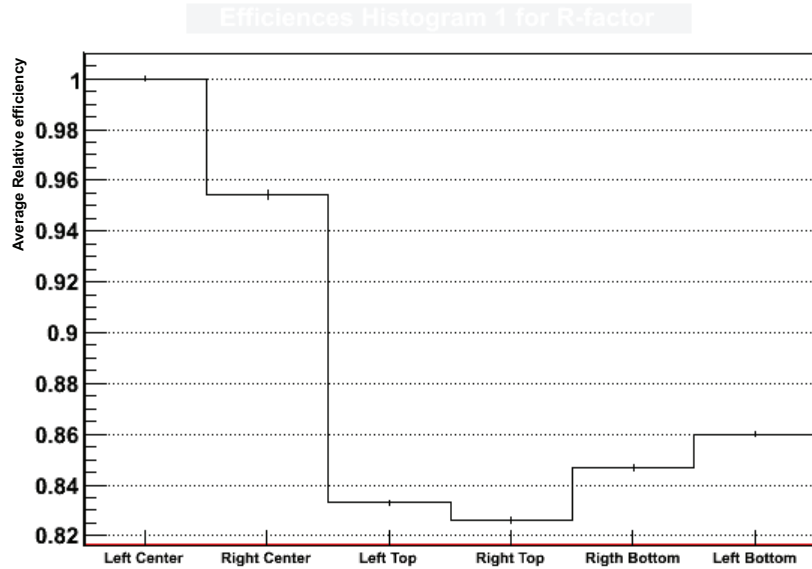
Figure 7.43: Relative efficiency for the six zones defined in the virtual pixel.
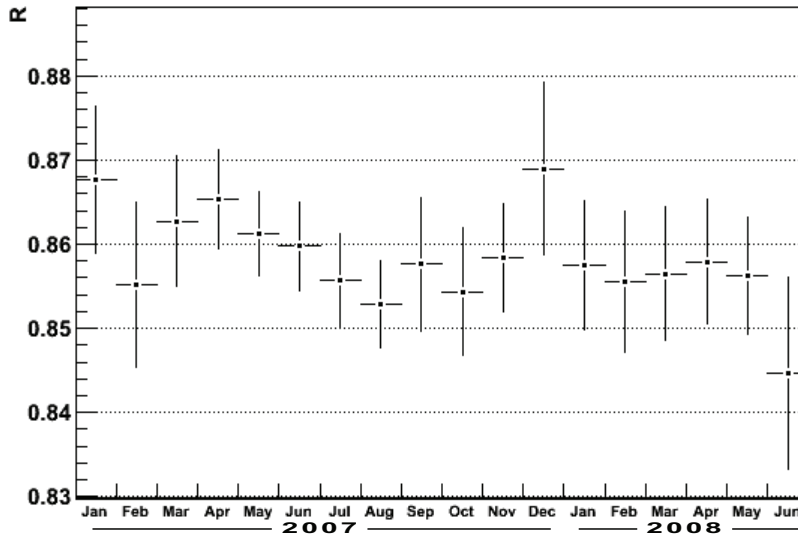
Figure 7.44: Evolution of the R parameter, obtained from laser data, with time.

R between the average efficiency in the peripheral regions and the average efficiency
in the central regions measures the efficiency drop due to the Mercedes and amounts
to $R = 0.858 \pm 0.008$. In figure 7.44 the evolution of the R parameter with time for
an 18 month period is shown. It can be seen that this parameter is, within errors,
stable over time.

The R parameter was also evaluated using the TelescopeSimulatorLX, and the
value obtained, $R = 0.937 \pm 0002$, is not compatible with the result obtained from
laser data. This difference may be related to a bad description of the optical spot
and/or to the Mercedes efficiency in the simulation. A first study of the influence
of the Mercedes reflectivity and of the spot size was performed using the Geant4
simulation. Two different configurations were tested and scans were performed in
the central pixel of the laser track.

In the first configuration the Mercedes surface reflectivity in the simulation was
reduced from the nominal value of 0.90 to 0.85 and to the limit value of 0. In figure
7.45 the relative efficiency is shown versus the angle α in the central region of the
camera for the laser data and for the Geant4 simulation with a Mercedes reflectivity
of 0.85 and 0. In the right image the data have been rescaled setting the maximum
to 1. If the spot was very small, a reduction on the Mercedes efficiency should only
affect the region of the scan on top of the Mercedes (around $\alpha \sim 0.7°$). Namely,
when the reflectivity was set to 0 the efficiency in this region should also drop to
0 as no photons would be reflected. However, from the left figure it is clear that
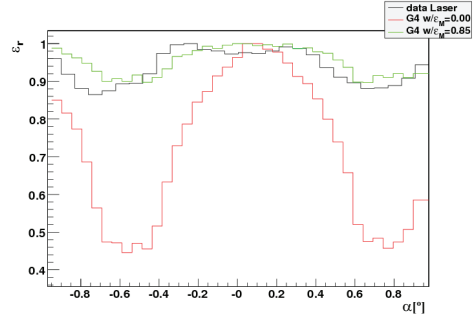
Figure 7.45: Profiles of the relative efficiency versus the angle α in the central region of the camera. Data is represented in black. In green and red are represented the simulations with a Mercedes reflectivity of 0.85 and 0, respectively. The data on the right image has been rescaled setting the maximum to 1.

the efficiency drop is lower than expected. Moreover the reduction in the Mercedes efficiency affects also the central region. This indicates that the spot, along the incident directions, is such that there is a reflected component when photons are directed to the pixel centre and that there exists a direct component when the photons are directed to the Mercedes. Thus, changing the Mercedes reflectivity the simulation can reproduce the deeper valleys seen in the data but affects also the whole profile shape making a smoother transition.

To test the influence of the spot size in the relative efficiency, the flexibility of the TelescopeSimulatorLX was used to reduce, in an effective way, the optical spot size. This reduction was achieved by rescaling the positions and incidence angles of the photons in the focal surface. Two scans were performed with scale factors of 100% and 10%, representing two limit cases, and two scans with intermediate scan factors of 70% and 50%. The relative efficiencies for the four scans are shown in figure 7.46 . The scan with a 10% scaling factor puts in evidence the reduction in the efficiency in the Mercedes areas, due to the reduction of the direct component, and the increase of the relative efficiency in the central regions as the component reflected in the Mercedes is reduced. It can also be seen that the profiles get steeper with the reduction of the spot size.
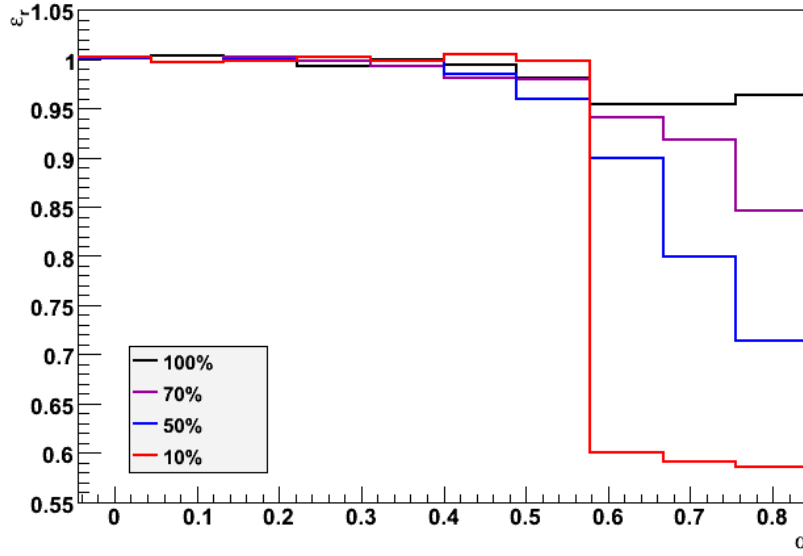
Figure 7.46: Profiles of the relative efficiency versus the angle α in the central region of the camera for several spot sizes. The four profiles were made with scaling factors of 100%, 70%, 50% and 10% are represented with different colours that are indicated in the legend.

Neither of these effects can, by itself, correct the disagreement between data and simulation. A more systematic study will be therefore needed. This study should include laser data from the several fluorescence eyes and, if possible, shower events data.

Chapter 8

Conclusions

The work in this thesis was developed in the framework of astroparticle experiments, namely in the context of EUSO, the Pierre Auger Observatory and GAW. The main focus is in the development of hardware and firmware for data acquisition and trigger systems and detailed studies of the detectors.

In this thesis was presented the first general purpose data acquisition board for cosmic rays developed at LIP - The LIP-PAD. This board was the building block of the DAQ system of ULTRA - a support activity for the EUSO mission, and was able to cope with all the experiment requirements. This board was also applied in the TRC - a public education and outreach project installing cosmic ray detectors in high schools. In the course of the project it was observed that a greater degree of autonomization of the DAQ system was important. This fact triggered the development of a new generation of the board, giving birth to the LPV3, incorporating performance upgrades (200 MHz sampling with 12 bits in resolution) and standalone operation (ethernet communication and processing capability). The board is currently in the prototyping phase. The final version will allow a completely autonomous DAQ system in the TRC project and will also provide a simple, yet high performance, data acquisition system for small experiments.

An important achievement was the installation, at Lisbon, of the LIP e-CRLab, an electronics laboratory dedicated to cosmic ray physics. This laboratory has state of the art equipment that will allow LIP to participate in the development of sophisticated instrumentation for cosmic ray detectors. The laboratory is centred on the development and test of firmware for FPGA based DAQ systems. Nevertheless, the laboratory has also the tools to produce electronics boards and prototypes to interface DAQ system and to test the adopted solutions. Some prototype boards have already been produced completely in the laboratory and final versions have

been designed and assembled in the laboratory. One other benefit of the laboratory is related with education. From September 2008 onwards, periods of training for first cycle students were organised. The first course in digital electronics, for second cycle students, will begin in the spring semester of 2008-2009. This will give students the opportunity to became familiar with the state of the art techniques and instruments used in digital electronics.

The design and implementation of trigger systems in the context of the single photon counting technique was also pursued. The firmware development and implementation became possible with the installation of the e-CRLab. First, the algorithms are implemented in firmware. Afterwards hardware tests are performed. LIP has taken the responsibility not only for the trigger system but of a major part of GAW DAQ firmware development. The different firmware components needed to be tested separately which implied the production of interface boards. Functional tests of the ProDacq were performed using a prototype interface board designed and produced in e-CRLab. Performance tests will require the board to be operated at maximum frequency (hundreds of MHz). Thus, the interface boards were redesigned for such frequencies and its production outsourced. The first tests have already started. The assessment of the trigger performance passed through end-to-end simulations for the study of the trigger efficiency and rejection parameters.

A detailed performance study of the fluorescence telescopes of the Pierre Auger Observatory was also one of the main subjects addressed in this thesis.

The complete geometry of the telescope was implemented in the Auger $\overline{\text{Off}}$ $\underline{\text{line}}$ simulation framework, using the Geant4 toolkit. The comparison with the existing simulation code showed an overall agreement. However the new code can produce more detailed simulations including some specific features of the telescope optics. Differences on the optical efficiency of the telescope at the level of 1 to 2% were found. The simulation developed constitutes now a tool for detailed simulations of the detector available to the Collaboration. This tool is already being used by the Genoa group to simulate the expected signals induced by muons crossing the detector. The Geant4 simulation is a very versatile tool and allows easy implementation of different geometries of the detector which may be quite important for the design and optimisation of the fluorescence telescopes for the northern site of the Pierre Auger Observatory.

In this thesis detailed performance studies on the light collection efficiency of the FD camera were performed. The light collection efficiency and uniformity are crucial properties of the FD camera. The light collection efficiency of the FD camera

pixels has been studied and mapped using simulated data and laser events. For each case, pixel maps of relative efficiency as a function of the position within the pixel have been produced. Using laser events, the sensitivity of the efficiency modulation within a pixel to the physical spot size was exploited.

In recent years cosmic ray experiments have increased their sensitivity and exposure dramatically. Furthermore these new-generation experiments are taking extreme care with the systematic uncertainties and have gone to a higher level of detail in the comprehension of both the detector itself and of the physics processes involved. This path will be followed by forthcoming experiments that will pose stringent requirements in the design of new detectors and will incorporate new technologies. The improvement in the detectors performance will for sure allow to further enhance knowledge in cosmic ray physics

Bibliography

[1] A. M. Hillas, *Cosmic Rays: Recent Progress and some Current Questions*, *ArXiv Astrophysics e-prints*, July 2006, `astro-ph/0607109`

[2] K. Greisen, *End to the Cosmic-Ray Spectrum?*, *Phys. Rev. Lett.*, **16(17)**:pp. 748–750, Apr 1966, doi:10.1103/PhysRevLett.16.748

[3] G. T. Zatsepin and V. A. Kuz'min, *Upper Limit of the Spectrum of Cosmic Rays*, *Soviet Journal of Experimental and Theoretical Physics Letters*, **4**:p. 78, Aug. 1966

[4] P. Coppi and F. A. Aharonian, *Constraints on the Very High Energy Emissivity of the Universe from the Diffuse GeV Gamma-Ray Background*, *Astrophys. J. L.*, **487**:pp. L9–L12, 1997, doi:10.1086/310883

[5] M. T. Ressell and M. S. Turner, *The Grand Unified Photon Spectrum: A Coherent View of the Diffuse Extragalactic Background Radiation*, *Comm. on Astrophys.*, **14**:p. 323, 1990

[6] J. Albert et al., *VHE γ-Ray Observation of the Crab Nebula and its Pulsar with the MAGIC Telescope*, *Astrophysical Journal*, **674(2)**:pp. 1037–1055, 2008, doi:10.1086/525270

[7] B. Rossi, *Cosmic Rays*, McGraw-Hill, 1964

[8] M. V. S. Rao and B. V. Sreekantan, *Extensive Air Showers*, World Scientific, 1999

[9] T. Bergmann et al., *One-dimensional hybrid approach to extensive air shower simulation*, *Astroparticle Physics*, **26(6)**:pp. 420–432, 2007

[10] H.-J. Drescher and G. R. Farrar, *Air shower simulations in a hybrid approach using cascade equations*, *Phys. Rev. D*, **67(11)**:p. 116001, Jun 2003, doi:10.1103/PhysRevD.67.116001

[11] K. Greisen, *The Extensive Air Showers, Progress in Cosmic Ray Physics*, **3**:p. 1, 1952

[12] T. K. Gaisser and A. M. Hillas, *Reliability of the method of constant intensity cuts for reconstruction of the average development of vertical showers*, in *Proceedings of the 15th Int. Cosmic Ray Conf.*, vol. 8, p. 353, Plovdiv, 1977

[13] K. Greisen, *Cosmic Ray Showers, Annual Review of Nuclear Science*, **10**:pp. 63–108, 1960, doi:doi:10.1146/annurev.ns.10.120160.000431

[14] K. Kamata and J. Nishimura, *The Lateral and the Angular Structure Functions of Electron Showers, Progress of Theoretical Physics Supplement*, **6**:pp. 93–155, 1958

[15] D. Heck, J. Knapp, J. Capdevielle, G. Schatz and T. Thouw, *CORSIKA: A Monte Carlo Code to Simulate Extensive Air Showers*, Tech. Rep. FZKA 6019, Forschungszentrum Karlsruhe, 1998

[16] D. Góra et al., *Universality of the lateral distribution of energy deposit in extensive air showers*, in *Proceedings of the 29th Int. Cosmic Ray Conf.*, vol. 7, pp. 191–194, 2005

[17] *Official NASA GLAST website at http://glast.gsfc.nasa.gov/*

[18] J. Abraham et al. (Pierre Auger collaboration), *Observation of the suppression of the flux of cosmic rays above $4 \times 10^{19} eV$, Physical Review Letters*, **101(6)**:061101, 2008, doi:10.1103/PhysRevLett.101.061101

[19] J. Abraham et al. (Pierre Auger collaboration), *Correlation of the Highest-Energy Cosmic Rays with Nearby Extragalactic Objects, Science*, **318(5852)**:pp. 938–943, November 2007, doi:10.1126/science.1151124

[20] M.-P. Véron-Cetty and P. Véron, *A catalogue of quasars and active nuclei: 12th edition, Astronomy and Astrophysics*, **455**:pp. 773–777, Aug. 2006, doi: 10.1051/0004-6361:20065177

[21] M. Unger (Pierre Auger collaboration), *Study of the Cosmic Ray Composition above 0.4 EeV using the Longitudinal Profiles of Showers observed at the Pierre Auger Observatory*, Jun 2007, `0706.1495`, URL `http://arxiv.org/abs/0706.1495`

[22] J. Abraham et al. (Pierre Auger collaboration), *Upper limit on the cosmic-ray photon flux above* 10^{19} *eV using the surface detector of the Pierre Auger Observatory*, Astroparticle Physics, **29(4)**:pp. 243–256, May 2008, doi:10.1016/j.astropartphys.2008.01.003

[23] A. De Angelis, O. Mansutti and M. Persic, *Very-High Energy Gamma Astrophysics*, Jul 2008, 0712.0315, URL `http://arxiv.org/abs/0712.0315`

[24] http://www.mppmu.mpg.de/~rwagner/sources/, 2008

[25] S. Hoppe et al. (H.E.S.S. collaboration), *The H.E.S.S. survey of the inner Galactic plane*, Oct 2007, 0710.3528, URL `http://arxiv.org/abs/0710.3528`

[26] L. Scarsi, *The extreme universe of cosmic rays : Observations from space*, Nuovo Cim., **24C**:pp. 471–482, 2001

[27] G. Agnetta et al. (ULTRA collaboration), *Extensive air showers and diffused Cherenkov light detection: The ULTRA experiment*, Nucl. Instrum. Meth., **A570**:pp. 22–35, 2007

[28] M. C. Maccarone (The Ultra Collaboration), *Detection of the Cherenkov light diffused by Sea Water with the ULTRA experiment.*, in *Proceedings of the 30th International Cosmic Ray Conference*, 2007

[29] P. Assis, *The Setup and Engineering Run of the ULTRA Experiment*, Master's thesis, Instituto Superior Técnico, 2003

[30] J. Allison et al., *Geant4 developments and applications*, IEEE Transactions on Nuclear Science, **53(1)**:pp. 270–278, 2006

[31] S. Agostinelli et al., *GEANT4-a simulation toolkit*, Nuclear Instruments & Methods in Physics Research Section A-Accelerators Spectrometers Detectors and Associated Equipment, **506(3)**:pp. 250–303, 2003

[32] M. C. Maccarone et al. (GAW collaboration), *Expected Performance of the GAW Cherenkov Telescopes Array - Simulation and Analysis*, in *Proceedings of the 30th International Cosmic Ray Conference*, Jul. 2007

[33] G. Cusumano et al. (GAW collaboration), *GAW - An Imaging Atmospheric Cherenkov Telescope with Large Field of View*, in *Proceedings of the 30th International Cosmic Ray Conference*, Jul. 2007

[34] O. Catalano, M. C. Maccarone and B. Sacco, *Single photon counting approach for imaging atmospheric Cherenkov telescopes*, Astroparticle Physics, **29(2)**:pp. 104–116, 2008, doi:10.1016/j.astropartphys.2007.11.011

[35] E. Cano, *PCI probe: simple labview VIs for PCI debugging*, 2002, URL `http://cano.web.cern.ch/cano/pciprobe/`

[36] O. Catalano and M. C. Maccarone, *ULTRA Experiment - Report on the "Capo Granitola" Campaign 2005*, Tech. Rep. 002/2005, IASF-PA / INAF, 2005

[37] L. Moniz, *Search for extended air showers with TRC*, in *Proceedings of the Sixth International Workshop on New Worlds in Astroparticle Physics*, 2007

[38] Altera Corporation, *Stratix II Device Handbook*, 2007, URL `http://www.altera.com/literature/hb/stx2/stratix2_handbook.pdf`

[39] G. F. Knoll, *Radiation Detection and Measurement*, John Wiley and Sons, Inc., 2000

[40] *Photon Counting using Photomultilier Tubes*, Tech. rep., Hamamatsu, 2005

[41] O. Catalano, *EUSO Trigger - Method and Operational Criteria*, Tech. Rep. EUSO-TEO-REP-002, EUSO, 2003

[42] M. Pallavicini and A. Thea, *ESAF user guide*, Tech. Rep. EUSO-SDA-REP-014-1, EUSO, 2004

[43] A. Thea et al., *The EUSO Simulation and Analysis Framework*, in *Proceedings of the 29th International Cosmic Ray Conference Pune*, vol. 8, pp. 133–136, 2005

[44] P. Assis, *How to select UHECR in EUSO: The trigger system*, in *New worlds in astroparticle physics - Proceedings of the fifth international workshop*, pp. 120–123, World Scientific, 2005

[45] A. Thea, *Osservazione di radiazione cosmica di altissima energia dallo spazio*, Ph.D. thesis, Università degli studi di Genova, 2006, (in English)

[46] GAW collaboration, *Gamma Air Watch (GAW) - Concept Design and Science Case*, December 2005

[47] M. C. Maccarone, *Study of the GAW Expected Performance. Part 1: Analysis at Trigger Level.*, Tech. Rep. GAW_EVE_0004_061127, IASF-Pa/INAF, 2006

[48] M. Pimenta, A. Pina and B. Tomé, *GAW Simulation Framework*, Tech. Rep. GAW_SIM_0008, GAW, 2007

[49] T. Ullrich and Z. Xu, *Treatment of Errors in Efficiency Calculations*, *arXiv:physics/0701199v1*, 2007

[50] M. Born and E. Wolf, *Principles of Optics*, Cambridge Univ. Press, 1999

[51] *Special Filter Glasses for sun beds, Advanced Materials, SCHOTT*, March 2006, URL `http://www.us.schott.com/special_applications/english/download/solarien_march_06us.pdf`

[52] M. de Oliveira, V. de Souza, H. Reis and R. Sato, *Manufacturing the Schmidt corrector lens for the Pierre Auger Observatory, Nuclear Instruments & Methods in Physics Research Section A-Accelerators Spectrometers Detectors and Associated Equipment*, **522**:pp. 360–370, 2004, doi:doi:10.1016/j.nima.2003.11.409

[53] R. Sato, *Desenvolvimento e produção das lentes dos telescópios do Observatorio Auger*, Ph.D. thesis, Universidade Estadual de Campinas. Instituto de Física 'Gleg Wataghin', 2005

[54] C. Aramo et al., *The Camera of the AUGER Fluorescence Detector*, Tech. Rep. GAP-99-027, Pierre Auger Observatory, 1999

[55] S. Argirò et al., *The offline software framework of the Pierre Auger Observatory*, *Nucl. Instrum. Meth. A*, **580**:pp. 1485–1496, 2007, doi:http://dx.doi.org/10.1016/j.nima.2007.07.010

[56] P. Facal San-Luis and P. Privitera, *Measurement of the FD camera light collection effciency and uniformity*, Tech. Rep. GAP-2000-010, Pierre Auger Observatory, 2000

[57] B. Fick et al., *The First Central Laser Facility*, Tech. Rep. GAP-2004-003, Pierre Auger Observatory, 2003

Abbreviations

AAS Analog Acquisition Sub-system

ADC Analog to Digital Converter

Belenos a detector of ULTRA

CAD Computer Aided Design

CAMAC Computer Automated Measurement And Control

CLF Central Laser Facility

CNR Consiglio Nazionale delle Ricerche, Italy

CORSIKA COsmic Ray SImulations for KAscade

CTRIG Control and TRIGger; an interface board for GAW

DAC Digital to Analog Converter

DAQ Data Acquisition

DE2 Development and Education Board

DSP Digital Signal Processor

e.g. exempli gratia (for example)

EAS Extensive Air Shower

e-CRLab Electronics for Cosmic Rays Laboratory

ESAF EUSO Simulation and Analysis Framework

ETScope Electromagnetic Telescope - a detector of ULTRA

EUSO Extreme Universe Space Observatory

FCT Fundação para a Ciência e Tecnologia (Foundation for Science and Technology)

FD Fluorescence Detector

FEBrick Front End Brick

Fermi Fermi Gamma-ray Space Telescope, formerly GLAST

FET Field Effect Transistor

FIFO First-In First-Out

FOV Field Of View

FPGA Field Programmable Gate Array

FTE Full Time Equivalent

GAW Gamma Air Watch

Geant4 GEometry ANd Tracking version 4

GLAST Gamma-Ray Large-Area Space Telescope - NASA announced on 26/08/08 that GLAST has been renamed the Fermi Gamma-ray Space Telescope.

GPS Global Positioning System

GS/s Giga Sample per second

GTU Gate Time Unit

GUI Graphical User Interface

HDL Hardware Description Language

HV High Voltage

I2C Inter-Integrated Circuit (Serial communications protocol)

IASF Istituto di Astrofisica Spaziale e Fisica Cosmica CNR, Italy

IASF-Palermo IASF-CNR at Palermo, Italy (formerly IFCAI)

IDL Interactive Data Language

IP Intellectual Property

IST Instituto Superior Técnico

LIP Laboratório de Instrumentação e Física Experimental de Partículas, Portugal

LIP-PAD LIP - Placa de Aquisição de Dados (LIP - data acquisition board)

LPV3 LIP-PAD Version 3

LV Low Voltage

MAPMT Multi Anode Photo Multiplier Tube

MEFT Mestrado em Engenharia Física Tecnológica (Master in Physics Engineering)

m.i.p. minimum ionizing particle

NIM Nuclear Instrumentation Module

NSB Night Sky Background

PAO Pierre Auger Observatory (as ACRO)

PC Personal Computer

PCB Printed Circuit Board

PCI Peripheral Component Interconnect

PMT Photo Multiplier Tube

ProDAcq Programmable Data Acquisition

PROM Programmable Read-Only Memory

ROI Region Of Interest

ROOT An Object-Oriented Data Analysis Framework developed at CERN

RS232 Recommended Standard RS-232; A standard for serial binary data signals

SD Surface Detector

SPC Single Photon Counting

TDC Time to Digital Converter

TMS Time Measuring Sub-system

TRC Telescópio de Raios Cósmicos (Lisbon Cosmic Ray Telescope)

ULTRA UV Light Transmission and Reflection in Atmosphere

UTC Universal Time Coordinated

UV Ultra Violet

UVIScope UV Imaging Telescope

UVScope UV Telescope

VHDL VHSIC Hardware Description Language